

A new type of one-dimensional discrete map

A. A. Koronovskii

Government Academic and Science Center "Kолledzh," Saratov State University, Saratov

(Submitted August 13, 1997; resubmitted March 18, 1998)

Pis'ma Zh. Tekh. Fiz. **24**, 1–8 (September 17, 1998)

A one-dimensional two-parameter map whose behavior on the plane of control parameters qualitatively reproduces the dynamics of a flow system — an rf oscillator describable by a system of three ordinary differential equations. It is shown that the behavior of the map largely coincides with that of the flow system and is also similar to the results of a previous experiment on the rf oscillator. © 1998 American Institute of Physics.
[S1063-7850(98)00109-8]

A tunnel-diode oscillator has been constructed, investigated, and described by Kiashko, Pikovskii, and Rabinovich.^{1–3} Physical experiments and numerical simulations by those authors showed that this oscillator exhibits chaotic oscillations. The experiments of Ref. 4 produced the first detailed map of the dynamical regimes on the plane of the control parameters — the damping rate and nonlinearity parameter — which showed the route to chaos and the pattern of the transitions between the different types of complex-periodic oscillations as the control parameters are varied. The same system, but with the real tunnel diode replaced by a piecewise-linear analog implemented by means of an operational amplifier, was studied in Ref. 5. It was shown in the course of numerical simulations and physical experiments that replacing the nonlinear element by its piecewise-linear analog did not qualitatively alter the dynamics of this system.

It should be noted that the description of this system was based on a flow model, i.e., the base model chosen for this description is a system of ordinary differential equations. On the other hand, in Refs. 6 and 7 a map was proposed, based on the initial differential equations (the tunnel diode characteristic was approximated by a piecewise-linear function, which, however, was much more idealized and less like the real characteristic than that described in Ref. 5), which in spite of the fact that it was of an implicit form, permitted a clear explanation of the essence of the processes occurring in the system. However, the question of the degree to which the behavior of this map repeats the behavior of the flow system on the plane of control parameters was not considered in detail.

In the present paper we propose a one-dimensional two-parameter map which is a discrete analog of the above-described oscillator with a piecewise-linear analog of the tunnel diode. It should be noted straightaway that this map is not derived from a system of differential equations describing the dynamics of the oscillator⁵ but rather is devised. It should be stressed that such an approach (one of devising discrete maps that are analogs of real physical systems with continuous time) has become more and more widely used in recent years.^{8,9} The map proposed in Ref. 7 was chosen as the base, which was then approximated by an explicitly

specified continuous function depending on two parameters in such a way that, as the values of these parameters were varied, the map constructed would exhibit dynamics analogous to the dynamics of an oscillator with a piecewise-linear analog of a tunnel diode.

The map described above belongs to a fundamentally new class of maps:

$$x_{n+1} = f_{\varphi}(\varepsilon, x_n). \quad (1)$$

The essence of this type of map is that one of the parameters on which it depends is the angle of rotation φ of the graph of the map about some reference point (e.g., (0;0), as in the case under discussion). At a zero angle of rotation the map described has the form

$$f_0(\varepsilon, x) = y_1(x)\sigma(y_2(\varepsilon, x) - y_1(x)) + y_2(\varepsilon, x)\sigma(y_1(x) - y_2(\varepsilon, x)), \quad (2)$$

where the functions $y_1(x)$, $y_2(\varepsilon, x)$ are defined as

$$y_1(x) = 125x, \quad (3)$$

$$y_2(\varepsilon, x) = 2.85\sqrt{(0.45 + \varepsilon)^2 + (x - 0.85)^2} - 0.3, \quad (4)$$

and $\sigma(x)$ is the Heaviside step function. Despite the superficial awkwardness of the form of map (2), the principle by which this map was constructed is quite transparent: Eq. (3) describes the linear part of the map, which corresponds to finding the flow system on the α branch of the characteristic of the piecewise-linear analog of the tunnel diode (see Ref. 5); Eq. (4) is a branch of a hyperbola and corresponds to finding the oscillator on the β branch of the characteristic, and the step function $\sigma(x)$ matches them at the crossing point and ensures the continuity of the function (2). The numerical values in relations (3) and (4) have been chosen so as to make the dynamics of the map similar to the dynamics of the initial flow system.

Now, to obtain a one-dimensional map for another value of the parameter φ , one must rotate the graph of the map about the origin by this angle φ . It is clear that for any rotation angle $\varphi \neq 0$ the map $f_{\varphi}(\varepsilon, x)$ cannot be written in explicit form (in the general case). Moreover, it is not hard to see that when the map is rotated, it is entirely possible that the function $f_{\varphi}(\varepsilon, x)$ will become multivalued. In that case:

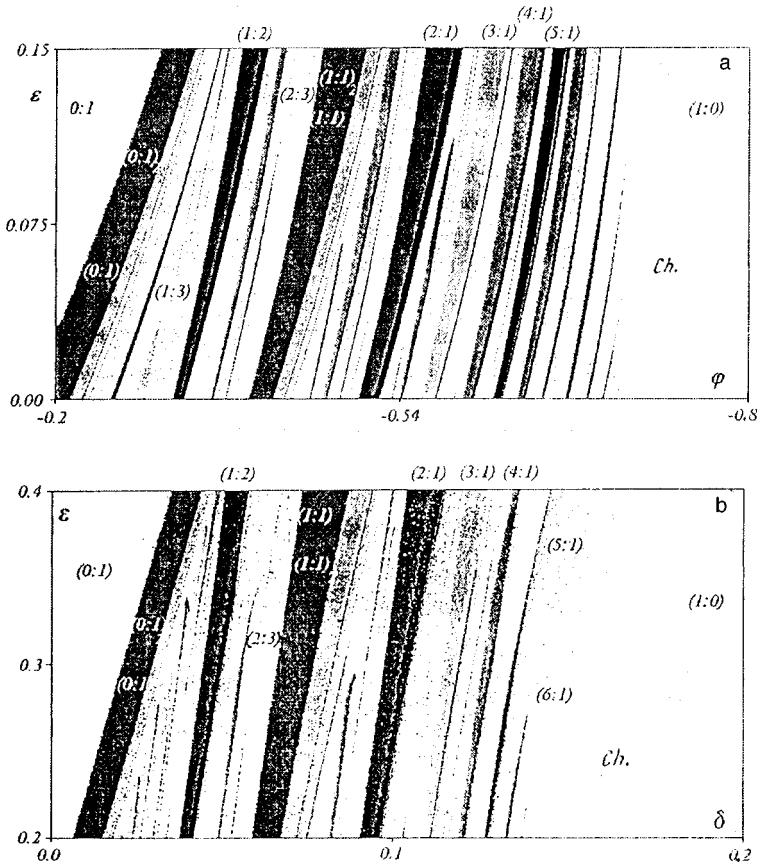


FIG. 1. a: Chart of the regimes on the plane of the control parameters φ and ε for map (1); Ch. denotes chaos. Since a change in the resistance r in an oscillator with a piecewise-linear analog of a tunnel diode corresponds to a nonlinear change of the rotation angle φ , the regimes of the parameter φ on the chart are plotted on a nonlinear scale; b: chart of the regimes of oscillation of an oscillator with a piecewise-linear analog of a tunnel diode on the plane of the control parameters δ and ε , obtained in a numerical simulation (Ch. denotes chaos). The parameter δ is actually the dimensionless resistance r , and the meaning and numerical values of all the other parameters for which this chart was plotted are given in Ref. 5.

1. One can investigate the behavior of $f_\varphi(\varepsilon, x)$ as the behavior of a hysteretic map. Maps of this kind, whose graphs possess multivaluedness, have a real “physical” basis.

2. One can consider the behavior of $f_\varphi(\varepsilon, x)$ as that of a single-valued map by choosing some one branch of the function, as was done in the present case: if at some value x the map $f_\varphi(\varepsilon, x)$ can have two values, corresponding to branches $y_1(x)$ and $y_2(\varepsilon, x)$, then one chooses as the value of $f_\varphi(\varepsilon, x)$ the minimum value, corresponding to branch $y_2(\varepsilon, x)$.

What is the physical essence of a rotation of the graph of a map, and which parameter of the flow system changes in correspondence with the change in the rotation angle φ ? Of course, since the tunnel diode (or its piecewise-linear analog) is the only nonlinear element in the oscillator, all the behavioral features of the flow system will be largely determined by the properties of this nonlinear element. It is clear that the discrete map should convey an impression of the nonlinear element of the system. In essence, as it happens, one need only glance at the graph of the map proposed in Ref. 7 to see the similarity between this map and the current–voltage characteristic of the tunnel diode (or, again, of its piecewise-linear analog). If as the variable whose observed values will be used to construct the one-dimensional map one chooses the current flowing through the diode (it doesn’t matter whether this is the tunnel diode or its analog), then the one-dimensional map illustrating the dependence of, say, the local maximum of the current at the n th step on the maximum value in the previous, $(n-1)$ th, step, the current–voltage characteristic of the diode will be qualitatively reproduced.

One of the main control parameters in the oscillator with the piecewise-linear analog of the tunnel diode is the value of the resistance r that is essentially connected in series with the diode.⁵ Then the diode and the linear resistance r can be regarded as a single nonlinear element whose current–voltage characteristic for $r=0$ is the same as that of the diode (which, however, has its own internal resistance). In turn, the form of the map (1) will be determined by the characteristic of just this “virtual” nonlinear element. It is easy to see that as the resistance r increases, the current–voltage characteristic will be rotated clockwise (consequently, the rotation angle φ will be negative) and distorted. Since we are talking about only a qualitative correspondence between the behavior of the map and the dynamics of the system, we can to a first approximation neglect the distortion of the current–voltage characteristic of the nonlinear element (consisting of the diode and resistor) and, hence, the distortion of the map (1) and assume that the rotation is the main dominant factor determining the properties of the system. Of course, this is only an assumption, but, as we shall see from the discussion below, this assumption is justified to good accuracy.

By analogy with the classification of the regimes of an oscillator containing a piecewise-linear analog of a tunnel diode (see Ref. 5), the oscillatory regimes of are identified by two integers $(m:n)$. The first integer m denotes the number of points of the sequence $\{x_k\}_{k=1}^{n+m}$ (this sequence is actually the period of the oscillations of the discrete map) that lie on the linear part of the map (1); this number corresponds to the

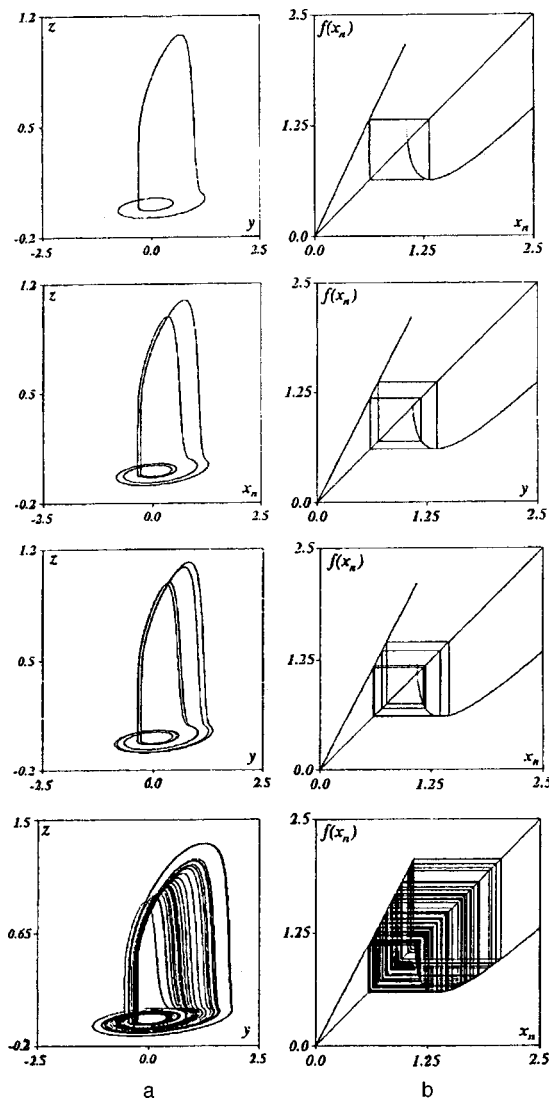


FIG. 2. Transition to chaos based on the (1:1) regime. a: Phase portraits of the behavior of an oscillator with a piecewise-linear analog of a tunnel diode; numerical simulation ($\varepsilon=0.2$): $(1:1)_1 \delta=0.06$, $(1:1)_2 \delta=0.069$, $(1:1)_4 \delta=0.0705$, $(1:1)_{\text{chaos}} \delta=0.078$; b: one-dimensional map $f_\varphi(\varepsilon, x)$ ($\varepsilon=0.05$): $(1:1)_1 \varphi=-0.442$, $(1:1)_2 \varphi=-0.464$, $(1:1)_4 \varphi=-0.469$, $(1:1)_{\text{chaos}} \varphi=-0.479$.

total number of turns of the phase trajectory that lie in the parameter plane of the voltage across the capacitor and the current through the diode for an oscillator with a piecewise-

linear analog of a tunnel diode. The number n in turn is defined as the number of points of the same sequence which lie on the second segment of the map (1); it corresponds to the total number of turns of the phase trajectory of the attractor that protrude into space, for an oscillator containing a piecewise-linear analog of a tunnel diode.^{4,5}

As we see from Fig. 1, the similarity of the dynamics of the flow system and discrete map turns out to be extremely good. The chart of the regimes of the map reproduces not only the base cycles ($m:1$), $m=0,1,2, \dots$ but also the windows of periodicity in the regions corresponding to chaotic oscillations. One can also clearly discern for the discrete map the scenario of the transition from periodic to chaotic oscillations. An example of this scenario based on the (1:1) regime is illustrated in Fig. 2.

Thus the proposed map (1) gives good qualitative agreement between the behavior of an oscillator with a piecewise-linear analog of a tunnel diode (flow system) and the dynamics of this map. It seems extremely promising to employ discrete-map analogs of the map (1) described above in the qualitative study of flow systems (in which one of the control parameters is the dissipation parameter) and, in particular, for constructing a chart of the regimes on the plane of the control parameters.

In closing, the author expresses his deep gratitude to A. A. Kipchatov for interest in this study, for much valuable advice, and for fruitful discussions.

This study was supported by the Russian Fund for Fundamental Research, Grant No. 96-02-16753.

¹A. S. Pikovsky and M. I. Rabinovich, *Physica D* **2**, 8 (1981).
²M. I. Rabinovich, *Usp. Fiz. Nauk* **125**, 123 (1978) [*Sov. Phys. Usp.* **21**, 443 (1978)].
³A. S. Pikovskii, *Izv. Vyssh. Uchebn. Zaved. Radiofiz.* **23**, 883 (1980).
⁴A. V. Andrushkevich and A. A. Kipchatov, *Izv. Vyssh. Uchebn. Zaved. Radiofiz.* **33**, 431 (1990).
⁵A. V. Andrushkevich *et al.*, *Izv. Vyssh. Uchebn. Zaved. PND* **1**, 93 (1993).
⁶A. S. Pikovskii and M. I. Rabinovich, *Dokl. Acad. Nauk SSSR* **239**, 301 (1978) [*Sov. Phys. Dokl.* **23**, 183 (1978)].
⁷S. V. Kiyashko, A. S. Pikovskii, and M. I. Rabinovich, *Radiotekh. Elektron.* **25**, 336 (1980).
⁸B. P. Bezruchko, M. D. Prokhorov, and E. P. Seleznev, *Chaos, Solution and Fractals* **5**, 2095 (1995).
⁹B. P. Bezruchko, M. D. Prokhorov, and A. U. Zhalnin, *Proceedings of the 5th International Specialist Workshop of Nonlinear Dynamics of Electronic Systems. NDES'97, Moscow, Russia, June 26-27, 1998*, pp. 431-436.

Translated by Steve Torstveit

On the degree to which the wide-gap part of a $p-n$ heterojunction influences the breakdown field and the carrier multiplication coefficients

V. A. Kholodnov and N. E. Kurochkin

State Science Center of the Russian Federation, State Enterprise NPO Orion, Moscow
(Submitted December 26, 1997)

Pis'ma Zh. Tekh. Fiz. **24**, 9–15 (September 12, 1998)

It is shown that in the analysis of an avalanche process in a $p-n$ heterojunction it is necessary, as a rule, to take into account the multiplication of carriers in the wide-gap part of the space-charge region of the $p-n$ heterojunction even when the difference between the band gaps \mathcal{E}_g in the narrow-gap and wide-gap layers is large, in spite of the fact that the impact ionization coefficients for electrons (α) and holes ($\beta = K\alpha$) in a semiconductor decreases sharply with increasing \mathcal{E}_g . © 1998 American Institute of Physics. [S1063-7850(98)00209-2]

According to the well-known Sze–Gibbons expression^{1,2} for an avalanche breakdown voltage $V = V_B$ of an asymmetric (say $p-n^+$) junction, the breakdown field E_B of the junction, i.e., the corresponding value of the electric field $E(x)$ at the metallurgical interface ($x=0$) of the $p-n^+$ junction can be determined, for a specified dopant concentration N in the p layer, from the condition

$$\Phi(\varepsilon, \mathcal{E}_g, N, E_B) \equiv \left(\frac{5\varepsilon_0\varepsilon}{6q10^6} \right)^4 \left(\frac{1.1}{\mathcal{E}_g} \right)^6 \left(\frac{E_B}{10^5} \right)^8 \frac{1}{N} = 1, \quad (1)$$

where ε is the dielectric constant. Here and below we adopt the following units of measurement, which are convenient for this topic:² energy (eV), electric field E (V/cm), electron charge q (C), permittivity of free space ε_0 (F/m), α and β (1/cm), mean free paths λ_e and λ_h of electrons and holes between scattering events on phonons (cm), and concentration (cm^{-3}). Relation (1) does not take into account the multiplication of carriers in the n^+ layer; this simplification is justified by the fact that $E(x)$ falls off more rapidly with depth in the n^+ layer than in the p layer and by the sharp field dependence of $\alpha(E)$ and $\beta(E)$.^{1–6} in Refs. 7 and 8 the multiplication was taken into account in both parts of the $p-n$ junction. The electron and hole multiplication coefficients M_e and M_h depend sharply on E_B (Ref. 9), as does (for $V \cong V_B$) the interband tunneling current, which is substantial even in structures with values of \mathcal{E}_g that are not small.^{6,10,11} This is the case, for example, in the InP/In_{0.43}Ga_{0.47}As heterostructures that are widely used in optical communications.⁶

Since α and β also depend sharply on \mathcal{E}_g (Ref. 1–6), the breakdown field $E_B^{(N)}$ of a $p-n$ heterojunction can be determined to a certain approximation by substituting the parameters of the narrow-gap layer into Eq. (1) (the parameters of the narrow-gap (N) and wide-gap (W) layers are denoted by indices N and W). However, the degree to which the W layer influences the value of $E_B^{(N)}$ and hence the carrier multiplication coefficients has not been analyzed before. In the present paper we give the results of such an analysis.

The problem is of interest physically for the following reasons:

1. in passing through the heterointerface ($x=0$) the carriers can acquire energy on account of the jump in the energy of the bottom of the conduction band, $\Delta\mathcal{E}_c$, or of the top of the valence band, $\Delta\mathcal{E}_v$ (Fig. 1).
2. As a rule, $\varepsilon_N > \varepsilon_W$ (Refs. 12–16), and therefore $E_W/E_N = \varepsilon_N/\varepsilon_W > 1$, where E_N and E_W are the fields at the heterointerface in the N and W layers (Fig. 2).
3. The breakdown field of the $p-n$ heterojunction should also be affected by the difference in the concentrations of dopants N_N and N_W in the narrow-gap and wide-gap layers, respectively.

Suppose that the current J through the heterojunction is initiated by the current J_{ini} of minority carriers (electrons) leaking into the space-charge region of the n layer (Fig. 1). This assumption, as analysis shows and as one would expect, does not affect the breakdown field (as is also the case for homojunctions; see Refs. 2–8 and 17. Most likely it is either the case that only carriers of one type acquire an energy increment $\Delta\mathcal{E}$ upon passage through the heterointerface or else the increment $\Delta\mathcal{E}$ for the carriers of the other type is much less than the ionization threshold energy \mathcal{E}_i (Refs. 14–16). Therefore, let us assume for the sake of definiteness that it is only the holes that undergo this additional (non-field-related) jumplike heating (Fig. 1). We write

$$J_e^{(N,W)}(x) = J - J_h^{(N,W)}(x), \quad J_h^{(N)}(0) = J_{\text{ion}} + J_{\text{bal}}(0), \quad (2)$$

where $J_e^{(N,W)}$ and $J_h^{(N,W)}$ are the electron and hole currents in the N and W layers, J_{ion} is the total (net) current of holes that cause impact ionization immediately after crossing the heterointerface and of holes that have arisen as a result of impact ionization; in this case their energy \mathcal{E} is close to $\mathcal{E}_v^{(N)}$; $J_{\text{bal}}(0)$ is the current of holes that enter the N layer ballistically, which either collide with phonons at a distance of the order of $\lambda_h^{(N)}$ or, as they are heated by the field, bring about impact ionization.

Let r be the fraction of the hole current $J_h^{(W)}(0)$ due to holes which, on account of the jump in \mathcal{E}_v , cause impact ionization at the point $x=0$ of the narrow-gap part of the space-charge region. This means that

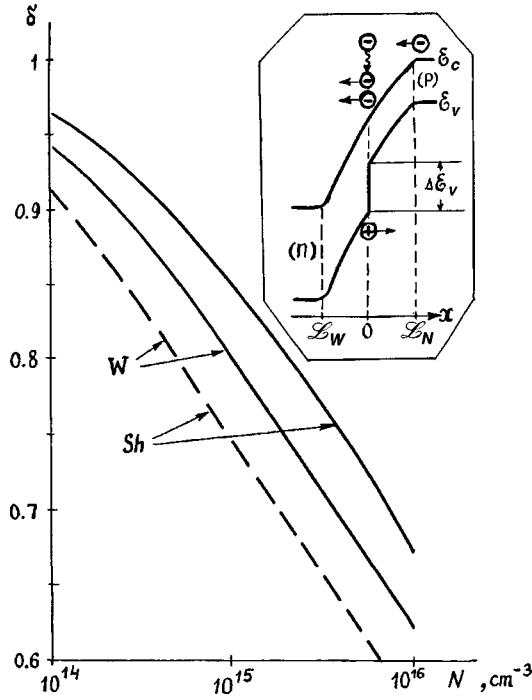


FIG. 1. Ratio $\delta \equiv E_B^{(N)}/E_{B0}^{(N)}$ of the breakdown field $E_B^{(N)}$ in the narrow-gap (N) part (p type) of GaAs/Ge and GaP/Ge p - n heterojunctions to the value $E_{B0}^{(N)}$ of the breakdown field calculated without taking carrier multiplication in the wide-gap (W) part (n type) of the heterojunctions into account, plotted as a function of the dopant concentration N_N in the N layer with the use of the Wolf (W) and Shockley (Sh) approximations of the energy distribution functions of the carriers, respectively. It is assumed that the dopant concentration in the W layer is $N_W = 10^{15} \text{ cm}^{-3}$, that the mean free path λ_h between scatters on phonons is $8 \times 10^{-7} \text{ cm}$ in Ge, $4 \times 10^{-7} \text{ cm}$ in GaAs, and $3.5 \times 10^{-7} \text{ cm}$ in GaP (Ref. 5), that the ionization threshold energy for holes in germanium is $\mathcal{E}_{ih}^{(N,W)} = 1.3 \text{ eV}$ (Ref. 5), that the jump $\Delta \mathcal{E}_v$ of the top of the valence band at the metallurgical boundary ($x=0$) is 0.7 and 1.44 eV for GaAs/Ge and GaP/Ge p - n heterojunctions, respectively,¹⁶ and that the ratio $K = \beta/\alpha$ of the impact ionization coefficients for holes (β) and electrons (α) is equal to 2 in Ge^{6,22} and to 1 in GaAs and GaP.⁶ The inset shows the band diagram of the p - n heterojunction in the working regime, where \mathcal{L}_N and \mathcal{L}_W are the thicknesses of the space-charge regions in the N and W layer of the p - n heterojunction, respectively.

$$J_{\text{ion}} = 2rJ_h^{(W)}(0), \quad J_{\text{bal}}(0) = (1-r)J_h^{(W)}(0),$$

$$J_h^{(N)}(x_1) = \kappa J_h^{(W)}(0), \quad (3)$$

where $\kappa = 1 + r + (1-r)\rho$, $\rho J_{\text{bal}}(0) = J_h^{(N)}(x_1) - J_h^{(N)}(0)$ is the total increment to the current $J_h^{(N)}(x)$, attained at a distance x_1 from the heterointerface much less than the thickness of the N part of the space-charge region, due to ionization by holes of the initial current $J_{\text{bal}}(0)$, conditions being such that the maximum possible energy that can be acquired by the carriers in the electric field over the length x_1 is far from sufficient for impact ionization. Therefore, we can write^{2-8,18} that

$$J = M_h^{(N)}J_h^{(N)}(x_1) + M_e^{(N)}J_{\text{ini}} = M_e^{(W)}J_e^{(W)}(0), \quad (4)$$

where $M_{e,h}^{(N,W)}$ are the electron and hole multiplication coefficients relating to the passage of these particles through the N or the W part of the space-charge layer. It follows from relations (2)–(4) that the breakdown field is determined by the equation

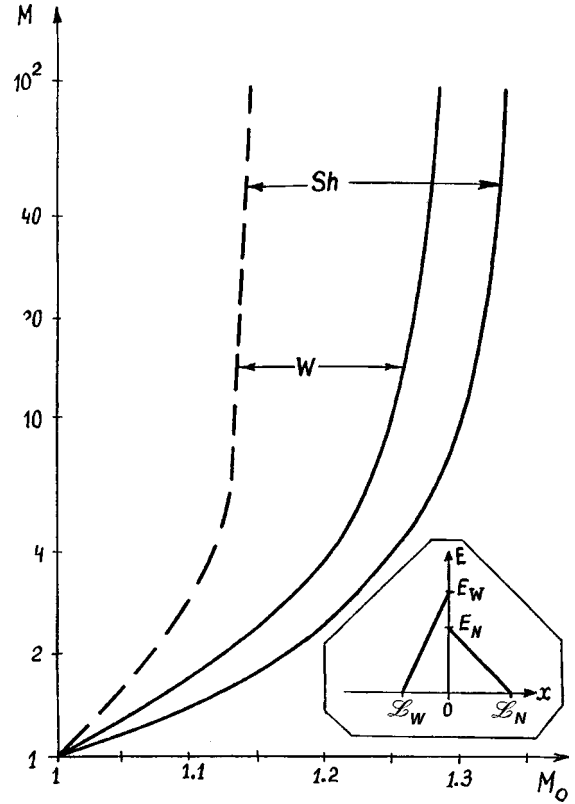


FIG. 2. Carrier multiplication coefficients M in GaAs/Ge and GaP/Ge p - n heterojunctions as functions of the multiplication coefficient M_0 calculated without taking into account the multiplication of carriers in the wide-gap (W) part (n type) of the heterojunctions. W and Sh are the Wolf and Shockley energy distribution functions of the carriers, respectively. It is assumed that the concentration of the dopants in the W and N layers are 10^{15} cm^{-3} , while the remaining parameters have the same values as in Fig. 1. The inset shows an illustration of the electric field $E(x)$ in the space-charge region, where \mathcal{L}_N and \mathcal{L}_W are the thicknesses of the space-charge regions in the N and W layers of the p - n heterojunction, respectively.

$$M_e^{(W)} = (M_e^{(W)} - 1) \kappa M_h^{(N)}. \quad (5)$$

For a number of semiconductors, e.g., for Ge, Si, InP, $\text{In}_{0.53}\text{Ga}_{0.47}\text{As}$, GaAs, and GaP, an approximate relation holds between α and β (Ref. 19). That relation can be used to derive numerical expressions for M_e and M_h in a p - n homojunction⁸ which are in quantitative agreement with the earlier results of numerical calculations²⁰ and experimental data.²¹⁻²⁶ Following Ref. 8, one can use this relation to obtain

$$M_e^{(W)} = \frac{K_W(E_W) - 1}{K_W(E_W) - G_W}, \quad M_h^{(N)} = \frac{K_N(E_N) - 1}{K_N(E_N) - G_N} G_N, \quad (6)$$

where $K_{N,W}(E)$ is the ratio of β to α in the N and W layers, and

$$G_{N,W} = \exp\{\Phi(\varepsilon_{N,W}; \mathcal{E}_g^{(N,W)}; N_{N,W}; E_{N,W}) \ln(K_{N,W}(E_{N,W}))\}. \quad (7)$$

To determine the possible values of κ it is sufficient to consider the Wolf²⁷ (W) and Shockley²⁸ (Sh) approximations for the energy distributions of the carriers (the limiting cases of strong and weak fields^{3-6,29}).

W. The dissipation of the carrier energy on phonons is unimportant,^{3-6,27,29} and so $\rho=1$ and hence $\kappa=2$.

Sh. Since for $\mathcal{E} > \mathcal{E}_i$ the impact ionization cross section is ordinarily a very sharply rising function of \mathcal{E} (Ref. 3-6), the holes will cause ionization almost immediately after attaining the threshold energy. This allows us to write

$$r = \frac{\int_{\mathcal{E}_{ih}^{(N)} - \Delta\mathcal{E}_v}^{\mathcal{E}_{ih}^{(W)}} f(\mathcal{E}) d\mathcal{E}}{\int_0^{\mathcal{E}_{ih}^{(W)}} f(\mathcal{E}) d\mathcal{E}},$$

$$J_{\text{bal}}(x) = J_{\text{bal}}(0) \exp\left(-\frac{x}{\lambda_h^{(N)}}\right) \frac{F(x)}{F(0)}, \quad (8)$$

where

$$f(\mathcal{E}) = \exp\{-\mathcal{E}/\lambda_h^{(W)} E\}, \quad F(x) = \int_0^{\tilde{\mathcal{E}}(x)} f(\mathcal{E}) d\mathcal{E},$$

$$\tilde{\mathcal{E}}(x) = \mathcal{E}_{ih}^{(N)} - \Delta\mathcal{E}_v - E_y x, \quad (9)$$

and $\mathcal{E}_{ih}^{(N,W)}$ are the ionization threshold energies for holes in the N and W materials. In the second of Eqs. (8) the second and third factors characterize the decrease in the ballistic flux of the holes owing to their scattering on phonons and to impact ionization events caused by them, respectively. Using expressions (8) and (9) and the inequality $f(\mathcal{E}_{ih}^{(N)} - \Delta\mathcal{E}_v) \ll f(0)$, we find that

$$r = \exp\left(-\frac{\varepsilon_W \mathcal{E}_{ih}^{(N)} - \Delta\mathcal{E}_v}{\varepsilon_N q \lambda_h^{(W)} E_N}\right), \quad \rho = -\frac{r - r^a}{a - 1}, \quad a = \frac{\varepsilon_N \lambda_h^{(W)}}{\varepsilon_W \lambda_h^{(N)}}. \quad (10)$$

The expressions obtained above can be used to express N_N explicitly in terms of $E_B^{(N)}$ and thereby to determine easily the dependence of $E_B^{(N)}$ on N_N . It is seen from Fig. 1 that the error in the value of $E_B^{(N)}$ due to neglect of carrier multiplication in the W layer increases, naturally, with increasing N_N and already amounts to approximately 20% at $N_N = N_W$. Because of this, condition (1) cannot be used even for an order-of-magnitude estimate of the carrier multiplication coefficients, and the situation becomes worse (even by orders of magnitude) as $\mathcal{E}_g^{(W)}$ increases (Fig. 2). A similar situation exists for the tunnel currents under conditions of avalanche multiplication of carriers.

¹S. M. Sze and G. Gibbons, *Appl. Phys. Lett.* **8**, 111 (1966).

²S. M. Sze, *Physics of Semiconductor Devices*, Wiley, New York (1969) [cited Russian translation, Mir, Moscow (1984), Book 1, 455 pp].

³A. S. Tager and V. M. Val'd-Perlov, *IMPATT Diodes and Their Application in Microwave Technique* [in Russian], Sov. Radio, Moscow (1968), 480 pp.

⁴G. E. Stillman and C. M. Wolf, in *Semiconductors and Semimetals*, Vol. 12, edited by R. K. Willardson and A. C. Beer, Academic Press, New York (1977), pp. 291-393.

⁵I. V. Grekhov and Yu. N. Serezhkin, *Avalanche Breakdown of p-n Junctions in Semiconductors* [in Russian], Énergiya, Leningrad (1980), 152 pp.

⁶W. T. Tsang (Ed.), *Lightwave Communications Technology. Photodetectors* Mir, Moscow (1988), 528 pp.

⁷V. A. Kholodnov, *Pis'ma Zh. Tekh. Fiz.* **14**, 1349 (1988) [*Sov. Tech. Phys. Lett.* **14**, 589 (1988)].

⁸V. A. Kholodnov, *Fiz. Tekh. Poluprovodn.* **30**, 1051 (1996) [*Semiconductors* **30**, 448 (1996)].

⁹V. A. Kholodnov, *Opt. Zh.* **30**, 53 (1996).

¹⁰V. V. Osipov and V. A. Kholodnov, *Zh. Tekh. Fiz.* **59**(1), 80 (1989) [*Sov. Phys. Tech. Phys.* **34**, 46 (1989)].

¹¹V. A. Kholodnov, *Opt. Zh.* **59**, 42 (1996).

¹²M. Rodo, *Semiconductor Materials*, Metallurgiya, Moscow (1971), 232 pp.

¹³R. A. Smith, *Semiconductors*, Cambridge Univ. Press, Cambridge (1959); Mir, Moscow (1982), 600 pp.

¹⁴H. C. Casey Jr. and M. B. Panish, *Heterostructure Lasers*, Part B, Academic Press, New York (1978); Vol. 2, Mir, Moscow (1981), 366 pp.

¹⁵A. G. Milnes and D. Feucht, *Heterojunctions and Metal-Semiconductor Junctions*, Academic Press, New York (1972); Mir, Moscow (1975), 432 pp.

¹⁶B. L. Sharma and R. K. Purokhit, *Semiconductor Heterojunctions* [in Russian], Sov. Radio, Moscow (1979), 232 pp.

¹⁷V. V. Osipov and V. A. Kholodnov, *Fiz. Tekh. Poluprovodn.* **21**, 2078 (1987) [*Sov. Phys. Semicond.* **21**, 1259 (1987)].

¹⁸N. Kh. Artsis and V. A. Kholodnov, *Radiotekh. Elektron.* **29**, 151 (1984).

¹⁹V. A. Kholodnov, *Pis'ma Zh. Tekh. Fiz.* **14**, 551 (1988) [*Sov. Tech. Phys. Lett.* **14**, 246 (1988)].

²⁰R. Leguerre and J. Urgell, *Solid-State Electron.* **19**, 875 (1976).

²¹S. L. Miller, *Phys. Rev.* **99**, 1234 (1955).

²²A. P. Shotov, *Zh. Tekh. Fiz.* **28**, 437 (1958) [*Sov. Phys. Tech. Phys.* **3**, 413 (1958)].

²³S. V. Bogdanov, A. B. Kravchenko, A. F. Plotnicov, and V. E. Shubin, *Phys. Status Solidi A* **93**, 361 (1986).

²⁴G. E. Stillman, L. W. Cook, N. Tabatanaie, G. E. Bulman, and V. M. Robbins, *IEEE Trans. Electron Devices* **ED-30**, 364 (1983).

²⁵R. D. Baertsch, *J. Appl. Phys.* **38**, 4267 (1967).

²⁶V. V. Gavryushko, O. V. Kosogov, and V. D. Lebedeva, *Fiz. Tekh. Poluprovodn.* **12**, 2351 (1978) [*Sov. Phys. Semicond.* **12**, 1398 (1978)].

²⁷P. A. Wolf, *Phys. Rev.* **95**, 1415 (1954).

²⁸W. Shockley, *Solid-State Electron.* **2**, 35 (1961).

²⁹G. A. Baraff, *Phys. Rev.* **128**, 2507 (1962).

Translated by Steve Torstveit

Numerical simulation of the lowering of the drag of a cylinder containing vortex cells with the use of a control system for the turbulent boundary layer

P. A. Baranov, S. A. Isaev, Yu. S. Prigorodov, and A. G. Sudakov

Academy of Civil Aviation, St. Petersburg

(Submitted February 25, 1998)

Pis'ma Zh. Tekh. Fiz. **24**, 16–23 (September 12, 1998)

[S1063-7850(98)00309-7]

Using a factorized finite-volume method of solving the Reynolds equations closed by a two-parameter dissipative model of turbulence, we analyze the lowering of the frontal drag of a cylinder containing vortex cells when the boundary layer is controlled by utilizing provisions for the suction of fluid at the central shaft of the cell.

Methods of decreasing the drag of a profile by controlling the turbulent boundary layer by the blowing and suction of fluid in the wall layers are well known in aerodynamics. For practice purposes, however, these methods have not been developed very far. The growing interest in vortex traps on curvilinear surfaces of objects has stimulated the use of suction of the fluid as an instrument for intensifying the flow in these traps.

In the present study we employ numerical simulation methods to pose and solve the related problem of the influence of large-scale trapped vortex structures on the turbulent flow of an incompressible viscous fluid around an object and on the aerodynamic drag of an object of classic geometry — a circular cylinder — for different positions of a circular cell with respect to the center of the cylinder (Fig. 1a). The vortex cells under discussion have a central shaft of the same geometry, with provisions for suction of the fluid over the entire contour of the shaft (Fig. 1b and 1c).

The algorithm that was devised is based on the finite-volume method of solving the Reynolds-averaged Navier–Stokes equations closed with a high-Reynolds two-parameter dissipative model of turbulence, utilizing the concept of decomposition of the computational region and the generation in substantially different-scale subregions of overlapping multigrid oblique-angle meshes of the same type (viz., of the O type). The system of initial equations is written in divergence form for the increments of the dependent variables: the covariant components of the velocity and pressure. Such an approach is characterized by a more exact representation of the flows through the faces of the computational cells.

In the approximation of a source term, which in the case of the steady-state problem is the right-hand side of the equations for the momentum, convective flows were calculated with a one-dimensional counterflow quadratic interpolation scheme, which was proposed by Leonard.¹ It should be noted that the Leonard scheme should be applied not to the covariant but to the Cartesian components of the velocity, otherwise failure of the “uniform flow” test could occur. For this reason, and for convenience of computer programming, it

was proposed to determine the Cartesian projections of the vector source term and then to project it onto the axes of a curvilinear coordinate system. In the discretization of the convective terms of the transport equations of the turbulence characteristics, we used both the aforementioned Leonard scheme and also the UMIST scheme, which is a modified TVD scheme.²

The proposed computational model is based on the concept of splitting according to physical processes and is implemented in the SIMPLEC pressure-correction procedure. The characteristic features of this iterative algorithm are that the provisional velocity components for the “frozen” pressure and turbulent-viscosity fields are determined at the “predictor” step and the pressure is subsequently corrected on the basis of a solution of the continuity equation with corrections to the velocity field. The computational process is devised so that in one “predictor” step there are several local iteration steps in the pressure-correction routine. Then, in solving the transport equations of the turbulence characteristics the turbulent vortical viscosity is re-determined. The computational procedure utilizes the method of global iterations over subregions with a subsequent interpolation of the dependent variables in the zones where the subregions overlap.

The choice of a centered pattern with the dependent variables referenced to the center of the computational cell is motivated by the fact that it tends to simplify the computational algorithm and reduce the number of computational operations. In this approach the pressure oscillations are eliminated by the Rhee–Chow approach. A high stability of the computational procedure is ensured by the use of single-sided counterflow differences for discretization of the convective terms in the implicit part of the equations for the increments of the unknown variables, by the damping of the nonphysical oscillations through the introduction of artificial diffusion in the implicit part of the equations, and by the use of stabilizing pseudo-time terms. The computational efficiency of the computational algorithm is also enhanced by the method of incomplete matrix factorization in the Stone version (SIP) for solving systems of nonlinear algebraic equations. The standard method of near-wall functions¹ was used in the calculations.

In solving the problem of the turbulent flow around a transversely oriented cylinder, for a more exact resolution of the structural elements of different scales it is helpful to treat

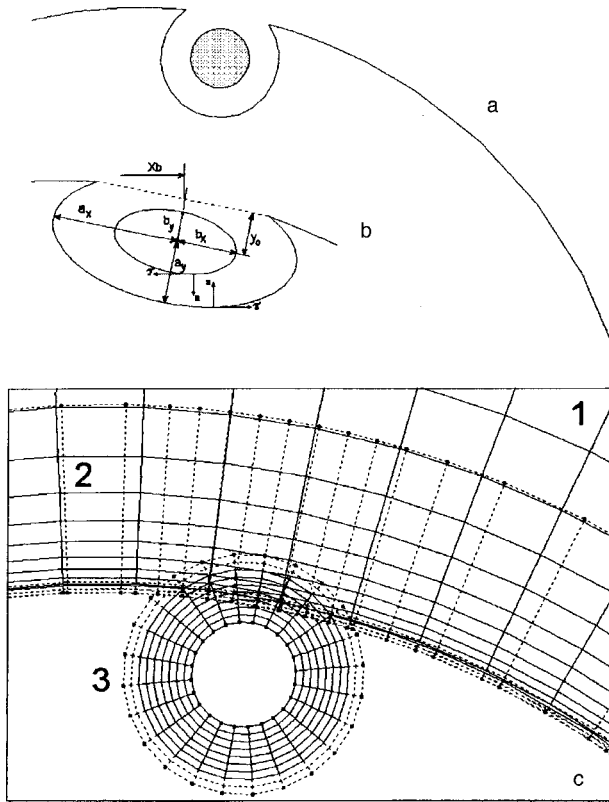


FIG. 1. Fragment of the contour of a cylinder with a vortex cell (a), a sketch of the cell with the notation and a fragment of the composite mesh (b), which consists (c) of two-grid (1,2) mesh around the cylinder and the mesh in the vortex cell (3).

separately a near-wall region with a thickness of approximately 0.1 times the cylinder diameter (which is chosen as the characteristic dimension), an intermediate circular region encompassing the attachment zone in the near wake behind the cylinder, and a peripheral annular zone whose outer boundary lies at a sufficient distance (of the order of 50–100) from the object. The introduction of an annular zone (Fig. 1c) or equivalently the construction of multigrid meshes is motivated not only by the faster convergence of the solution of the problem because of the smaller number of computational cells required but also, and more importantly, by the adaptation of the local mesh to the characteristics of the particular structural element of the flow which is being mapped: the boundary layer on the surface of a cylinder, the return flow in the wake, and the flow around the object at a large distance from it. It should be noted that the results presented in this paper were obtained on the assumption that a symmetric regime of flow around the cylinder is realized. This permits some simplification of the solution of the prob-

TABLE I. Results of numerical and experimental studies of the integral characteristics of turbulent flow around a circular cylinder in a transverse flow.

Re	Mesh	C_x	C_{xf}	X_s	Source
10 000	Multigrid	0.686	0.024	3.96	Present study
10 000	100×62	0.743	0.011	5.00	Ref. 3
14 500	–	0.72	–	–	Ref. 4

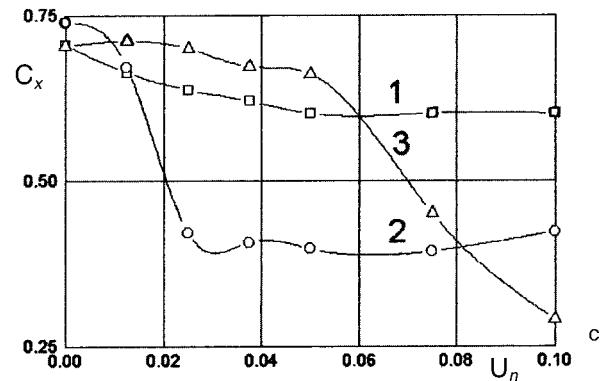
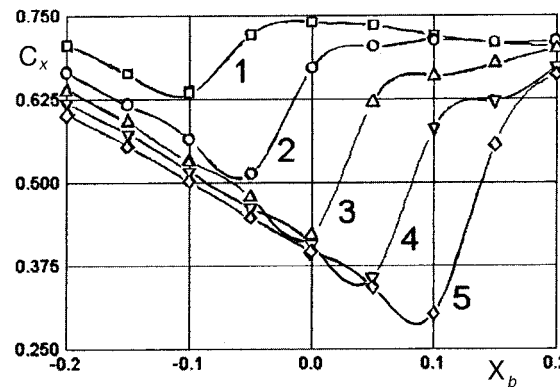
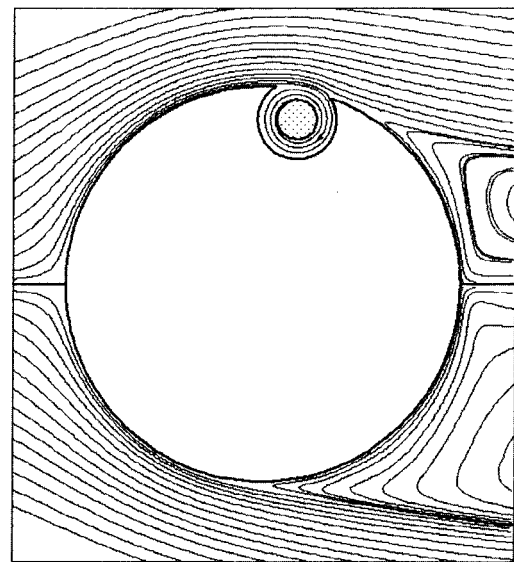


FIG. 2. Comparison of the patterns of turbulent flow around a cylinder with a vortex cell (for $U_n=0.05$ and $X_b=0.1$) and a smooth cylinder (a); the frontal drag coefficient C_x of the cylinder as a function of the position of the vortex cells (b): 1 — $U_n=0$, 2 — 0.0125, 3 — 0.025, 4 — 0.0375, 5 — 0.05; and as a function of the suction velocity (c): 1 — $X_b=-0.2$; 2 — 0; 3 — 0.2.

lem by considering the flow in a single half plane. Numerical simulations carried out without making use of this assumption confirm the validity of this approach.

One can state a requirement on the mutual positioning of the zones: the region in which adjacent zones are superposed should include around 3–4 cells of each zone, so that the total overlap region contains of the order of 6–8 computational cells. If this requirement is not met and the number of

cells is smaller than that indicated, then the process of information transfer between zones breaks down. The opposite case, choosing too large a number of cells in the overlap region, is a waste of computational resources. In the present study the number of mesh points in the outer zone is 15×40 , the number in the intermediate zone is 60×80 , and the number in the near-wall zone is 21×80 . The step near the wall is 0.0005.

Inside the vortex cells the mesh is constructed uniformly in the circumferential direction toward the radius (the chosen number of mesh points is 21). The number of mesh points (15) on the cut through the cavity is specified. The total number of mesh points in the circumferential direction is then calculated from the condition that the angular step be equal. The diameter of the vortex cell is taken equal to 0.2. The diameter of the central shaft is 0.1. In all cases the cells are distributed inside the cylinder at a depth of 15% of the transverse dimension of a cell ($y_0 = 0.7a_x$). Different positions of the cells are considered, characterized by a distance X_b from the forward critical point of the cylinder to the rear edge of the cell (Fig. 1b). Also, the normal component U_n of the suction velocity at the central object of the cell is also varied. The Reynolds number is specified as 10^4 . An analysis (see Table I) of the calculated coefficients of frontal drag C_x , frictional drag C_{xf} , and detachment zone length X_s in the near wake behind the cylinder in comparison with the available computational³ and experimental⁴ data for roughly similar values of Re shows that the computational algorithm devised here is suited to the task.

Placing a vortex cell on the contour of a cylinder in a flow in the absence of suction can reduce the frontal drag by approximately 10% if the cell is in a forward position. Then the observed effect is analogous to the lowering of the drag of an object with a forward separation zone (an object con-

sisting of two disks or a composite of a disk and a cylinder).¹ However, this effect is weakly expressed because the circumferential flow in the cell is not well developed. Suction of fluid at the central shaft of the cell will bring about a growing intensification of the flow in the bucket, and with increasing suction velocity the local minimum of the frontal drag of a cylinder with cells (Fig. 2b) is shifted toward a rearward position of the cell on the contour of the cylinder (at a constant suction velocity). The reason lies not only in the redistribution of the local loads inside the vortex cells but also in a change of the pattern of the flow around the cylinder. It follows from Fig. 2a that enhancing the momentum of the turbulent flow in the near-wall zone of the cylinder due to the intense return flow in the cell substantially deforms the region of detached flow in the near wake behind the cylinder. It should be emphasized that the drag of the cylinder falls off by nearly half, and for a central position of the vortex cell on the contour of the cylinder the drag of the cylinder remains at a nearly constant level over a considerable interval of suction velocities (Fig. 2c).

This study was carried out with the financial support of the Russian Fund for Fundamental Research under Project Nos. 96-01-01290 and 96-01-00298.

¹I. A. Belov, S. A. Isaev, and V. A. Korobkov, *Computational Problems and Methods for Detached Flows of Incompressible Fluids* [in Russian], Sudostroenie, Leningrad (1989), 256 pp.

²F. S. Lien, W. L. Chen, and M. A. Leschziner, *Int. J. Numer. Methods Fluids* **23**, 567 (1996).

³I. A. Belov and N. A. Kudryavtsev, *Heat Transfer and the Drag of Stacks of Tubes* [in Russian], Leningrad (1987), 213 pp.

⁴A. Roshko, "On the drag and shedding frequency of two-dimensional bluff bodies," NASA Tech. Note No. 3169 (1954).

Resonance ring interferometry with incoherent light

M. A. Novikov and V. V. Ivanov

Institute of Physics of Microstructures, Russian Academy of Sciences, Nizhniĭ Novgorod
(Submitted November 19, 1997)

Pis'ma Zh. Tekh. Fiz. **24**, 24–29 (September 12, 1998)

A new method of measuring the phase nonreciprocity in a passive ring resonator using a light source of low coherence is described. The method provides effective suppression of noise from the backscattering of light in the ring resonator and insensitivity of the interferometer to excursions of the resonance frequencies of the resonator due to reciprocal effects (e.g., thermal expansion) and also permits modulation and compensation of the phase nonreciprocity by using a device outside the resonator to shift the frequency of the light. One version of a low-coherent resonance ring interferometer is examined, viz., a two-transit asymmetric interferometer with a rotating mirror. © 1998 American Institute of Physics. [S1063-7850(98)00409-1]

Optical ring interferometers are widely used in physics and technology, mainly as optical rotation sensors.¹ Recently more and more attention is being devoted to ring interferometers based on passive Fabry–Perot ring resonators (passive resonance ring interferometers, or PRRIs). PRRIs have a number of important advantages over ring lasers and Sagnac interferometers; in contrast to the first there is no locking of counterpropagating modes in them, and unlike the second they are many times more sensitive at the same dimensions of the sensitive loop. Interest in PRRIs is also being stimulated by the advent of optical ring resonators with exceptionally high Q factors; today there are known mirror ring resonators with a finesse $F \sim 10^6$ (Ref. 2), and fiber-optic ones with $F \sim 10^3$ (Ref. 3). One expects that PRRIs will find wide application in physics and engineering if the difficulties still present can be overcome. The greatest difficulties stem from the high noise level of the interference of backscattered light in the ring resonator and from the sensitivity of PRRIs to excursions of the resonance frequencies of the ring resonator owing to reciprocal effects, e.g., thermal expansion. The main reason that these difficulties arise is due to the use of highly coherent light sources with spectra much narrower than the resonance of the ring resonator.⁴

In this paper we describe a new method of measuring the phase nonreciprocity in PRRIs, based on the use of wide-band light sources such as superradiant diodes, the spectral width of which spans many resonances of the ring resonator. The basic idea of the method is illustrated in Fig. 1, which shows one of the possible layouts of a PRRi with a wide-band light source (a fiber-optic version). Light from the source S passes through a 50% coupler C and a weak coupler C_1 and enters the ring resonator R , through which it travels in a clockwise direction, and then is coupled out through coupler C_2 , is sent through a frequency shifter FS , reflects off a rotating mirror RM , passes once again through the frequency shifter FS , and returns to the resonator, but now in a counterclockwise direction, is coupled out through coupler C_1 , and passes through coupler C onto a photodetector PD . It is known that the transmission spectrum of a high-Q optical resonator is a set of narrow lines of transpar-

ency, the center frequencies of which are the eigenfrequencies of the resonator and whose width is F times smaller than the distance between adjacent lines (Fig. 2). For this reason, all the light power incident on the rotating mirror will be concentrated in the transmission lines of the resonator for the clockwise directions. In the presence of phase nonreciprocity these lines turn out to be shifted relative to the transmission lines of the resonator for the counterclockwise direction, and that leads to a decrease in the illuminance at the photodetector on account of the decrease in the area of overlap between the lines of radiation entering the resonator from the rotating mirror and the transmission lines of the resonator in the counterclockwise direction. The frequency shift imposed on the light by the frequency shifter FS upon reflection from the rotating mirror also has the same effect. The total light power reaching the photodetector is

$$P_{\text{out}} = \int \frac{1}{2} T^-(\omega) T^+(\omega + \Omega) \frac{1}{2} P_0(\omega) d\omega, \quad (1)$$

where ω is the frequency of the light, $P_0(\omega)$ is the spectrum of source I ; Ω is the frequency shift imposed on the light by the frequency shifter FS ; $T^\pm(\omega)$ is the transmission spectrum of the ring resonator in the clockwise (+) and counterclockwise (–) directions. In the case when the dispersion of the refractive index in the material of the sensitive loop and the dependence of the phase nonreciprocity on the frequency of the light can be neglected, the expression for the output power takes the form

$$P_{\text{out}}(\Delta\Phi) = \frac{\pi}{16F} \frac{P_0}{1 + (F/\pi)^2 \sin^2(\Delta\Phi/2)}, \quad (2)$$

where $P_0 = \int P_0(\omega) d\omega$ is the total power of the source, F is the finesse of the ring resonator, which is determined by the coupling coefficient K in the couplers C_1 and C_2 and by the value S of the relative loss per pass through the resonator:

$$F \approx \frac{\pi}{K + S}; \quad (3)$$

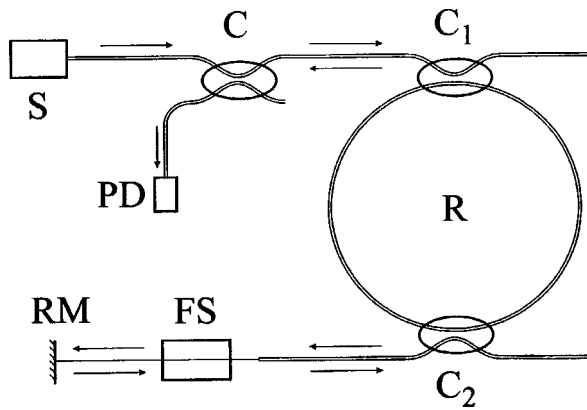


FIG. 1.

and $\Delta\Phi$ is the total effective phase nonreciprocity per round trip:

$$\Delta\Phi = \Delta\phi + \Delta\phi_{\text{eff}}, \quad (4)$$

where $\Delta\phi$ is the phase nonreciprocity in the resonator, and $\Delta\phi_{\text{eff}}$ is the effective nonreciprocity due to the frequency shift of the light upon reflection from the rotating mirror:

$$\Delta\phi_{\text{eff}} = 2\pi \frac{nL}{c} \Omega, \quad (5)$$

where n is the refractive index of the ring resonator, L is its perimeter, and c is the speed of light in vacuum.

We note that the phase nonreciprocity in the resonator, $\Delta\phi$, and the effective nonreciprocity due to the frequency shift on reflection from the rotating mirror, $\Delta\phi_{\text{eff}}$, appear in the expression (2) for the output power in absolutely the same way. Because of this, modulation and compensation of the phase nonreciprocity can be achieved by means of a light frequency shifter FS placed between the resonator and the rotating mirror, so that the parasitic nonreciprocity in the frequency shifter will not affect the operation of the interferometer. Using for the compensating element a constant-frequency-shifting device controlled by a sinusoidal voltage, e.g., a Bragg acousto-optic cell, one can create a compensated PRRI with frequency output.

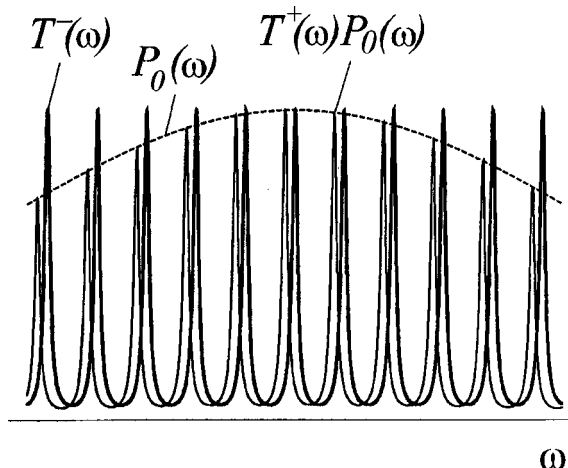


FIG. 2.

The fundamental limit of observation of phase nonreciprocity is determined by the shot noise of the light source:

$$\Delta\phi_{\text{sn}} \approx 25 \sqrt{\frac{\hbar c \pi}{\lambda_0 \tau \eta F P_0}}, \quad (6)$$

where \hbar is Planck's constant, λ_0 is the center wavelength of the light source, τ is the averaging time, and η is the quantum yield of the photodetector. In a Sagnac effect measurement the limit of observation of a rotation is

$$W_{\text{sn}} \approx \frac{c}{A} \sqrt{\frac{\hbar c \pi \lambda_0}{\tau \eta F P_0}}, \quad (7)$$

where A is the area enclosed by the ring resonator. For $A = 1 \text{ m}^2$, a finesse of the resonator $F = 100$, a wavelength $\lambda_0 = 1.5 \text{ }\mu\text{m}$, a source power $P_0 = 100 \text{ mW}$, and an averaging time $\tau = 1 \text{ s}$, one gets $W_{\text{sn}} \approx 3 \times 10^{-8} \text{ rad/s}$. The limiting sensitivity of the interferometer proposed here is higher than for a Sagnac interferometer by a factor of $F^{1/2}$ and lower by the same factor than for a resonance ring interferometer for monochromatic light. The latter circumstance is due to the fact that only a $1/F$ fraction of the source power is utilized in the proposed interferometer. Under conditions such that the noise of the interferometer is significantly higher than the shot noise, the improvement in sensitivity in comparison with nonresonance ring interferometers turns out to be the same as in resonance interferometers for monochromatic light, i.e., approximately a factor of F .

The main advantages of the proposed method over the existing schemes derive from the use of a broad-spectrum source and consist in the following. First, the proposed method does away with the noise due to parasitic interference of the backscattered light in the sensitive loop, which is the main factor degrading the characteristics of ring interferometers for coherent light. Second, as can be seen from formula (2), the proposed interferometer is practically insensitive to excursions of the resonance frequencies of the resonator due to reciprocal effects, e.g., thermal expansion of the resonator, unlike schemes with a monochromatic source, where the resonance frequency must be strictly tied to the frequency of the source. This increases the stability of the interferometer and makes it unnecessary to tune the resonator exactly to the center frequency of the source. In addition, the proposed method affords the possibility of achieving modulation and compensation using a device located outside the ring resonator, which permits lowering the modulation noise, and also to create compensated interferometric schemes with frequency output. It may be hoped that the proposed method will find application in optical gyroscopy, where it can be used to create fiber-optic and integrated optic resonance gyroscopes with significantly improved characteristics, and also in basic physical research on nonreciprocal optical elements.

¹W. W. Chow, V. E. Sanders *et al.*, *Rev. Mod. Phys.* **57**, 61 (1985).
²R. Anderson, H. R. Bilger, and G. E. Stedman, *Am. J. Phys.* **62**, 975 (1994).
³Z. K. Ioannidis, R. Kadivar, and I. P. Giles, *J. Lightwave Technol.* **14**, 377 (1996).
⁴K. Iwatsuki, K. Hotate, and M. Higashiguchi, *Appl. Opt.* **23**, 3916 (1984).

Improvement of the conducting parameters of $\text{YBa}_2\text{Cu}_3\text{O}_x$ films grown on sapphire through the use of a strontium titanate buffer layer

G. A. Ovsyannikov, A. D. Mashtakov, P. B. Mozhaev, F. V. Komissinskiĭ, Z. G. Ivanov, and P. Larsen

*Institute of Radio Engineering and Electronics, Russian Academy of Sciences, Moscow, Russia
Chalmers Technical University, Göteborg, Sweden*

(Submitted March 6, 1998)

Pis'ma Zh. Tekh. Fiz. **24**, 30–35 (September 12, 1998)

High- T_c superconducting films of $\text{YBa}_2\text{Cu}_3\text{O}_x$ on sapphire with an additional buffer layer of strontium titanate (actually, on heterostructures $(100)\text{SrTiO}_3/(001)\text{YBa}_2\text{Cu}_3\text{O}_x / (100)\text{CeO}_2/(11\bar{0}2)\text{Al}_2\text{O}_3$) are obtained by laser deposition, and their superconducting characteristics are investigated. It is shown that buffering the sapphire by a strontium titanate film can raise the critical temperature of the $\text{YBa}_2\text{Cu}_3\text{O}_x$ films by two degrees and give a severalfold increase in the critical current density. © 1998 American Institute of Physics. [S1063-7850(98)00509-6]

Strontium titanate SrTiO_3 (STO) is one of the best substrate materials for growing epitaxial high- T_c superconducting (HTSC) films. It has a cubic crystal lattice of the perovskite type with a lattice parameter $a = 0.3904$ nm that is only slightly ($< 2.5\%$) different from the lattice constants a and b of the basal plane of the HTSC $\text{YBa}_2\text{Cu}_3\text{O}_x$ (YBCO). The coefficient of linear thermal expansion of STO ($9.4 \times 10^{-6} \text{ K}^{-1}$) is also close to that of YBCO ($12 \times 10^{-6} \text{ K}^{-1}$). The shortcomings of STO — its high dielectric constant and high microwave losses — limit its use in microwave technique. For such purposes sapphire and silicon are more suitable substrate materials, and they are considerably cheaper as well. When these materials are used, however, it is necessary to employ guard sublayers to prevent the diffusion of atoms of the substrate into the growing HTSC film. One of the most often used materials for a guard sublayer in the deposition of YBCO films on sapphire substrates is cerium oxide CeO_2 , which has a cubic crystal lattice (of the fluorite type) with a lattice parameter $a = 0.541$ nm, differing by less than 1% from a translation along the $[110]$ direction of YBCO. It has been shown (see, e.g., Refs. 1–4) that by using a $(11\bar{0}2)\text{Al}_2\text{O}_3$ (r plane) substrate with a thin (30–50 nm) epitaxial sublayer of CeO_2 one can grow epitaxial films of $(001)\text{YBCO}$ with good structural and electrophysical parameters at temperatures of 700–770 °C. However, increasing the deposition temperature above 800 °C to permit the growth of the highest-quality films on STO substrates causes the properties of the YBCO film to be degraded on account of the chemical interaction between the HTSC film and the CeO_2 guard sublayer.³ To prevent this interaction it has been proposed^{5,6} to use an additional buffer layer of STO. In the present study we have obtained YBCO films on sapphire with an additional buffer layer of STO and have investigated their superconducting characteristics. We have found that buffering the sapphire by

an STO film can raise the critical temperature of YBCO films by two degrees and can increase the critical current density severalfold.

The YBCO, CeO_2 , and STO films were deposited using a KrF excimer laser (output wavelength 248 nm) with an energy at the target of up to 3 J/cm^2 . The pressure in the chamber was maintained constant in the interval 0.03–1 mbar, depending on the material being deposited. The substrate lay at a distance of 50 mm from the target on a heated susceptor, the temperature of which was held constant during the deposition to a precision of 1 °C in the range 750–900 °C. To improve the thermal contact with the heater the substrate was fastened to the susceptor with silver paste. At the end of the deposition the chamber was filled with oxygen to a pressure of 800 mbar and the substrate was cooled to room temperature at a rate of 15 °C/min. The thickness of the deposited films was 20–60 nm for the buffer layers and 120–200 nm for the YBCO film.

The structure of the grown films was investigated by x-ray diffractometry ($\theta/2\theta$ scan). The superconducting parameters of the YBCO films (the critical temperature T_c and the superconducting transition width ΔT_c) were determined from measurements of the magnetic susceptibility of the films and of the temperature dependence of the resistance and critical current of bridges 4–8 μm wide, obtained by ion-beam etching of the YBCO films through a photoresist mask.

Figure 1a shows the diffractograms obtained in a $\theta/2\theta$ scan of a CeO_2/STO buffer layer with a thickness of 430 nm (30+400) on an r -oriented sapphire substrate. The CeO_2 had the (001) orientation; no other orientations were observed at the accuracy of the measurements. The upper STO layer, however, grows in a mixed orientation of (110) and (111). Although the growth of STO films with a predominant (001) orientation on a $\text{CeO}_2/\text{Al}_2\text{O}_3$ heterostructure was reported in Ref. 7, the authors of that paper did not manage to eliminate the growth of extraneous (110) and (111) orientations of STO. It may be that the disruption of epitaxial

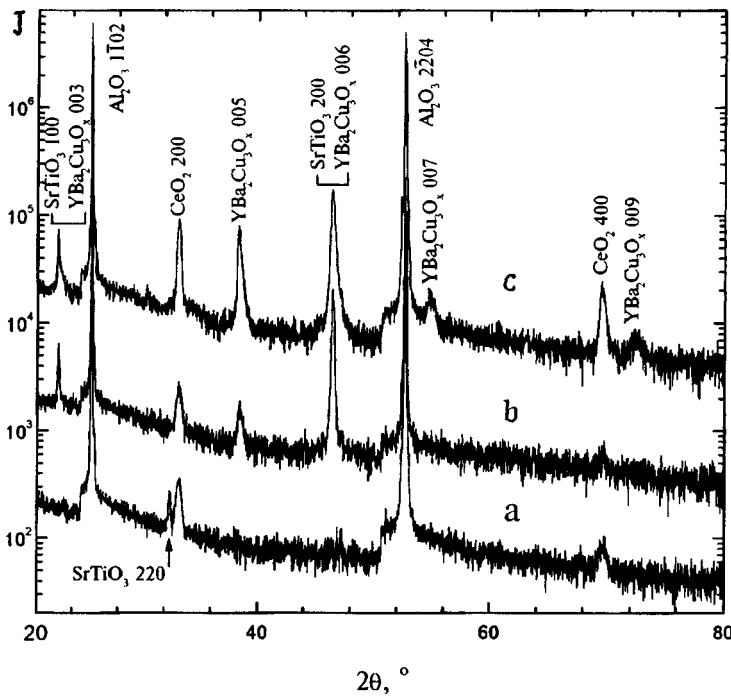


FIG. 1. X-ray diffractograms obtained in a $\theta/2\theta$ scan of the following heterostructures: a — STO-400/CeO₂-30/Al₂O₃; b — STO-200/YBCO-50/CeO₂-30/Al₂O₃; c — YBCO-150/STO-60/YBCO-20/CeO₂-30/Al₂O₃ (the number after the name of the compound is the layer thickness in nm).

growth of STO on CeO₂/Al₂O₃ is caused by the chemical interaction of STO with CeO₂ (Ref. 5). In several studies^{5,6} additional buffer layers have been used to ensure growth of the (001) orientation of STO. Here we have used for this purpose a thin (30 nm) layer of YBCO.

Figure 1b shows the diffractograms obtained in a $\theta/2\theta$ scan of a STO/YBCO/CeO₂/Al₂O₃ heterostructure with a thick upper layer of STO. In addition to the (00*n*) peaks of CeO₂ one observes a pronounced system of (00*m*) peaks of STO, the (002) peak of which is merged with the (006) peak of YBCO. The main contribution to the intensity of that re-

flexion is from the STO, since the thickness of the STO film is substantially greater. A three-layer buffer of this type with a 50 nm thickness of the STO layer was used for the deposition of YBCO films 100–200 nm thick on sapphire. An x-ray diffractogram of the entire heterostructure with an upper layer of YBCO film is shown in Fig. 1c. The lattice constants and half-widths of the most interesting reflections for all the layers of the heterostructure are given in Table I.

The critical temperatures T_c of the superconducting transition of nine of the ten YBCO films deposited on an STO buffer layer lay in the interval 89–90 K, while, as a rule, the

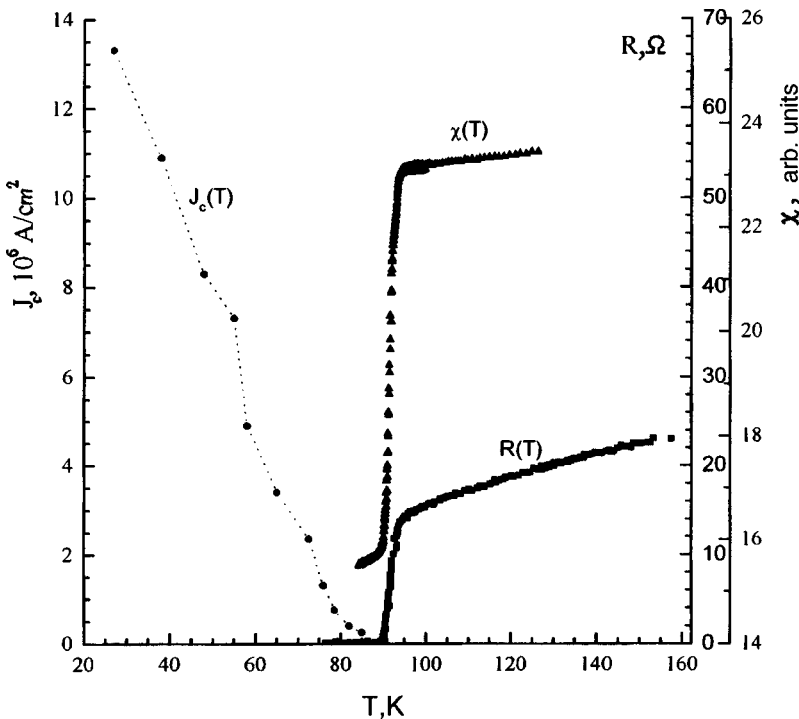


FIG. 2. Temperature dependence of the magnetic susceptibility of a YBCO film on an STO/YBCO/CeO₂/Al₂O₃ heterostructure and of the resistance and critical current of a bridge 7 μ m wide made from the same film.

TABLE I. Crystallographic parameters of the films, determined from the x-ray diffractograms obtained in a $\theta/2\theta$ scan.

Film material	Film thickness, nm	Index of reflection	Lattice parameter, nm	Half-width of reflection, deg
CeO ₂	30	(002)	0.504	0.37
YBCO*	50	(005)	1.171	0.47
STO*	200	(002)	0.391	0.23
YBCO	150	(005)	1.173	0.28

*The parameters of the YBCO and STO buffer layers were determined in a separate experiment.

critical temperature for films deposited on CeO₂ have not exceeded 88 K.^{2,3} Figure 2 shows the dependence of the magnetic susceptibility of YBCO films 120 nm thick and the superconducting parameters (resistance and critical current) of a bridge 7 μm wide made from the same film by ion-beam etching through a photoresist mask. It is seen that the critical temperature of the entire film, as determined from the magnetic measurements ($T_{cm}=88.0$ K), is somewhat lower than the value ($T_{c0}=89.6$ K) determined from the condition of zero resistance of a bridge 7 μm wide. The difference of these temperatures, $T_{cm}-T_{c0}=1.6$ K, together with the width of the resistive superconducting transition $\Delta T_c=2.8$ K, defined as the temperature interval between the 0.9 and 0.1 levels of the resistance of the bridge for $T>T_c$, can serve as a measure of the nonuniformity of the superconducting parameters of the film over the area of the substrate. The superconducting critical current density j_c has a value of 2×10^6 A/cm² at liquid-nitrogen temperature and increases almost linearly with decreasing temperature, reaching a value of 1.4×10^7 A/cm² at liquid-helium temperature (Fig. 2). We note that in the case of a single-layer CeO₂

buffer on sapphire, j_c was equal to 10^6 A/cm² at $T=77$ K.

Thus we have shown experimentally that the use of a complex buffer with an upper layer of strontium titanate makes it possible to grow epitaxial films of the HTSC YBCO of higher quality than can be grown on a single buffer layer of cerium oxide. The proposed method can be used in the growth of HTSC films of YBCO for passive microwave electronics (filters, resonators, switches, etc.). By varying the thicknesses and deposition conditions of the buffer layers — in particular, by depleting the STO of oxygen to lower its dielectric constant⁸ — one can regulate the parameters of microwave devices on sapphire.

The authors thank Yu. V. Bořov, D. Winkler, and I. M. Kotelyanskiĭ for a helpful discussion.

This study was supported in part by the government program of the Russian Federation ‘‘Topical HBLs in Condensed-Matter Physics,’’ subdivision ‘‘Superconductivity,’’ by the Russian Fund for Fundamental Research, and by the program INKO-Copernicus of the European Union.

¹I. M. Kotelyanskiĭ, V. A. Luzanov, Yu. M. Dikaev *et al.*, Sverkhprovodimost' (KIAE) 7, 1306 (1994).

²P. B. Mozhaev, G. A. Ovsyannikov, and Ĭ. L. Skov, Zh. Tekh. Fiz. (1998), in press.

³A. D. Mashtakov, I. M. Kotelyanskiĭ, V. A. Luzanov, P. B. Mozhaev, G. A. Ovsyannikov, and I. D. Bdikin, Pis'ma Zh. Tekh. Fiz. 23(19), 8 (1997) [Tech. Phys. Lett. 23(10), 738 (1997)].

⁴A. G. Zaitsev, R. Kutzner, and R. Wordenweber, Appl. Phys. Lett. 67, 2723 (1995).

⁵Yu. A. Boikov and Z. G. Ivanov, J. Alloys Compd. 251, 193 (1997).

⁶Nicoletti and Villigier, IEEE Trans. Appl. Supercond. AS-7, 1399 (1997).

⁷E. K. Gol'man, V. E. Loginov, A. M. Prudan, and S. V. Razumov, Pis'ma Zh. Tekh. Fiz. 21(21), 84 (1995) [Tech. Phys. Lett. 21(11), 899 (1995)].

⁸M. Hitani, K. Imagawa, and K. Takagi, Jpn. J. Appl. Phys. 34, 254 (1995).

Translated by Steve Torstveit

Influence of accidental impurities and defects on the low-frequency dielectric relaxation in the ferroelectric $\text{Cd}_2\text{Nb}_2\text{O}_7$

N. N. Kolpakova, M. Wiesner, A. O. Lebedev, P. P. Syrnikov, and V. A. Khramtsov

A. F. Ioffe Physicotechnical Institute, Russian Academy of Sciences, St. Petersburg

Adam Mickiewicz University, 61-614 Poznan, Poland

(Submitted January 24, 1998)

Pis'ma Zh. Tekh. Fiz. **24**, 36–44 (September 12, 1998)

It is shown that accidental impurities and structural defects (cation vacancies) formed in the $(\text{CdO}_8)^{n-}$ sublattice during synthesis enhance the relaxation properties of the system near T_{Curie} and suppress the ferroelectric phase transition. © 1998 American Institute of Physics.

[S1063-7850(98)00609-0]

The relaxor behavior of ferroelectric materials has stimulated enormous interest both from the standpoint of elucidating the microscopic mechanism of the extraordinary dielectric relaxation and ascertaining the interrelationship between the ordered (ferroelectric) and disordered (relaxor) states of the system^{1–4} and also in connection with diverse applications of ferroelectric materials in electronics and modern device engineering, where their electrical properties and domain structure are utilized.^{4–6}

A characteristic feature of all relaxor systems is a certain degree of disorder of the crystal structure. Relaxor behavior of solid solutions of the $\text{Pb}(\text{Mg}_{1/3}\text{Nb}_{2/3})\text{O}_3$, $\text{Pb}(\text{Sc}_{1/2}\text{Ta}_{1/2})\text{O}_3$, and $(\text{Pb},\text{La})(\text{Zr},\text{Ti})\text{O}_3$ with the perovskite structure (phase formula AMO_3 , $\text{O}_h^1\text{-Pm}3\text{m}$) is due to the nonuniform distribution of the different species of cations in the M sites and is enhanced in the presence of cation vacancies in the A sites.^{1–4} The relaxor behavior of $\text{Cd}_2\text{Nb}_2\text{O}_7$, which has the pyrochlore structure (general formula $\text{A}_2\text{M}_2\text{O}_6\text{Z}$, $\text{O}_h^7\text{-Fd}3\text{m}$), is ascribed to disorder in the orientation of the chains of dipoles $\text{O}(7)\text{-Cd-O}(7)$ along axes of the $[111]_{\text{cub}}$ type owing to the dynamic displacements of the Cd^{2+} ions relative to the central positions in the $(\text{CdO}_8)^{n-}$ sublattice.^{7,8} The nature of the structural disorder in this material suggests a strong influence of accidental impurities and vacancies in the A sites on the behavior of the dielectric relaxation. This is also indicated by a number of experimental facts that have not yet received the requisite attention and have therefore escaped study. For example, the maximum dielectric constant ϵ'_{max} in this compound, according to different investigators,^{8–11} ranges from 1500 to 20 000. Another peculiarity is that crystals grown in different runs have different coloration (colorless, yellow, orange), apparently on account of uncontrolled impurities and lattice defects arising in the synthesis.^{8,9,12–14} At the same time, the existence of a relation between these characteristics of the material could provide information about the role played by disruptions of the $(\text{CdO}_8)^{n-}$ and $(\text{NbO}_6)^{n-}$ sublattices in the relaxor behavior of the system and about the transformation of the relaxor and ferroelectric states. To shed some light on these questions we have in the present study performed an x-ray structural analysis of crystals of different colors and an investigation of

the optical absorption (340–700 nm) and dielectric response of the system in the radio frequency range (250 Hz–2 MHz).

The crystals were grown by spontaneous crystallization.^{9,10,13} The solvent used was cadmium borate, in an excess amount so as to compensate for the loss of Cd during synthesis. Analysis of the synthesis conditions showed that when starting materials with the same degree of purity are used, the crystals were colorless in those cases when the synthesis was carried out at 1270 °C with a subsequent slow cooling to 850 °C, but when the synthesis conditions were changed (the temperature of the melt was lowered and/or the rate of cooling was increased) the crystals had yellow or orange coloration to varying intensity.

X-ray powder diffractometry confirmed that the synthesized crystals have the pyrochlore structure, and no other phases were observed (Fig. 1). The lattice parameter of the crystals at room temperature was determined by the method of approximation (the reflections $\overline{1022}$, $\overline{1060}$, $\overline{1062}$, $\overline{1200}$, $\overline{1240}$, $\overline{1066}$, $\overline{1244}$) and with the use of an internal Si standard (the $\overline{1244}$ reflection for $\text{Cd}_2\text{Nb}_2\text{O}_7$ and 444 for Si). The values of the lattice parameter obtained by the two methods ($a = 10.372 \pm 0.002$) agree with each other. For all the crystals this parameter has the characteristic value for pure $\text{Cd}_2\text{Nb}_2\text{O}_7$ (Ref. 9). The phase transition temperatures in the colorless and colored crystals are also practically the same.^{8,12–14} On the other hand, it is known that upon substitution of more than 0.5 mol.% of the cations in the A or M sites of this pyrochlore, the lattice constant increases and T_c always decreases.⁹ The absence of such changes in the synthesized crystals allows us to regard them as nominally pure, with an impurity content of less than 0.5 mol.%.

According to the optical characteristics, the crystals are divided into three groups (Fig. 2). In the colorless crystals the absorption edge is observed near 350 nm. In the colored crystals the absorption edge is shifted to longer wavelengths, and a wide absorption band appears in the region 380–450 nm. The more intense the coloration of the yellow crystals, the more intense is this band. In the orange crystals this band is more intense and wider (350–520 nm). After annealing in an oxygen atmosphere at 800 °C for 20 h, the spectral composition of the wide band in the yellow crystals became more

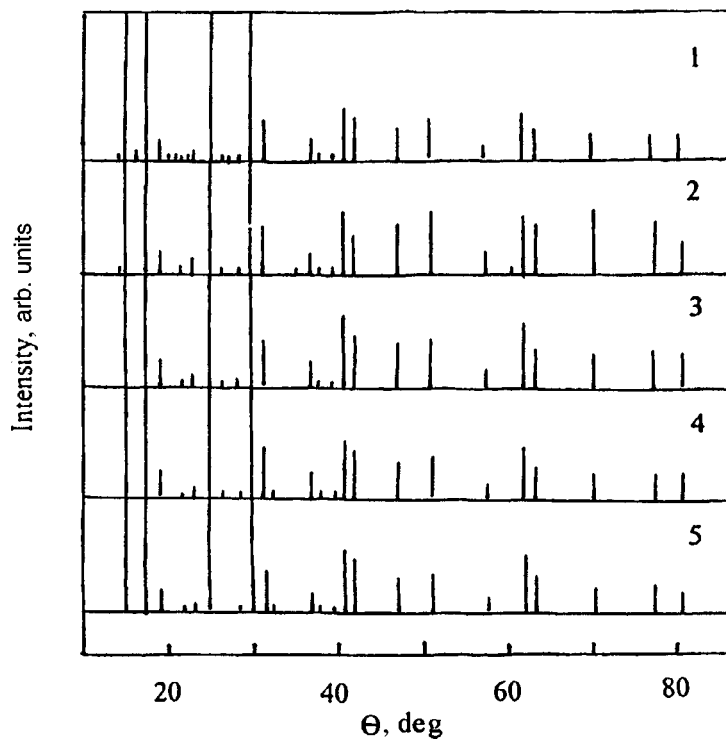


FIG. 1. Line diagram of $\text{Cd}_2\text{Nb}_2\text{O}_7$ crystals of different colors at room temperature (DRON-2 diffractometer, $\text{CuK}\alpha$ radiation): 1 — colorless, 2 — light yellow, 3 — yellow, 4 — orange, 5 — dark orange.

like that typically seen in the orange crystals, while the spectrum of the orange crystals changed less noticeably. Apparently annealing leads to both an ordering of the impurity distribution and to a change in the valence of the impurity ions. The similarity of the behavior of the optical absorption spectra suggests that the same mechanism gives rise to the wide bands and, accordingly, to the accidental impurities and defects in the crystals of different colors. This refers first of all to those impurities and defects which are due to the features of the material being synthesized and of the synthesis technology. In $\text{Cd}_2\text{Nb}_2\text{O}_7$ one has the interesting limiting case in which the M^{5+} cation (0.66 Å) has the maximum and the A^{2+} cation (0.99 Å) the minimum admissible radius for formation of the pyrochlore structure.^{9,15} Since borates are used in the synthesis, the boron ions B^{3+} (0.2 Å), owing to their very small size, can occupy the A sites simultaneously with the cadmium ions, causing a noncentral displacement

of the latter. The cadmium ions can also be replaced by substituent ions with variable valence, Fe^{3+} (0.67 Å), Fe^{2+} (0.80 Å) (the orange crystals),¹⁴ Nb^{4+} (0.67 Å), Nb^{2+} (0.95 Å),¹² or V^{3+} (0.67 Å), V^{2+} (0.72 Å) (the yellow crystals) as accidental impurities. In the presence of B^{3+} ions such a substitution not only preserves the stability of the structure but increases the disorder of the structure in respect to the composition of the cations and the dynamic displacements and gives rise to vacancies in the A sites because of the smaller total ionic radius.^{2,3} It is not ruled out that there are also defects in the form of Cd and O vacancies in an amount not affecting the stoichiometry of the crystals.^{9,15}

The dielectric response of the system is of the same character in all the investigated crystals (Fig. 3a): the anomalies at $T_s = 205$ K and $T_c = 196$ K correspond to phase transitions, and the peak at $T_{\text{max}} = 190$ K (at a frequency of 1 kHz) corresponds to the relaxation maximum.^{7,8} In the colored

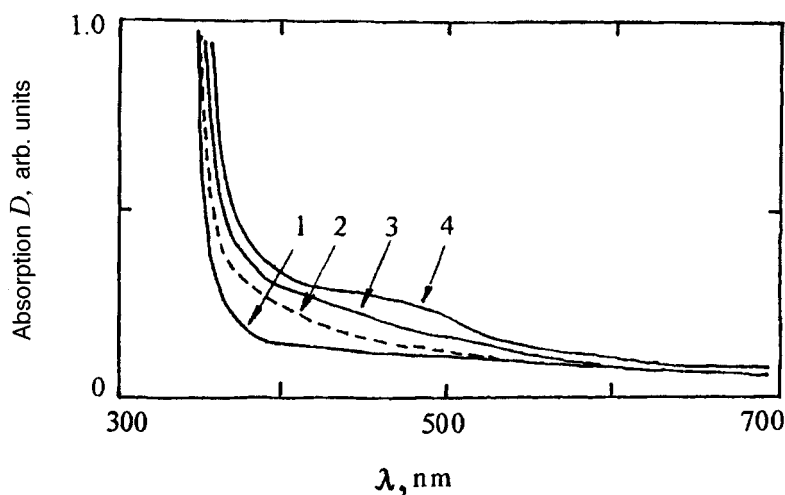


FIG. 2. Optical absorption spectra of crystals of different colors at room temperature (standard Hitachi spectrophotometer): 1 — colorless, 2 — light yellow, 3 — yellow, 4 — orange.

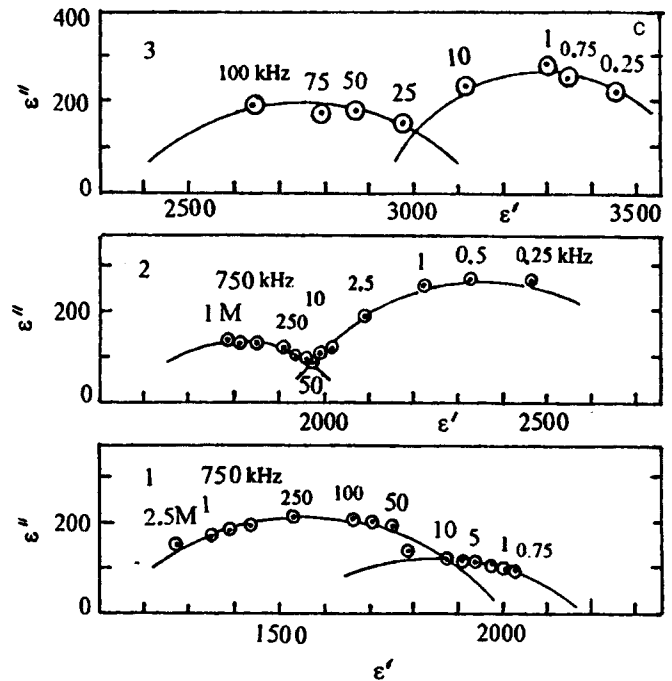
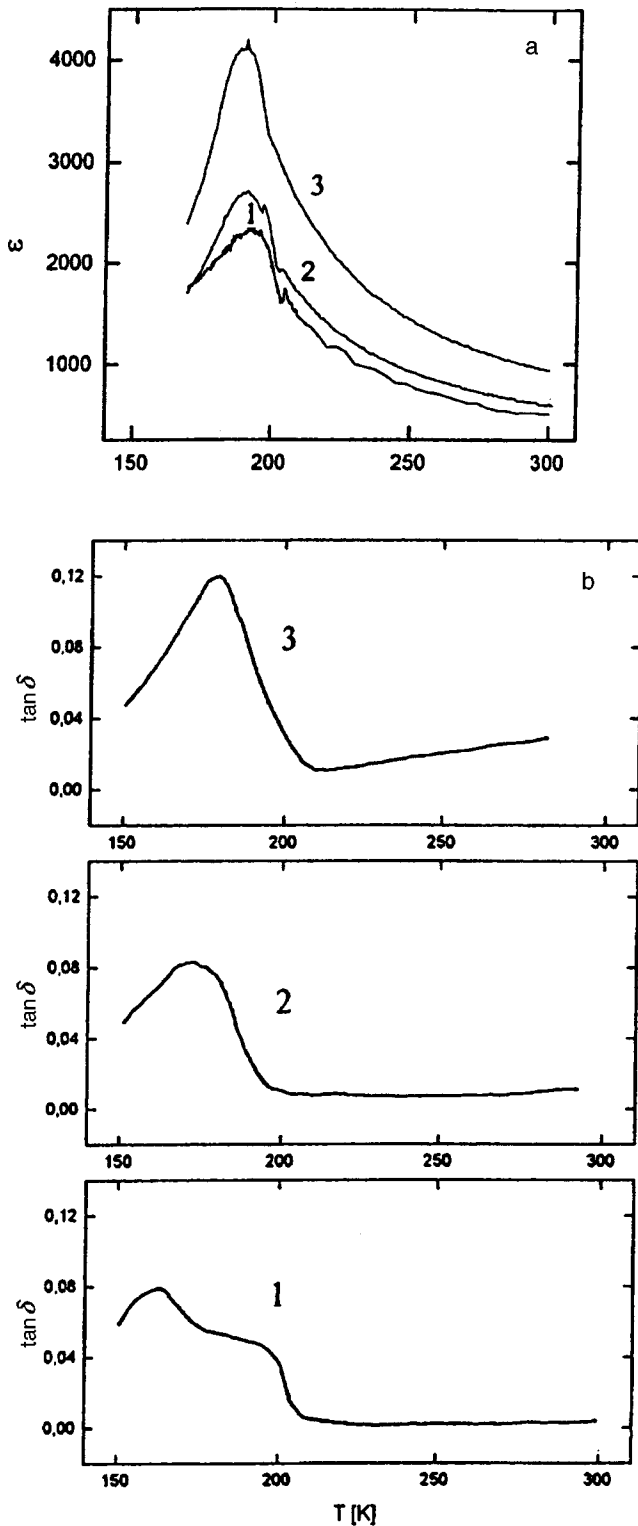


FIG. 3. Temperature dependence of ϵ' and $\tan \delta$ at a frequency of 1 kHz (a,b) and Cole-Cole diagrams at $T = 180$ K near the relaxation maximum $T_{\max} < T_c$ (c) for crystals of different colors. Natural slabs of the $(111)_{\text{cub}}$ type with deposited Au electrodes were investigated with an HP-4284A capacitive bridge. $E_{\text{ac}} = 2$ V/cm. The rate of cooling and heating was 0.5 K/min. 1 — Colorless, 2 — yellow, 3 — dark orange.

crystals, however, the value of $\epsilon(T)$ is greater than in the colorless crystals (especially near T_{\max}), and the maximum at T_{\max} is narrower; the maximum in the temperature dependence of $\tan \delta$ in the colored crystals is shifted to higher temperatures. Dielectric relaxation processes due to the relaxor properties of the system (10 kHz–100 Hz)^{7,8} in the orange crystals are dominant even near T_c , and they suppress the contribution of the ferroelectric phase transition (2 MHz–10 kHz) (Fig. 3). This shows that accidental impurities

(e.g., B^{3+} , Fe^{2+} , Nb^{4+} , Nb^{2+} , V^{2+}) and structural defects (cation vacancies) formed in the $(\text{CdO}_8)^{n-}$ sublattice during synthesis increase the degree of disorder of the structure in this sublattice and enhance the relaxor properties of the system. A direct confirmation of such an interrelationship would come from analysis of the chemical composition and structure of the crystals by the method of analytical electron microscopy (TEM) (see, e.g., Ref. 16). The evolution of the

dielectric relaxation processes upon substitution of atoms of smaller radius (in view of the size of the boron ions) for less than 0.5 mol.% of the Cd^{2+} ions also indicates that the dynamic displacements of the cations in the $(\text{CdO}_8)^{n-}$ sublattice underlie the relaxor behavior of this system.

This study was done with the financial support of the Russian Fund for Fundamental Research (Project 97-02-18099).

- ¹G. A. Smolensky, V. A. Isupov, A. I. Agranovskaya, and S. N. Popov, *Fiz. Tverd. Tela (Leningrad)* **2**, 2909 (1960) [*Sov. Phys. Solid State* **2**, 2584 (1961)].
- ²F. Chu, I. M. Reaney, and N. Setter, *J. Am. Ceram. Soc.* **78**, 1947 (1995).
- ³X. Dai, A. DiGiovanni, and D. Viehland, *J. Appl. Phys.* **74**, 3399 (1993).
- ⁴L. Cross, *Ferroelectrics* **76**, 241 (1987).
- ⁵J. F. Scott, *Ferroelectrics* **183**, 51 (1996).
- ⁶A. Hirt, *Ferroelectrics* **201**, 1 (1997).
- ⁷N. N. Kolpakova, M. Wiesner, G. Kugel, and P. Bourson, *Ferroelectrics* **190**, 179 (1997).

- ⁸N. N. Kolpakova, M. Wiesner, G. Kugel, and P. Bourson, *Ferroelectrics* **201**, 107 (1997); *Ferroelectrics Commun.* **1**(3), 10 (1997).
- ⁹F. Jona, G. Shirane, and R. Pepinsky, *Phys. Rev.* **98**, 903 (1955).
- ¹⁰V. A. Isupov and G. I. Tarasova, *Fiz. Tverd. Tela (Leningrad)* **25**, 1018 (1983) [*Sov. Phys. Solid State* **25**, 587 (1983)].
- ¹¹S. L. Swartz, C. A. Randall, and A. S. Bhalla, *J. Am. Ceram. Soc.* **72**, 637 (1989).
- ¹²P. A. Markovin, R. V. Pisarev, E. S. Sher, and B. N. Shermatov, *Fiz. Tverd. Tela (Leningrad)* **25**, 3642 (1983) [*Sov. Phys. Solid State* **25**, 2096 (1983)].
- ¹³M. L. Charters, *Growth and Investigation Ferroelectric Cadmium Niobate Single Crystals*, Ph. D. Thesis, Rutgers University, New Jersey; Ph. D. Thesis, Ann Arbor, Michigan (1960).
- ¹⁴J. Minge, S. Waplak, and N. N. Kolpakova, *Material Science* **17**, 41 (1991).
- ¹⁵E. Aleshin and R. Roy, *J. Am. Ceram. Soc.* **45**, 18 (1962).
- ¹⁶G. Drazic and M. Kosec, *Ferroelectrics* **201**, 23 (1997).

Translated by Steve Torstveit

Spectral aspect of the onset of subharmonic Shapiro steps in a chain of Josephson junctions connected in parallel

A. V. Arzumanov, V. K. Kornev, K. I. Konstantinyan, and G. A. Ovsyannikov

*M. V. Lomonosov Moscow State University, Moscow
Institute of Radio Engineering and Electronics, Moscow
(Submitted February 27, 1998)*

Pis'ma Zh. Tekh. Fiz. **24**, 45–52 (September 12, 1998)

A chain of parallel-connected Josephson elements described by a resistive model is considered as a model for high-temperature Josephson junctions. The calculated spectra of the Josephson generation can account for the experimentally observed subharmonic Shapiro steps on the current–voltage characteristic and for their aperiodic dependence on the external magnetic field. © 1998 American Institute of Physics. [S1063-7850(98)00709-5]

INTRODUCTION

Josephson junctions formed at the grain boundaries between two high-temperature single-crystal superconducting films with different directions of the crystallographic axes ordinarily have nonhysteretic current–voltage characteristics similar to the typical characteristic of microbridge Josephson junctions. Therefore, weak links of this kind are ordinarily described using the so-called resistive model of a Josephson junction.¹ In the resistive model, applying an external monochromatic rf signal to a Josephson junction will give rise only to harmonic Shapiro steps on the current–voltage characteristic, by virtue of the specific character of the spectrum of Josephson generation in the autonomous regime:

$$V_k \equiv V_k/V_c = 2v/(i+v)^{|k|}, \tag{1}$$

where v_k is the normalized value of the amplitude V_k of the k th harmonic of the voltage $V(t)$ across the Josephson junction, $V_k \equiv I_c R_n$ is the characteristic voltage, I_c is the critical

current, R_n is the resistance in the normal state, $v = V/V_c$, and $i = I/I_c$, where, in turn, I is the dc bias current, and V is the dc component of the voltage. For such a spectrum of the Josephson generation $V(t)$ the spectrum of the inverse quantity $[V(t)]^{-1}$ will contain only the dc component and the fundamental harmonic ($k = 1$). This is the reason why there are only harmonic Shapiro steps, for which the frequency ω of the Josephson generation is an integer multiple n times the frequency of the external signal, where $n = 1, 2, 3, \dots$ (Ref. 1).

At the same time, the experimentally measured current–voltage characteristics of Josephson junctions based on high-temperature superconductors also exhibit large subharmonic steps ($n = 1/2, 1/3, \dots$). There are two approaches taken to explain these results. In one approach the presence of the subharmonic steps is attributed to a nonsinusoidal character of the dependence of the superconducting component of the current on the Josephson phase ω (Ref. 2), whereupon the

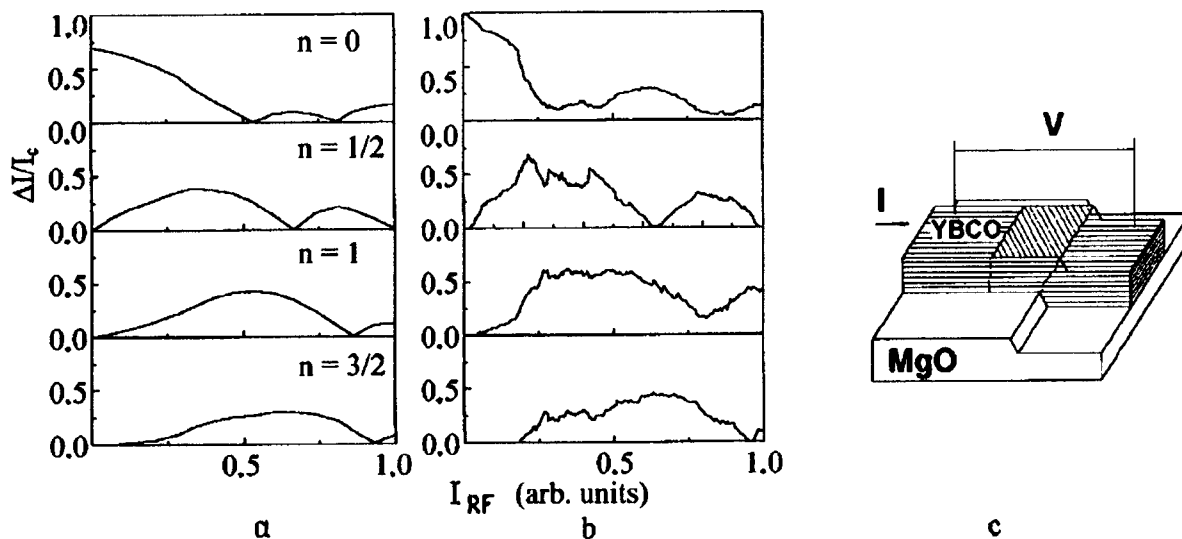


FIG. 1. Height of the Shapiro steps versus the amplitude of the microwave signal at a frequency $\Omega = 1.5\Omega_c$, where the characteristic Josephson frequency $\Omega_c \equiv (2\pi/\Phi_0)I_c R_n$. a: Numerical simulation for a two-junction chain with $l \equiv 6$ and $\Phi_e = \Phi_0/2$; b: experimental results for a YBCO biepitaxial Josephson junction; c: a biepitaxial Josephson junction. The shaded region to the left of the step is rotated in the crystallographic plane $a-b$ by 45° relative to the adjacent regions; this leads to the formation of the Josephson junction.

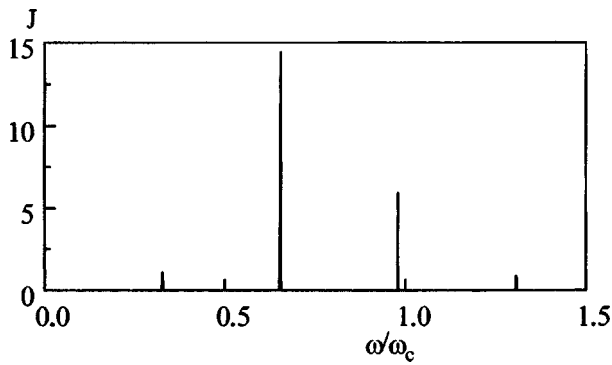


FIG. 2. Spectrum of Josephson generation in a two-junction chain for $l=0.8$ and $\Phi_e = \Phi_0/2$.

expression (1) for the spectral components of the Josephson generation breaks down. In the other approach it is proposed to model the Josephson junction by a chain of parallel-connected Josephson elements, each of which obeys the resistive mode.³⁻⁷

In the present study we investigate the spectrum of Josephson generation for a chain of parallel-connected Josephson elements which obey the resistive model and to explain the causes for the appearance of subharmonic Shapiro steps and the dependence of their amplitude on the strength of the external magnetic field and on the amplitude of the external rf signal.

TWO-JUNCTION CHAIN

Even the simplest model in the form of a two-junction chain of inductively coupled Josephson junctions predicts the appearance of subharmonic Shapiro steps for a specified external field. The calculated dependence of the heights of the Shapiro steps on the amplitude of the microwave signal at a value of the dimensionless inductive parameter $l \equiv (2\pi/\Phi_0)I_c L = 6$, where Φ_0 is the magnetic flux quantum and L is the inductance (Fig. 1a), in this case corresponds rather well to the experimental data, which are shown in Fig. 1b for a YBCO biepitaxial Josephson junction formed on a MgO substrate on which there is a step (Fig. 1c).

In the absence of a magnetic field the chain under consideration is equivalent to a single Josephson junction with a critical current of $2I_c$, since the two Josephson elements

oscillate in-phase, and the spectrum of these oscillations corresponds to expression (1). Specifying the external magnetic flux Φ_e through the loop of the cell gives rise to a phase difference between the oscillations of the Josephson junctions, which for $\Phi_e = \Phi_0/2$ equal to π ; this means that the first harmonics of these oscillations will be 180° out of phase (in antiphase), while the second harmonics will be in-phase. Therefore, because of the interaction between the Josephson elements, the spectrum of Josephson oscillations in the cell will differ appreciably from spectrum (1), for which the amplitudes of the harmonics fall off monotonically with increasing number k of the harmonic, in that the amplitude of the second harmonic is significantly larger and the amplitude of the first harmonic is small (Fig. 2). In this case the frequency spectrum for $[V(t)]^{-1}$ will contain, in addition to the first harmonic, a second harmonic component, which will give rise to subharmonic Shapiro steps on the current-voltage characteristic, which correspond to half-integer ratios of the velocities of the external signal and the Josephson generation ($n = 1/2, 3/2, \dots$).

The external microwave signal in this model will be either in the form a microwave current added to the dc bias current of the chain or in the form of an rf component of the magnetic flux, added to the static external flux Φ_e . In the latter case a circular microwave current arises in the chain, corresponding to the flow of rf currents through the parallel-connected Josephson elements, which oscillate in antiphase. Therefore, the subharmonic step in this case will have a substantially lower height, and the period of its height as a function of the external magnetic flux will be halved (Fig. 3). In our experiment, as in the majority of the published experimental research, the biepitaxial Josephson junction can be regarded as a lumped element in comparison with the wavelength of the rf signal. Therefore, in the subsequent calculations the external microwave signal was always specified in the form of a microwave current added to the bias current.

Unlike the curves shown in Fig. 3 for the heights of the Shapiro steps versus the external magnetic field, the experimentally measured curves have a complicated and aperiodic dependence on the magnetic field.⁵⁻⁷ Therefore, to explain the experimental data we considered a more complex model, in the form of a chain of three inductively coupled Josephson elements.

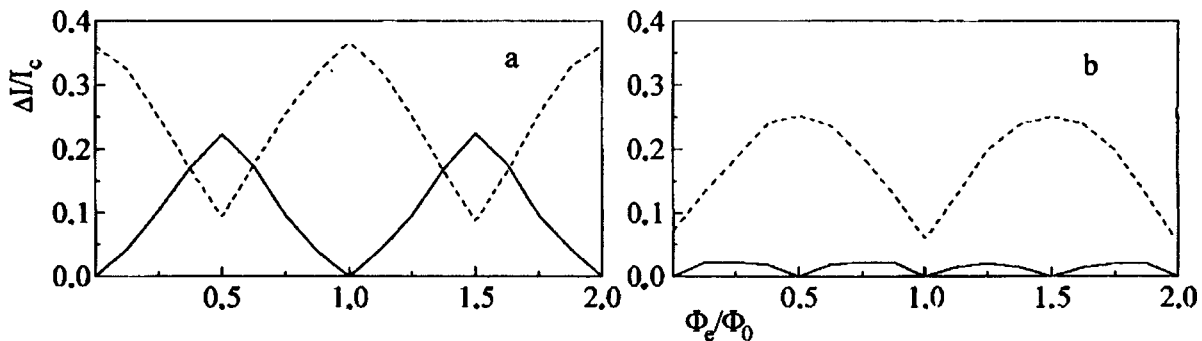


FIG. 3. Height of the Shapiro steps for a two-junction chain with $l=0.8$ and a fixed microwave current amplitude $I_0=0.5I_c$ at a frequency $\Omega=0.7\Omega_c$. a: The microwave current is added to the dc bias current of the chain; b: an alternating component causing a circular microwave current is added to the magnetic flux. The solid curves correspond to $n=1/2$, the dashed curves to $n=1$.

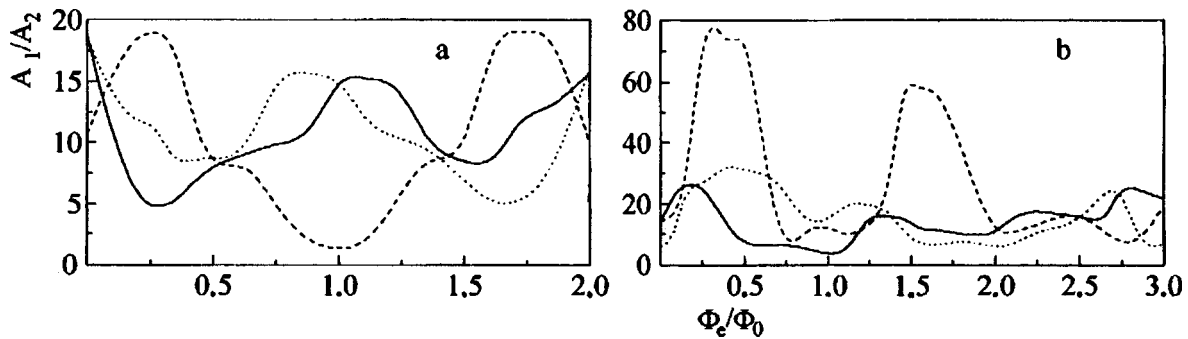


FIG. 4. Ratio of the amplitudes of the first two spectral lines of Josephson generation versus the magnetic flux Φ_e through the outer loop of the three-junction chain at $\Omega = 0.35\Omega_c$ for $l_1 = l_2 = 3$ (a), $l_1 = 2.5$ and $l_2 = 3.5$ (b). The solid curve pertains to the first Josephson element J_1 , the dashed curve to the element J_2 , and the dotted line to the element J_3 .

THREE-JUNCTION CHAIN

In considering a three-junction chain as a model for a high-temperature Josephson junction, to approximate the actual situation the bias current was specified by means of two identical current sources connected to side Josephson elements of the chain J_1 and J_2 . A numerical simulation revealed a strong dependence of the dynamics of the chain on the external magnetic field. Figure 4 shows the ratio of the amplitudes of the first two harmonics A_1/A_2 of the Josephson oscillations for each Josephson element as a function of the magnetic flux through the external loop of the chain, and Fig. 5 shows the analogous dependence of the heights of the first harmonic and subharmonic Shapiro steps at a fixed bias current and a fixed inductance of the external loop $l \equiv l_1 + l_2 = 6$ for various ratios of the arms l_1 and l_2 of the inductive coupling of the elements of the chain. In the case of a symmetric chain ($l_1 = l_2$) these curves are periodic with a period of $2\Phi_0$, which corresponds to a flux Φ_0 through each of the two internal loops of the chain. In the case of an asymmetric chain ($l_1 \neq l_2$) these functions are not periodic. In the presence of strong asymmetry, when, e.g., $l_1 \ll l_2$, a quasiperiod $\Delta\Phi = \Phi_0$ arises. Then the total loop of the chain basically coincides with one of the internal loops, and the three-junction chain thus degenerates into a two-junction chain.

CONCLUSION

In summary, a chain of parallel-connected and inductively coupled Josephson elements each obeying an extremely simple resistive model can serve as an adequate model for a Josephson junction formed at a grain boundary between two single-crystal films of high- T_c superconductors. We have shown that the onset of subharmonic Shapiro steps in the presence of a magnetic field is due to a fundamental change in the spectrum of Josephson generation of the chain in comparison with that of an isolated Josephson element in the framework of the resistive model.

The results obtained in this study also suggest that the complex aperiodic magnetic-field dependence of the height of the Shapiro steps indicates that several superconducting loops with comparable inductance values exist inside a high-temperature Josephson junction. In those cases when a quasiperiodic dependence can be discerned, the Josephson junction contains one main loop having a much larger inductance than the other loops present.

This study was supported in part by the Government Program ‘‘Topical Areas of Condensed-Matter Physics’’ (Project No. 98051) and the ‘‘Integratsiya’’ Academic-Science Center (Project No. 461).

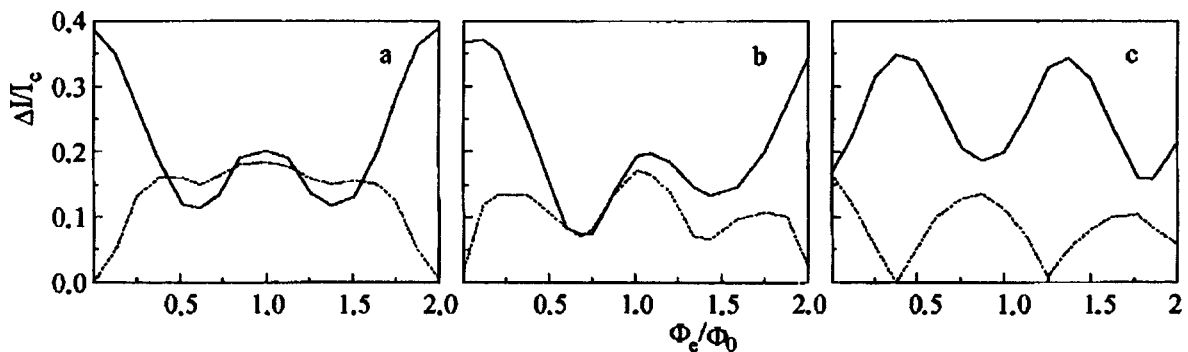


FIG. 5. Height of the Shapiro steps versus the magnetic flux through the outer loop of a three-junction chain at a fixed microwave signal amplitude $I_0 = 0.5I_c$ at a frequency $\Omega = 0.7\Omega_c$ for $l_1 = l_2 = 3$ (a), $l_1 = 2.5$ and $l_2 = 3.5$ (b), and $l_1 = 0.9$ and $l_2 = 5.1$ (c). The solid curve corresponds to the first harmonic Shapiro step ($n = 1$), and the dotted line corresponds to the subharmonic step ($n = 1/2$).

- ¹K. K. Likharev, *Introduction to the Dynamics of Josephson Junctions* [in Russian], Nauka, Moscow (1985).
- ²K. Lee and I. Iguchi, *Proceedings of the 5th International Superconducting Electronics Conference (ISEC'95)*, Japan (1995), pp. 69–71.
- ³R. L. Kautz, S. P. Benz, and C. D. Reintsema, *Appl. Phys. Lett.* **65**, 1445 (1994).
- ⁴I. C. Ku, H. M. Cho, and S. W. Wang, *Physica C* **243**, 187 (1995).
- ⁵E. A. Early, R. L. Sheiner, A. F. Klark, and K. Char, *Phys. Rev. B* **50**, 9409 (1994).
- ⁶D. Terpstra, R. P. J. Ijssesteijn, and H. Rogalla, *Appl. Phys. Lett.* **66**, 2286 (1995).
- ⁷K. Y. Constantinian, G. A. Ovsyannikov *et al.*, *Physica C* **273**, 21 (1996).

Translated by Steve Torstveit

Photodynamic effects in laser Doppler anemometry

Yu. N. Dubnishchev and V. A. Pavlov

Institute of Thermal Physics, Siberian Branch of the Russian Academy of Sciences
(Submitted January 19, 1998)

Pis'ma Zh. Tekh. Fiz. **24**, 53–58 (September 12, 1998)

The first observations of photodynamic effects in laser Doppler anemometry are reported, consisting in the fact that the result of a measurement of the Doppler shift of the frequency of light scattered by a particle depends on the action of the probe light beams on the particle.

© 1998 American Institute of Physics. [S1063-7850(98)00809-X]

Measurement of particle velocities by the Doppler frequency shift in the scattered light is widely used in scientific research and industrial technology. The measurement technique and its various modifications have come to be called laser Doppler anemometry (LDA).¹ One of the chief advantages of this method is that it presumably does not disturb the medium under study during the measurement process. However, the photodynamic effect of the probe laser beams on the kinetics of the scattering particles has not been considered before now. Poynting's familiar words about the light pressure: "Very little experience with attempts to measure the light pressure is needed in order to recognize that it is extremely small — so small that it can be excluded from consideration in earthly matters" (Ref. 2), have been accepted with too little skepticism in a number of measurement technologies, even after the invention of the laser, although research on the dynamical effects of laser radiation on atoms³ and macroparticles² and research on laser thermonuclear fusion⁴ have a long and interesting history.

In this paper we report for the first time the observation of a photodynamic effect in laser Doppler anemometry. The experimental layout is shown in Fig. 1. The apparatus for the measurements is based on a laser anemometer with an adaptive selection of the velocity vector⁵ and contains a laser 1 and, located along the beam path, a quarter-wave plate 2, matching objective 3, acousto-optic traveling-wave modulator 4, objectives 5, 6, and 7, mirrors 8 and 9, cell with optical windows 10, diaphragmed mirror 11, mirror 12, objective 13, and photodetector 14, which is equipped with a field diaphragm 15 and is connected to a signal processing unit 16. An image of the probe field in the cell is recorded by a

video camera 17 through a microscope 18 and is processed on a personal computer 19.

The beam of an argon laser operating at the fundamental mode passes through the quarter-wave plate 2 and is directed by objective 3 into a Bragg acousto-optic traveling-wave modulator 4. Formed at the output of the modulator are the diffracted beams of the zeroth and minus first order, the difference between their frequencies being equal to the modulation frequency (80 MHz). The diffracted beams are directed by objectives 5, 6, and 7 into the cell, where a convective flow of smoke particles is created. The laser beams in the cell are directed counter to each other and interfere to form an interference field whose grating vector **K** (the "sensitivity vector") is given by the difference of the wave vectors **k**₁ and **k**₂ of the interfering beams:¹

$$\mathbf{K} = \mathbf{k}_1 - \mathbf{k}_2, \quad K = 2k = \frac{2\pi}{\Lambda},$$

where $k = 2\pi/\lambda$ and $\Lambda = \lambda/2$. The probe field is localized in the crossing region of the waists of the interfering beams. An image of the probe field in light scattered on smoke particles is formed on the light-sensitive surface of the photodetector 14 by objective 5, mirrors 11 and 12, objective 13, and field diaphragm 15. The photoelectric signal is sent to the electronic processing unit 16.

As we know,¹ the photoelectric signal contains a component whose frequency is a linear function of the difference of the Doppler frequency shifts in the light scattered by a particle from the incident laser beams:

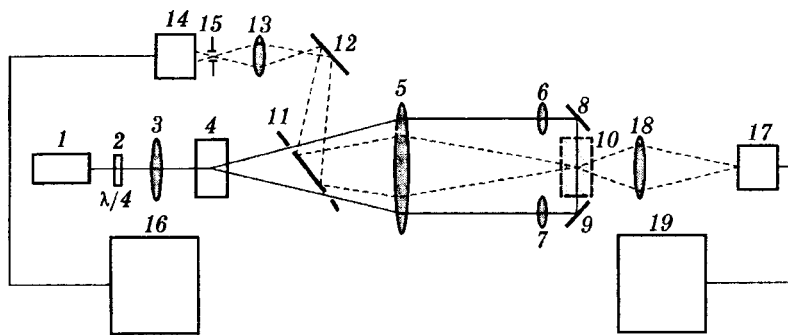


FIG. 1. Diagram of the experimental layout: 1 — laser, 2 — quarter-wave phase plate, 3 — objective, 4 — acousto-optic modulator, 5,6,7 — objectives, 8,9 — mirrors, 10 — cell, 11 — mirror with diaphragms, 12 — mirror, 13 — objective, 14 — photodetector, 15 — field diaphragm, 16 — electronics, 17 — video camera, 18 — microscope, 19 — personal computer.

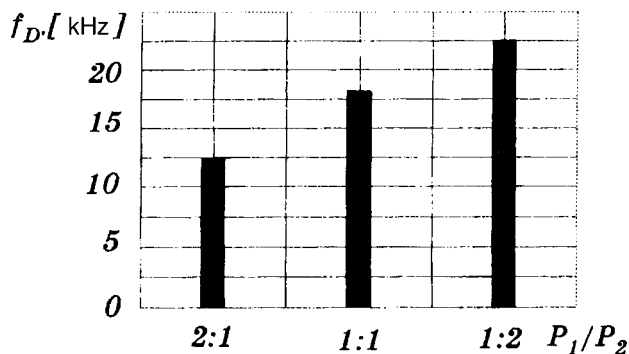


FIG. 2. Average value of the Doppler frequency shift for different ratios of the powers P_1 and P_2 of the probe laser beams.

$$\omega = \Omega_0 + \mathbf{v} \cdot \mathbf{K} = \Omega_0 + \frac{2\pi v}{\Lambda}$$

Here Ω_0 is the difference of the angular frequencies of the diffracted beams at the output of the modulator (the carrier frequency), and \mathbf{v} is the velocity vector of the scattering particle, v is the modulus of the projection of the velocity vector of the particle onto the grating vector \mathbf{K} of the probe field. The electronic unit measures the frequency $f_D = v/\Lambda = 2v/\lambda$, which is proportional to the velocity component to be measured, with a known coefficient of proportionality $2/\lambda$, where for argon laser radiation $\lambda = 0.515 \mu\text{m}$.

Figure 2 shows the values of the measured frequency of the particles for different ratios of the power of the laser beams forming the probe field: 1:1, 2:1, and 1:2. For a 1:1 ratio the average frequency f_D corresponding to the velocity of convection of the smoke particles is 18 kHz ($v = 4.64 \text{ mm/s}$). In the case when the power of the beam with wave vector coinciding with the direction of the velocity v is equal to twice the power of the beam in the opposite direction, the average value of f_D increases to a value of 22.5 kHz ($v = 5.79 \text{ mm/s}$). This means that the particles are accelerated on account of the photodynamic effect. In the situation where the power of the light beam whose wave vector coincides with the particle velocity is one-half the power of the oppositely directed beam, the average value of the frequency f_D falls to 12.5 kHz ($v = 3.22 \text{ mm/s}$). Consequently, the resultant effect of the light beams in this case is to slow the particle.

Figure 3 shows the tracks of particles in the probe field, as recorded by the video camera. The inclined ‘‘point’’ tracks correspond to the convective motion of the particles. The horizontal tracks reflect the motion of the particles under the influence of the probe laser beams at a beam power ratio of two.

An example of the Doppler signal from a scattering particle moving under the influence of laser radiation is shown in Fig. 4. The signal was obtained from a smoke particle in

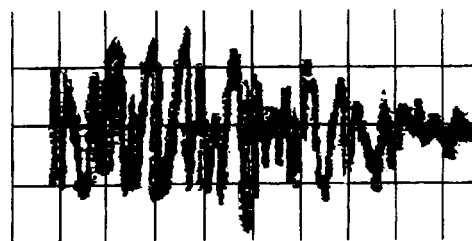


FIG. 4. Doppler signal from a particle moving under the influence of the photodynamic effect in the probe field. $1 \text{ div.} = 2 \text{ ms}$, $v \approx 0.3 \text{ mm/s}$.

the absence of convective flows in the cell.

The results show that in the measurement of small particle velocities (of the order of cm/s and lower) the photodynamic effect of the laser beams on the scattering particle should be taken into account. The influence of the probe field can be manifested in light pressure or photophoresis, which is a consequence of the nonuniform heating of the particle surface and the adjacent medium by a laser beam. It follows that one encounters situations in laser anemometry, especially in the measurement of small velocities, in which the disturbance of the medium under investigation by the probe beam cannot be neglected, and the assumption that the measurements are of a ‘‘nondisturbing’’ character breaks down.

In addition to taking the photodynamic effects into account directly, one must keep in mind when making velocity measurements that different optical configurations of the measuring schemes in laser anemometry have different sensitivities to photodynamic effects. For example, in a differential scheme of LDA with equal powers of the probe beams, the measurement of the velocity component collinear with the grating vector of the probe field is subject to the least influence of the photodynamic effects on account of the counteracting influences of the incident beams, while the influence of the photodynamic effect on the measurement of the orthogonal component will be the greatest. This follows from the formula for the Doppler frequency shift in the differential scheme:¹

$$\omega_D = \mathbf{v} \cdot (\mathbf{k}_1 - \mathbf{k}_2).$$

The same can be said of the inverse-differential scheme,¹ in which the Doppler frequency shift is given by the expression $\omega_D = \mathbf{v} \cdot (\mathbf{k}_{s1} - \mathbf{k}_{s2})$, where the sensitivity vector is defined as the difference of the wave vectors \mathbf{k}_{s1} and \mathbf{k}_{s2} of the scattered beams when they are oriented symmetrically about the wave vector of the incident beam, provided that the scattering indicatrix has axial symmetry.

The highest sensitivity to photodynamic effects is possessed by schemes with a reference beam,¹ for which the Doppler frequency shift is given by the expression $\omega_D = \mathbf{v} \cdot (\mathbf{k}_i - \mathbf{k}_s)$, where \mathbf{k}_i is the wave vector of the beam incident on the particle and \mathbf{k}_s is the wave vector of the scattered

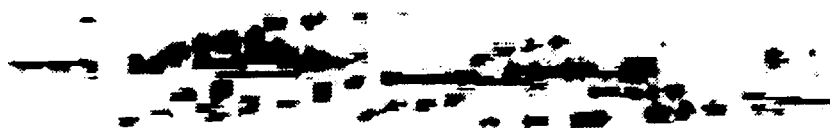


FIG. 3. Photograph of the tracks of particles in the probe field. The radius of the waist is $20 \mu\text{m}$; the power of the laser beams forming the probe field is 20 mW .

beam. In measurements of a three-dimensional velocity vector the optical configuration that is least sensitive to photodynamic effects is that formed by three interference gratings in counterpropagating beams, which form an orthogonal basis. Even here, however, in the case of precision measurements it is necessary to take into account the attraction or repulsion of particles in the cross section of the laser beam in the case of different relative refractive indices of the substance of which the scattering particles are made.

Photodynamic effects in LDA should not be regarded exclusively as complicating factors in measurements. The detection and analysis of photodynamic effects in LDA may serve as a basis for the development of new methods of laser diagnostics, permitting measurement of the parameters of the scattering particles and the medium around them.

The authors thank V. A. Arbuzov and V. G. Meledin for assistance in processing the results.

This study was supported by Grant No. 96-02-19246 From the Russian Fund for Fundamental Research.

¹ Yu. N. Dubnischev and B. S. Rinkevichyus, *Methods of Laser Doppler Anemometry* [in Russian], Nauka, Moscow (1982), 304 pp.

² V. G. Minogin and V. S. Letokhov, *Laser Radiation Pressure on an Atom* [in Russian], Nauka, Moscow (1986), 222 pp.

³ A. Ashkin, *Sci. Am.* **226**(2), 63 (1972).

⁴ G. A. Askar'yan, *Usp. Fiz. Nauk* **110**, 115 (1973) [*Sov. Phys. Usp.* **16**, 414 (1973)].

⁵ P. Ya. Belousov, Yu. N. Dubnischev, V. G. Meledin *et al.*, *Opt. Appl.* **20**, 187 (1990).

Translated by Steve Torstveit

Low-temperature photoluminescence of heavy-ion-implanted InGaP solid solutions

D. Bhattachar-yya, D. A. Vinokurov, G. M. Gusinskiĭ, V. A. Elyukhin, O. V. Kovalenkov, R. N. Kyutt, J. H. Marsh, V. O. Naĭdenov, and E. L. Portnoĭ

*A. F. Ioffe Physicotechnical Institute, Russian Academy of Sciences, St. Petersburg
Glasgow University, Glasgow G128QQ, Scotland, UK*

(Submitted March 3, 1998)

Pis'ma Zh. Tekh. Fiz. **24**, 59–62 (September 12, 1998)

The photoluminescence spectra of samples of the solid solution In(0.5)Ga(0.5)P before and after implantation of high-energy nitrogen ions to doses of 10^{11} – 5×10^{12} cm $^{-2}$ shows that the photoluminescence of the implanted (and annealed) samples may be the result of the formation of essentially one-dimensional semiconductor structures along the individual ion tracks.

© 1998 American Institute of Physics. [S1063-7850(98)00909-4]

There is great interest at present in research on the creation of nanostructures with a large ratio of length to diameter. In this letter we present results that confirm the basic underlying idea of a possible method of creating such structures — the formation of amorphized tracks along the paths of individual heavy ions in an In(0.5)Ga(0.5)P solid solution and the subsequent recrystallization of these tracks, accompanied by decomposition.^{1,2} Epitaxial films of the solid solution In(0.5)Ga(0.5)P grown on GaAs(100) substrates by metalorganic vapor-phase epitaxy (MOVPE) were chosen for implantation for the following reasons. Among the ternary solid solutions of the III–V type with a direct gap structure, the solid solution In(0.5)Ga(0.5)P has the greatest difference in the lattice constant a of the constituent compounds ($a = 5.87$ Å for InP and $a = 5.45$ Å for GaP). Such a difference in the lattice constants makes for a wide zone of immiscibility in these solid solutions, which for the solid solution In(0.5)Ga(0.5)P occurs in the temperature interval 820–900 K.^{1,2} The crystallization of such a solution at lower temperatures under conditions close to thermodynamic equilibrium should lead to the formation of a two-phase solid solution in which one of the phases is enriched in indium phosphide and the other in gallium phosphide. Crystallization under practically thermodynamic equilibrium conditions can be achieved by a prolonged thermal annealing of a single-phase amorphized solid solution, which should lead to a recrystallization process involving the formation of a two-phase single-crystalline solid solution. However, in the recrystallization of a completely amorphized solid solution found in the zone of immiscibility, the size of the regions of different composition will have a large spread of values. Therefore, to limit the spread in values of the dimensions of these regions, the epitaxial films of the solid solution In(0.5)Ga(0.5)P were irradiated by high-energy ions in doses ruling out continuous amorphization. The irradiation by accelerated ions was carried out at the cyclotron of the Ioffe Physicotechnical Institute in St. Petersburg, Russia. In the experiments nitrogen ions (+3) were used for irradiation. An ion energy of 3 MeV was chosen to ensure their penetration to a depth much greater than the thickness of the epitaxial films, which was 0.5 μm. The irradiation doses were varied in the interval

10^{11} – 5×10^{12} cm $^{-2}$, which corresponds to an average distance of 300–50 Å between the centers of the amorphized regions formed by the tracks of individual ions. The PL spectra were measured at 5 K under pumping by an argon laser. In addition, an x-ray structural analysis of the heterostruc-

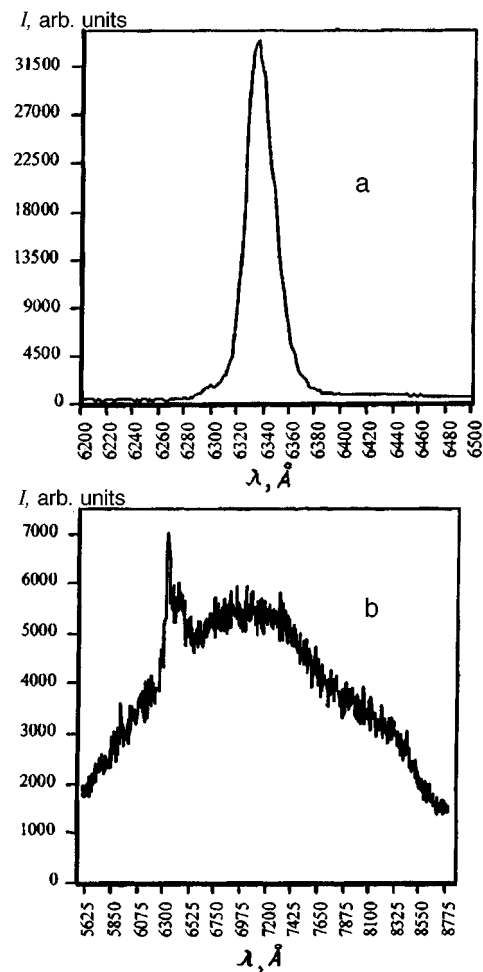


FIG. 1. Photoluminescence spectra of the solid solution In(0.5)Ga(0.5)P at 5 K before implantation and annealing (a) and after implantation by nitrogen ions in a dose of 5×10^{12} cm $^{-2}$ with a subsequent anneal for 8 h at a temperature of 410 °C (b).

tures was carried out prior to the implantation and annealing and again after these procedures. A comparison of the x-ray diffraction curves before and after implantation and annealing confirms that only an insignificant fraction of the volume of the epitaxial films was subjected to amorphization. One can thus assume that on average the transverse cross-sectional diameter of the tracks of the nitrogen ions in the In(0.5)Ga(0.5)P solid solution is considerably less than 50 Å. In addition, the same x-ray spectral investigations showed that annealing substantially decreased the variation of the composition over the thickness of the films in the as-grown heterostructures, a finding which is of great interest in its own right.

The main relationships discerned in the behavior of the PL are the following (see Fig. 1): In all the samples irradiated to the indicated doses there arose a spectral distribution with a maximum at 705 nm and a full width at half maximum (FWHM) of the order of 150 nm, on which was superposed the peak of the unirradiated material (633.5 nm), which was significantly diminished in intensity but maintained its position. The PL spectrum should depend on both the composition and the dimensions of the recrystallized regions. The observed maximum of the spectral distribution in the implanted and annealed samples corresponds to a composition of the bulk solid solution In(0.7)Ga(0.3)P. However, the dimensions and geometry of the recrystallized regions do not permit one to state that the luminescence of the solid solution In(0.7)Ga(0.3)P has been observed. In accordance with the results of Ref. 2, one of the two solid solutions found in equilibrium at the annealing temperature should be In(0.9)Ga(0.1)P. Thus the PL spectrum in the implanted and annealed samples may be the result of the formation of essentially one-dimensional semiconductor objects at the sites

of the tracks formed by nitrogen ions. The rather large width of the distribution can be attributed to the difference in the dimensions of the latent tracks of the ions. Indeed, the mechanism of formation of a latent track of a heavy ion in crystal structures has never been studied. It has been established that the so-called "Coulomb explosion" occurs along the path of a heavy ion, leading to displacements of the lattice ions and the creation of a region of disorder, amorphization, recrystallization, and other effects. All these processes depend on the type of ion and its energy and on the type of structure.³ Most of the processes are of a nonlinear character. It has been shown⁴ that there exists a disproportionately large decrease in the transverse dimensions of the tracks upon switching from uranium ions (an ellipse 21.8×18 nm) to dysprosium ions (12×4.5 nm). The transverse dimensions of the tracks of nitrogen ions are apparently subject to large fluctuations in view of their small sizes. In addition, there may be fluctuations of the ionization density along the length of a track. To elucidate these matters we plan to repeat the experiments with the heavier argon ions.

This study was carried out as part of Project 2-024/4 of the Russian Ministry of Science and Technology program "Physics of Solid-State Nanostructures."

¹ V. O. Naidenov, G. M. Gusinsky, V. A. Elukhin, E. L. Portnoy, and J. H. Marsh, *Abstracts of the 10th International Conference on Surface Modification of Metals by Ion Beams*, Gatlinburg, Tennessee (1997).

² V. A. Elukhin, E. L. Portnoy, E. A. Avrutin, and J. H. Marsh, *J. Cryst. Growth* **173**, 69 (1996).

³ M. Toulemonde, C. Dufour, and E. Paumier, *Phys. Rev. B* **46**, 14 362 (1992).

⁴ J. Vetter, N. Scholz, and N. Angert, *Nucl. Instrum. Methods Phys. Res. B* **91**, 129 (1994).

Translated by Steve Torstveit

Measurement of the thermal and electronic parameters of semiconductors by the "mirage-effect" method with pulsed excitation and splitting of the probe beam

A. N. Petrovskii, K. V. Lapshin, and V. V. Zuev

Moscow Engineering Physics Institute

(Submitted February 13, 1998)

Pis'ma Zh. Tekh. Fiz. **24**, 63–67 (September 12, 1998)

A technique is described which affords a qualitative improvement in the accuracy of determining the thermal and electronic parameters of semiconductor samples. © 1998 American Institute of Physics. [S1063-7850(98)01009-X]

In this paper we propose a novel technique employing the "mirage-effect" method with a splitting of a probe beam which can yield a qualitative improvement in the accuracy of determining the thermal and electronic parameters in the scanning of sample surfaces (including the number of hidden flaws, the quality of surface treatment, the presence of microcracks, impurity levels, etc.); we demonstrate the advantages of this technique and present experimental results on the thermal diffusivity and velocity of propagation of the maximum of the refractive-index gradient for a thermal wave in test samples.

The possibility of measuring the thermal and electronic parameters of semiconductors by the "mirage-effect" method with pulsed excitation, which is particularly promising because of its local, nondestructive, and contactless character — has been demonstrated in a number of papers from Russia and abroad.^{1–4}

The factors which determine the accuracy of the method are the nonuniformity of the illumination of the sample by the exciting radiation from pulse to pulse and the accuracy of measurement of the location of the point of entry of the probe beam into the sample.

The experimental arrangement proposed in this paper (see Fig. 1) can successfully solve both of these problems, significantly improving the accuracy and response time of the method.

A probe beam 1 from a He–Ne laser is shined on the face of a beam splitter 2, which splits it into two beams. The two newly formed probe beams scan the sample 3, which is located in a telescopic system 4, at depths x_1 and x_2 .

The sample is mounted inside the telescopic system on an adjusting stage with a micron drive along the vertical and horizontal axes (the drive has a precision of $10\ \mu\text{m}$). The two-coordinate drive on the adjusting stage permits varying both the depth of the points of entry of the probe beams into the sample and also the distance between the probe beams in the sample (Δx) by moving closer or farther from the waist (of course, the horizontal displacement should not be large, since that would make the diameter of the probe beam in the sample comparable to the scanning depth, and the probe beam could no longer be regarded as uniform).

The deflection of the probe beams after their passage through the telescopic system is registered by two photo-

diodes 5 shielded from stray radiation by silicon filters 6.

The signals from the photodiodes are fed to an S9-16 dual-trace programmable digital oscilloscope 7, which permits their visual comparison, and are then processed using a program for the pulsed photodeflection spectroscopy (PPDS) of the signals from the two probe beams, taken simultaneously during a single exciting pulse (8,9,10).

From the shapes of the PPDS signals taken over a single pulse of exciting laser radiation we calculate the values of the thermal diffusivity D_t and the thermal wave velocity in the samples.

Expressing D_t in terms of the time difference Δt of the positions of the thermal maxima of the PPDS signals from the two probe beams, the scanning depth x_2 of the probe beam more distant from the surface, and the distance Δx between the probe beams in the sample, we have in the simplest approximation¹

$$D_t = \Delta x \cdot x_2 (1 - \Delta x / 2x_2) / 3\Delta t. \quad (1)$$

It is seen from Eq. (1) that the error in determining D_t depends on the uncertainties in determining Δx , Δt , and x_2 , which we shall call $\delta(\Delta x)_{\text{two}}$, $\delta(\Delta t)_{\text{two}}$, and $\delta(x_2)_{\text{two}}$, respectively.

The fact that the parameter Δt in the proposed scheme is independent of the nonuniformity of the illumination of the sample by the exciting radiation makes it possible to improve the accuracy of its determination from 20% (the conventional "mirage" effect) to 2%.

The main parameter influencing the accuracy of measurement of the scanning depth x_2 is the diameter of the probe beam inside the sample (it should be considerably smaller than the scanning depth, since otherwise the nonuniformity of the deflection of the different parts of the probe beam over depth must be taken into account). In the experiment reported here the focal length of the telescope lenses was 3 cm, the sample thickness was around 2 mm, and the diameter of the probe beam at the entrance of the optical system was around 2 mm.

The laser radiation at the entrance and exit of the sample could be observed visually through a night-vision device; the diameter of the probe beams at the entrance to and exit from the sample was $70\ \mu\text{m}$, and inside the sample the distribution of the laser beam maintained its Gaussian profile.⁵ The

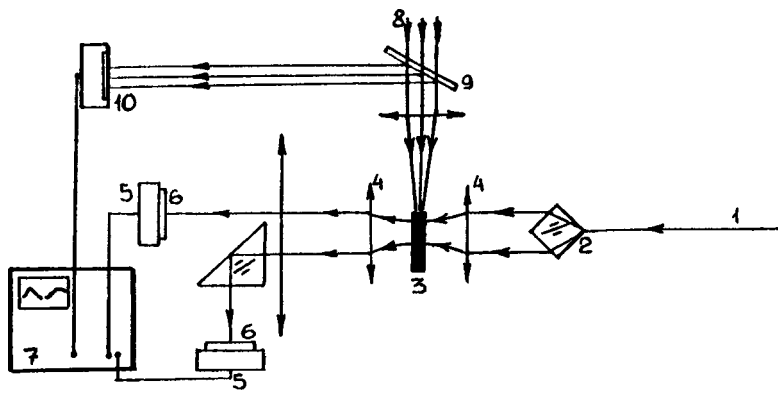


FIG. 1.

physical limitation on the waist of the probe beam was $20 \mu\text{m}$ (Ref. 5). The scanning depth x_2 was chosen as large as possible and equalled $450 \mu\text{m}$, and it was thus significantly larger than the diameter of the probe beam inside the sample. The error $\delta(x_2)_{\text{two}}$ was $\sim 6\%$ (as in the conventional scheme).

In the proposed scheme the distance Δx between the two scanning probe beams is not affected by vertical movement of the sample. The error $\delta(\Delta x)_{\text{two}}$ was $\sim 2\%$, whereas in the conventional scheme the error is determined by the scanning depth x_1 , by the precision of the drives of the adjustable stage, and by the nonuniformity of the illumination of the surface of the sample by the exciting laser radiation: $\delta(x_1)_{\text{one}} \sim 10\%$.

Thus the error in the determination of D_t for one measurement by the method utilizing a split probe beam is $\delta(D_t)_{\text{two}} \sim 10\%$, which is significantly lower than the error in D_t determined by the conventional scheme: $\delta(D_t)_{\text{one}} \sim 40\%$. In addition, the possibility of measuring the parameters of the samples with a single exciting pulse makes this method substantially faster.

The aforementioned advantages of the technique of using a double probe beam make it particularly convenient for scanning the thermal and electronic parameters of a sample over the surface (including for purposes of determining the quality of surface treatment, the presence of microcracks, impurity levels, etc.).

Let us mention another possible application of the split-probe-beam method, viz., a parallel arrangement of the exciting beam and the split probe beams. Such a scheme is convenient for detecting hidden flaws in a sample.

In this study we investigated polished silicon samples with a surface finish of $1-2 \mu\text{m}$, so that the rate of surface

recombination is negligible,² and with minority-carrier lifetimes of $170 \mu\text{s}$ (p type) and $0.7 \mu\text{s}$ (n type).

The thermal diffusivity of the investigated samples was $1.0 \text{ cm}^2/\text{s}$ for the n -type silicon sample (the tabulated value is $1.0 \text{ cm}^2/\text{s}$; Ref. 6) for all of the series, and $0.9-1.4 \text{ cm}^2/\text{s}$ for the p -type silicon sample (the tabulated value is $1.2 \text{ cm}^2/\text{s}$; Ref. 6) for all of the series.

We also made a study of the propagation velocity V_t of the maxima of the gradients of the refractive index of thermal waves in the samples, the theoretical justification for which is given in Ref. 7. Because the measurements are of a relative nature, the error $\delta(V_t)_{\text{two}}$ was around 4% , considerably smaller than the error in the conventional method $\delta(V_t)_{\text{one}} \sim 30\%$. The propagation velocity of the maximum of the refractive-index gradient for a thermal wave was 53 cm/s in the p -type silicon sample with $\tau = 170 \mu\text{s}$ and 98 cm/s in the n -type silicon sample with $\tau = 0.7 \mu\text{s}$.

¹ V. V. Zuev, M. M. Mekhtiev, and D. O. Mukhin *et al.*, MIFI Preprint No. 031-90 [in Russian], Moscow Engineering Physics Institute, Moscow (1990), 24 pp.

² A. N. Petrovsky, A. O. Salnick, V. V. Zuev *et al.*, Solid State Commun. **81**, 223 (1992).

³ K. V. Lapshin, A. N. Petrovskii, and V. V. Zuev, Pis'ma Zh. Tekh. Fiz. **19**(1), 24 (1993) [Tech. Phys. Lett. **19**(1), 9 (1993)].

⁴ K. V. Lapshin, A. N. Petrovskii, and V. V. Zuev, Pis'ma Zh. Tekh. Fiz. **20**(21), 60 (1994) [Tech. Phys. Lett. **20**(11), 880 (1994)].

⁵ L. D. Landau and E. M. Lifshitz, *The Classical Theory of Fields*, 4th Eng. ed., Pergamon Press, Oxford (1975) [cited Russian original, Nauka, Moscow (1988), 512 pp.].

⁶ M. P. Shaskol'skii (Ed.), *Acoustic Crystals* [in Russian], Nauka, Moscow (1982), 632 pp.

⁷ M. M. Mekhtiev, V. V. Zuev, and A. N. Petrovskii, MIFI Preprint No. 014-96 [in Russian], Moscow Engineering Physics Institute, Moscow (1996), 40 pp.

Conversion of Hermite–Gaussian and Laguerre–Gaussian beams in an astigmatic optical system. 1. Experiment

A. N. Alekseev, K. N. Alekseev, O. S. Borodavka, A. V. Volyar, and Yu. A. Fridman

Simferopol State University

(Submitted January 26, 1998)

Pis'ma Zh. Tekh. Fiz. **24**, 68–73 (September 12, 1998)

The workings of a mode converter providing energy-effective conversion of an Hermite–Gaussian beam to a Laguerre–Gaussian beam and vice versa are analyzed experimentally. The converter is an astigmatic Fourier transformer consisting of a system of two cylindrical lenses with perpendicular principal planes lying between two spherical lenses. It is shown that this device is less sensitive to the mating of the astigmatic elements. © 1998 American Institute of Physics. [S1063-7850(98)01109-4]

The capacity of Laguerre–Gaussian beams to transport angular momentum of an electromagnetic wave has found wide application in devices for trapping, transporting,^{1,2} and “torquing” particles³ with dimensions of 1–20 μm . Ordinarily the electromagnetic angular momentum is associated with both the polarization⁴ and orbital properties of the electromagnetic wave. It is assumed that these orbital characteristics of the wave are due to a topological charge l which characterizes a special state of the electromagnetic field: an optical vortex⁶ or a wave with a purely screw dislocation.

Laser light sources can generate two types of paraxial coherent beams: Hermite–Gaussian (HG_{mn}) and azimuthally symmetric Laguerre–Gaussian (LG_{lg}) beams. Linearly polarized LG_{lg} beams are carriers of purely screw dislocations (optical vortices) and, hence, also transport angular momentum. Linearly polarized HG_{mn} beams have a degenerate edge dislocation of the wave front and do not transport angular momentum.⁷ For in-resonator selection of these beams one must use special diaphragms and absorbers, measures which are not always convenient in experimental practice.⁸ The use of holographic filters for forming optical vortices with the required magnitude and sign of the topological charge⁹ has opened up broad possibilities for the practical use of

Laguerre–Gaussian beams. However, the majority of the holograms used in practice for such purposes have a low diffraction efficiency.

Relatively recently Beijersbergen et al.¹⁰ proposed and developed an original means of converting Hermite–Gaussian beams to Laguerre–Gaussian beams and vice versa. The conversion of beams between different symmetry groups is done by means of two astigmatic cylindrical lenses with coincident (parallel) principal planes. The conversion of the beams occurs on account of the difference of the Gouy phases acquired by the beams in the space between the cylindrical lenses. The distance between lenses is chosen such that the phase difference at the exit from the lens at the time when the wave fronts overlap will be $\pi/2$ or π . A phase difference of $\pi/2$ corresponds to conversion of a LG_{lg} beam to an HG_{ml} beam and vice versa. The π conversion involves the transformation of a positive topological charge ($l > 1$) to a negative charge ($l < 1$) and vice versa. Such conversions are possible only when the astigmatic lenses are precisely phase matched.

In the present paper we analyze experimentally a less demanding method of conversion of beams of different symmetry groups, based on Fourier transformations in a system

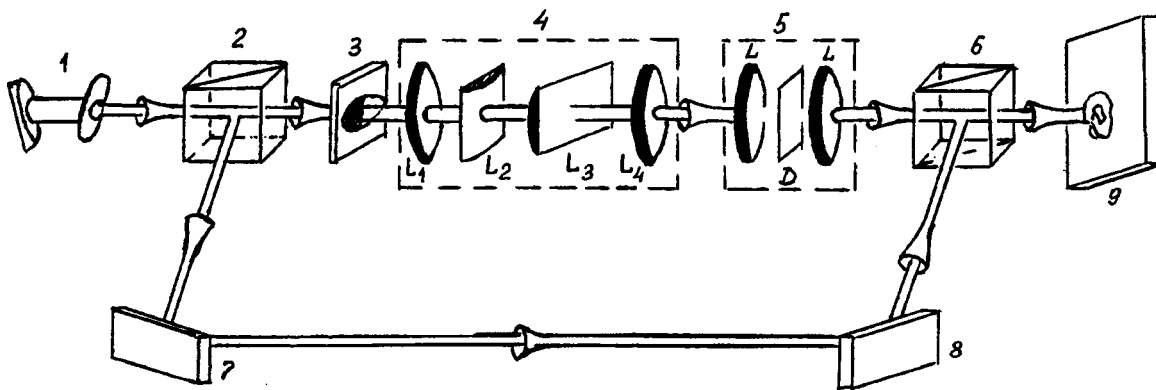


FIG. 1. Diagram of the experimental apparatus: 1 — He–Ne laser, 2,6 — beam splitters, 3 — phase transparency (a composite half-wave ($\lambda/2$) phase plate), 4 — phase converter (L_1 and L_4 are spherical lenses, L_2 and L_3 are cylindrical lenses), 5 — Fourier filter (two lenses L and a diaphragm D), 7,8 — mirrors, 9 — screen.

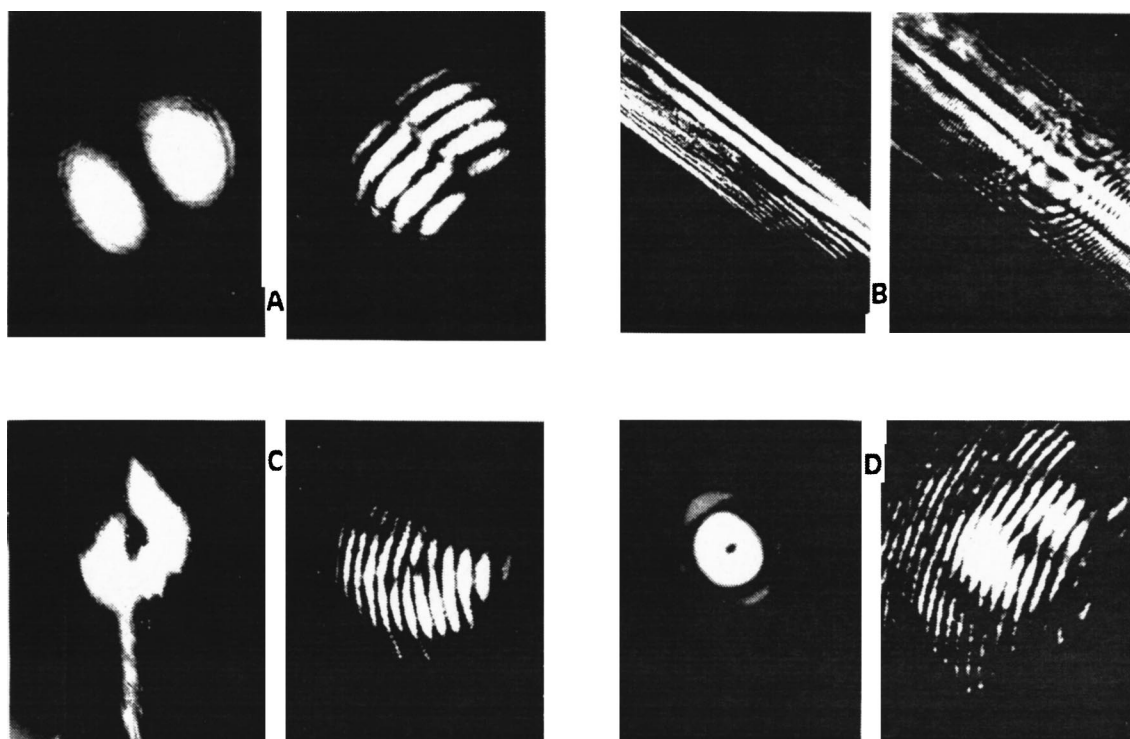


FIG. 2. Photographs of the beam shape: A — an Hermite–Gaussian beam with a degenerate edge dislocation; B — a deformed Gaussian beam with a degenerate edge dislocation; C — two aberrations of the coma type, a purely screw dislocation; D — a Laguerre–Gaussian beam with a purely screw dislocation.

of spherical and cylindrical lenses. The essence of the method is to use two cylindrical lenses with plane principal planes lying between two spherical lenses. A diagram of the experimental layout is shown in Fig. 1. Radiation from a He–Ne laser in the form of a fundamental Gaussian beam at wavelength $\lambda = 0.6328 \mu\text{m}$ and with a power $P = 1 \text{ mW}$ is used to excite a Mach–Zehnder interferometer. A mode converter is mounted in the object arm of the interferometer. At the entrance of the mode converter is a fundamental Gaussian beam that has been converted to a Laguerre–Gaussian beam LG_{lg} by a phase transparency. The phase transparency used is a composite half-wave ($\lambda/2$) plate, which permits introducing a phase difference of π between the wave fronts on only half of the transverse cross section of the beam. The total loss in the transparency amounts to 15–20%. The laser beam is transformed further by the phase converter, which consists of two cylindrical lenses (L_2, L_3) placed between two spherical lenses (L_1, L_4). The symmetry planes of the cylindrical lenses are perpendicular to each other (Fig. 1). This geometry of the converter substantially alters its working principle from that of the analogous device investigated in Ref. 10. When the symmetry axis of the phase transparency is oriented at an angle of 45° and, if the relations among the lengths between all four lenses are approximately satisfied, an Hermite–Gaussian beam is efficiently converted to a Laguerre–Gaussian beam. To cut off the higher-order harmonics a Fourier filter is used, consisting of two centered lenses and a diaphragm. Figure 2 shows photographs of the shape of the beam in the process of its sequential conversion in the individual units of the converter. Shown next to each

photograph of the beam is its interferogram, which characterizes the type of dislocation of the wave front. It is seen that the Hermite–Gaussian beam with a degenerate edge dislocation (Fig. 2a) becomes, after passing through the spherical lens L_1 and the two cylindrical lenses L_2 and L_3 , a highly deformed astigmatic Gaussian beam with a degenerate edge dislocation (Fig. 2b). However, after passing through the second spherical lens L_4 the beam starts to collapse into a composite of two aberrations of the coma type.¹¹ Then the deformed beam is characterized by an almost purely screw dislocation (Fig. 2c). The Fourier filter suppresses the higher harmonics, resulting in a symmetric Laguerre–Gaussian beam with a purely screw dislocation (Fig. 2d).

The losses in the lens converter and Fourier filter amount to 8–10%, so that the total energy loss came to 25–30%.

It was found that changing the orientation of the symmetry axis of the phase transparency at the entrance to the converter from $+45^\circ$ to -45° corresponds to reversing the sign of the topological charge of the beam.

¹K. T. Gahagan and G. A. Swartzlander Jr., *Opt. Lett.* **21**, 827 (1996).

²H. He, M. E. J. Friese, N. R. Heckenberg, and H. Rubinsztein-Dunlop, *Phys. Rev. Lett.* **75**, 826 (1995).

³N. B. Simpson, K. Dholakia, L. Allen, and M. J. Padgett, *Opt. Lett.* **22**, 52 (1997).

⁴R. A. Beth, *Phys. Rev.* **50**, 115 (1936).

⁵S. J. Van Enk and G. Nienhuis, *Opt. Commun.* **94**, 147 (1992).

⁶J. F. Nye and M. V. Berry, *Proc. R. Soc. London, Ser. A* **336**, 165 (1974).

⁷L. Allen, M. W. Beijersbergen, R. J. C. Spreeuw, and J. P. Woerdman, *Opt. Rev.* **45**, 45 (1992).

⁸M. Harris, C. A. Hill, and J. M. Vaughan, *Opt. Commun.* **106**, 161 (1994).

⁹J. V. Basistiy, I. V. Bazhenov, and Yu. M. S. Soskin, *Opt. Commun.* **103**, 422 (1993).

¹⁰M. W. Beijersbergen, L. Allen, H. E. L. O. van der Veen, and J. P. Woerdman, *Opt. Commun.* **96**, 123 (1993).

¹¹M. Born and E. Wolf, *Principles of Optics*, 4th ed., Pergamon Press, Oxford (1969); Nauka, Moscow (1970), p. 856.

Translated by Steve Torstveit

Features of the microwave breakdown of a high- T_c superconducting film at defects

N. A. Buznikov and A. A. Pukhov

*Joint Institute of High Temperatures; Scientific-Research Center of Applied Problems of Electrodynamics,
Russian Academy of Sciences, Moscow*

(Submitted July 9, 1997; resubmitted February 3, 1998)

Pis'ma Zh. Tekh. Fiz. **24**, 74–80 (September 12, 1998)

The influence of nonsuperconducting defects on the power density for microwave breakdown of a high- T_c superconducting film is investigated theoretically. It is found that the scenario of the destruction of superconductivity depends substantially on the shape of the defect and on the ratio of the absorption coefficients of the defect and film. It is shown that the breakdown power density at a defect may be higher than or equal to the threshold power density for microwave breakdown of a homogeneous film. © 1998 American Institute of Physics.
[S1063-7850(98)01209-9]

The microwave breakdown of high- T_c superconducting (HTSC) films has been observed in a number of studies.^{1–5} The thermal mechanism of breakdown involves a sharp increase in the absorption coefficient κ of the film when the critical temperature T_c is exceeded.⁶ It has been shown⁷ that the presence of normal (nonsuperconducting) defects in a HTSC film has a substantial effect on the breakdown power density P_c of the film. In this case the destruction of superconductivity may be due to the onset of a local temperature domain at the defect. In this paper we investigate the influence of the shape of the defect and its absorption coefficient on the scenario of the destruction of superconductivity and on the value of the power density at which microwave breakdown occurs.

Consider a HTSC film of thickness D_f on an insulating substrate of thickness $D_s \gg D_f$, the back side of which is held at a temperature T_0 . Incident microwave radiation of power density P is partially absorbed in the film, which has a normal defect of arbitrary shape. The microwave absorption coefficient of the defect, $\kappa = \kappa_d$, does not depend on the temperature T , while that of the remaining film, $\kappa = \kappa_f$, has a temperature dependence that can be written⁸ as $\kappa_f = \kappa_n \eta(T - T_c)$, where $\kappa_n = 4(\sigma D_f Z_0)^{-1} / [2(\sigma D_f Z_0)^{-1} + 1]^2$ is the absorption coefficient and σ the conductivity of the film in the normal state, $Z_0 = 377 \Omega$ is the wave impedance of the vacuum, and $\eta(x)$ is the Heaviside step function.

The absorption of microwave radiation by the defect causes its temperature to increase. The diffusion of heat causes heating of the rest of the film and the substrate, and a region of the film adjacent to the defect can undergo a transition to the normal state and become a source of additional microwave absorption. As a result, a steady-state temperature distribution arises in the film and substrate, corresponding to a temperature domain localized at the defect.⁷ Here the temperature distribution in the substrate is described by the three-dimensional steady-state heat conduction equation

$$\nabla \cdot (k_s \nabla T) = 0 \tag{1}$$

with the boundary conditions⁹

$$k_s \frac{\partial T}{\partial n} = -\kappa P, \quad T = T_0 \tag{2}$$

at the boundary of the film and substrate and on the back side of the substrate, respectively. Here k_s is the thermal conductivity of the substrate, and n is the normal to the film, directed into the substrate. The problem (1), (2) can be solved by separation of variables^{9,10} in the limiting cases of a linear defect and a circular defect.

Let us first consider a linear defect of half width D_d . Neglecting for simplicity the temperature dependence of k_s , we obtain for the half width D of the domain

$$\sum_{k=0}^{\infty} \lambda_k^{-2} \exp(-2\lambda_k D / D_s) - 2(\gamma - 1) \sum_{k=0}^{\infty} \lambda_k^{-2} \times \sinh(\lambda_k D_d / D_s) \exp(-\lambda_k D / D_s) = (P - P_p) / 2P. \tag{3}$$

Here $\lambda_k = \pi(2k + 1)/2$, $\gamma = \kappa_d / \kappa_n$ is the ratio of the absorption coefficient of the defect to that of the film in the normal state, and $P_p = 2k_s(T_c - T_0) / \kappa_n D_s$ is the threshold power density for breakdown of a homogeneous film.⁸ For $P < P_p$ breakdown is fundamentally impossible,⁸ and for $P > P_p$ breakdown develops if a normal phase region of sufficiently large size arises in the film.^{9,10} Figure 1 shows the curves of $D(P)$ for various values of D_d in the cases $\gamma < 1$ (dashed curves) and $\gamma > 1$ (solid curves).

For $\gamma > 1$ a temperature domain localized at the defect arises when the incident power density P exceeds a threshold value P_t , which is determined from the condition $D(P_t) = D_d$. For a sufficiently large D_d , the half width of the domain increases as P is increased (curves 1 and 2 in Fig. 1), and microwave breakdown occurs at $P = P_p$, when the domain occupies the entire film ($D \rightarrow \infty$). At smaller values of D_d the domain vanishes if the breakdown power density has a value $P_c > P_p$ (curve 3 in Fig. 1). In this case the transition of the film to the normal state occurs through the propagation along the film of a normal-phase region arising at the defect.^{8,10} For $\gamma < 1$ a domain does not arise in the film (curves 4–6 in Fig. 1), and breakdown occurs at a power

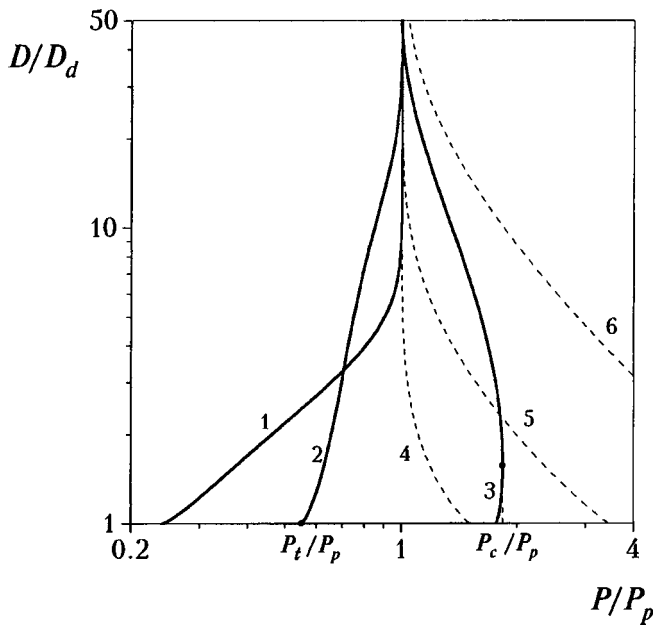


FIG. 1. Linear defect. Curves of the half width D versus the microwave power density P . The solid curves are for $\gamma=5$, the dashed curves for $\gamma=0.8$. 1,4 — $D_d/D_s=0.5$; 2,5 — $D_d/D_s=0.1$; 3,6 — $D_d/D_s=0.02$.

density P_c determined from the condition $D(P_c)=D_d$. In this case P_c is always higher than P_p , the threshold power density for breakdown of a homogeneous film. For a defect with a small half width $D_d \ll D_s$, the power density P_c is described approximately by the relations

$$P_c/P_p = (\pi/4)[\gamma \ln(D_d/D_s)|D_d/D_s|]^{-1}, \quad \gamma < 1,$$

$$P_c/P_p = (\pi/8)[(\gamma-1)|\ln\{(\gamma-1)D_d/D_s\}|D_d/D_s]^{-1}, \quad \gamma > 1. \quad (4)$$

Let us now consider a circular defect of radius R_d . From Eqs. (1) and (2) we get the following equation for the domain radius R :

$$(R/D_s) \sum_{k=0}^{\infty} \lambda_k^{-1} I_1(\lambda_k R/D_s) K_0(\lambda_k R/D_s) + (R_d/D_s)(\gamma-1) \times \sum_{k=0}^{\infty} \lambda_k^{-1} I_1(\lambda_k R_d/D_s) K_0(\lambda_k R/D_s) = P_p/4P, \quad (5)$$

where $I_1(x)$ and $K_0(x)$ are modified Bessel functions. We note that a dependence analogous to Eq. (5) was obtained in Ref. 7. Figure 2 shows the curves of $R(P)$ for various values of D_d in the cases $\gamma < 1$ (dashed curves) and $\gamma > 1$ (solid curves).

It is seen from Fig. 2 that for $\gamma < 1$ the function $R(P)$ is qualitatively similar to the function $D(P)$ for a linear defect, and microwave breakdown occurs without the formation of a temperature domain in the film (curves 4–6 in Fig. 2). For $\gamma > 1$ a domain forms in the film, and its radius increases monotonically with increasing P all the way up to the threshold power density P_c (curves 1–3 in Fig. 2). We note that in the case of a circular defect the breakdown power density P_c is always greater than P_p , the threshold power density for

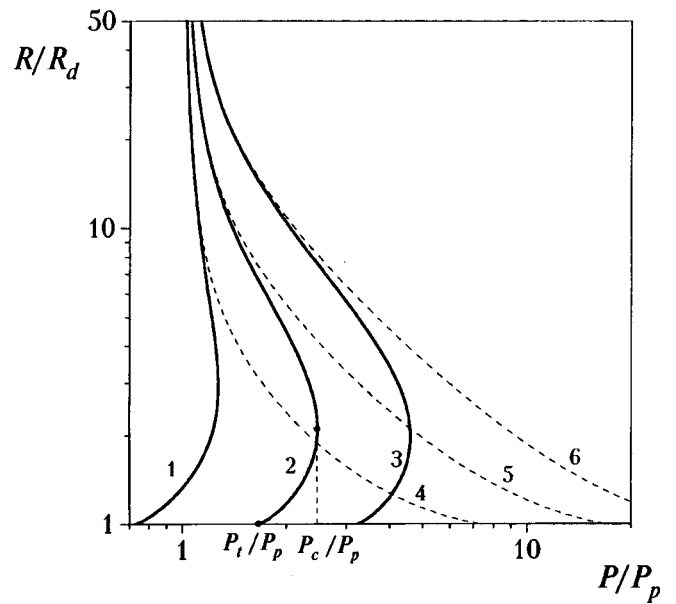


FIG. 2. Circular defect. Curves of the domain radius R versus the microwave power density P . The solid curves are for $\gamma=5$, the dashed curves for $\gamma=0.5$. 1,4 — $R_d/D_s=0.25$; 2,5 — $R_d/D_s=0.1$; 3,6 — $R_d/D_s=0.05$.

breakdown of a homogeneous film. For a defect of small radius $R_d \ll D_s$ the breakdown power density P_c is described approximately by the relations

$$P_c/P_p = (\pi/4)(\gamma R_d/D_s)^{-1}, \quad \gamma < 1,$$

$$P_c/P_p = (\sqrt{\pi}/4)(\sqrt{\gamma-1} R_d/D_s)^{-1}, \quad \gamma > 1. \quad (6)$$

Thus the scenario of microwave breakdown of a HTSC film with a normal defect depends on both the shape of the defect and the ratio γ of the absorption coefficients of the defect and film. For $\gamma > 1$ breakdown is preceded by an intermediate stage of formation of a temperature domain localized at the defect, while for $\gamma < 1$ breakdown occurs without the formation of a domain. The breakdown power density P_c depends substantially on the shape of the defect; for a linear defect P_c may be higher than or equal to the threshold power density P_p for breakdown of a homogeneous film, while for a circular defect P_c is always higher than P_p . For defects of small size $D_d \ll D_s$ or $R_d \ll D_s$, the value of P_c can be substantially greater than P_p (cf. Eqs. (4) and (6)).

In conclusion we note that the absorption model used here is applicable in the high-frequency limit, when the quasisteady flow of microwave current around the defect can be neglected. This condition is met if the characteristic time $\mu_0 \sigma_f R_d^2$ for expulsion of current from the defect is large compared to the inverse frequency of the microwave radiation f^{-1} : $f \mu_0 \sigma_f R_d^2 \gg 1$ (here $\sigma_f = \sigma B_{c2}/B$ is the conductivity of the film in the regime of viscous flow of the magnetic flux, B_{c2} is the upper critical field, and B is the surface microwave field). For typical parameters of Y–Ba–Cu–O films, $\sigma \approx 2 \times 10^6$ S/m and $B_{c2} \approx 50$ T, for the breakdown fields observed in experiment, $B \approx 0.01$ T (Refs. 1–4), and for $R_d \approx 1 \mu\text{m}$ (Ref. 5), we find that the model used is applicable for $f \gg 10^8$ Hz.

The authors are grateful to A. A. Zharov and A. N. Reznik for helpful discussions of the results and for making a copy of Ref. 7 available prior to publication.

This study was supported by the Government Science and Technology Project “Topical Problems in Condensed-Matter Physics” (Project No. 96083) and the Russian Fund for Fundamental Research (Project No. 96-02-18949).

¹R. W. Ralston, *Supercond. Sci. Technol.* **4**, 386 (1991).

²W. Diete, B. Aschermann, H. Chaloupka *et al.*, *Applied Superconductivity (Proc. EUCAS'95)*, Institute of Physics Press, Bristol, UK (1995), Vol. 2, pp. 1107–1110.

³N. Klein, N. Tellmann, U. Dähne *et al.*, *IEEE Trans. Appl. Supercond.* **AS-5**, 2663 (1995).

⁴G. Hampel, P. Kolodner, P. L. Gammel *et al.*, *Appl. Phys. Lett.* **69**, 571 (1996).

⁵M. Hein, W. Diete, M. Getta *et al.*, *IEEE Trans. Appl. Supercond.* **7**, 1264 (1997).

⁶A. A. Zharov, A. L. Korotkov, and A. N. Reznik, *Sverkhprovodimost' (KIAE)* **5**, 419 (1992) [*Superconductivity* **5**, 413 (1992)].

⁷A. A. Zharov and A. N. Reznik, *Zh. Tekh. Fiz.* **68**(1), 126 (1998) [*Tech. Phys.* **43**, 117 (1998)].

⁸A. A. Pukhov, *Pis'ma Zh. Tekh. Fiz.* **22**(12), 55 (1996) [*Tech. Phys. Lett.* **22**, 504 (1996)].

⁹N. A. Buznikov and A. A. Pukhov, *Pis'ma Zh. Tekh. Fiz.* **22**(20), 51 (1996) [*Tech. Phys. Lett.* **22**(10), 843 (1996)].

¹⁰N. A. Buznikov and A. A. Pukhov, *Supercond. Sci. Technol.* **10**, 318 (1997).

Translated by Steve Torstveit

Superdeep penetration efficiency

S. K. Andilevko, S. M. Usherenko, and V. A. Shilkin

Scientific-Research Institute of Pulsed Processes, Belorussian Government-Industry Powder Metallurgy Concern, Minsk, Belorussia

(Submitted January 29, 1998)

Pis'ma Zh. Tekh. Fiz. **24**, 81-84 (September 12, 1998)

The efficiency of an explosive accelerator is analyzed. The efficiency of the stream of particles in penetrating into a target to ultralarge depths is determined. © 1998 American Institute of Physics. [S1063-7850(98)01309-3]

In analyzing the results of experiments on superdeep penetration,¹⁻⁵ an important question is the amount of matter inserted into the target and its distribution in the target material. There are notable differences in the data¹⁻³ on the amount of inserted matter for different materials (sometimes by several orders of magnitude). Attempts to shed light on this question by indirect methods of evaluating the amount of inserted matter, e.g., based on estimates of the density of the channel zones in transverse cross sections of the target material, have not met with much success.^{2,4,5} Here the estimates also disagree, ranging from hundreds² of microparticles per square millimeter to thousands⁴ and tens of thousands⁵ per square millimeter. This circumstance necessitates carrying out a general analysis of the efficacy of an explosive accelerator^{7,8} for determining the mean amount of matter (or its concentration) inserted into a target under conditions of superdeep penetration (SDP).

From the results obtained in previous modeling of the process⁶⁻⁸ one can calculate the work required for the SDP of a single particle as the total energy expended on overcoming the total resistance of the target in the transient and steady-state parts of the particle motion.^{4,6,8} It follows from Ref. 4 and 6-8 that the energy expended by a nondeformable particle in the transient part of the motion can be neglected in comparison with that expended in the steady-state part of the motion. In that case, if dx is a small distance traversed by the particle in the target, U_c is the velocity of the steady-state motion of the particle,^{4,6,8} and ρ is the density of the target, the work expended on overcoming the segment dx can be calculated from the formula

$$dA = \rho \frac{U_c^2}{2} S_p dx, \quad (1)$$

where S_p is the midsectional area of the particle. Since the velocity of the steady-state motion at a constant pressure is constant,⁶⁻⁸ a particle penetrating to a depth H will expend an energy

$$e = \int_0^e dA = \int_0^H \rho \frac{U_c^2}{2} S_p dx = \rho \frac{U_c^2}{2} S_p H. \quad (2)$$

The average penetration depth H can be established from the variation of the mass concentration of inserted material with depth in the target, $c_m(h)$:

$$H = \frac{1}{2c_m} \int_0^l c_m(h) dh, \quad (3)$$

where L and c_m are the length of the target and the average concentration of inserted material, respectively. However, for determining the integral parameters of the process it is entirely acceptable to use a uniform concentration distribution ($c_m(h) = c_m = \text{const}$), in which case Eq. (3) gives a value $H = L/2$.

It follows from Ref. 4 and 6-8 that the sole source of energy for the UPD is the kinetic energy of the stream of particles formed by the explosive accelerator.^{6,8} If we denote by U_A and m_p the average velocity of the particle stream and the mass of an individual particle, respectively, the energy of each particle of the stream will be $e_p = m_p(U_A^2/2)$, from which we can determine the number of particles of the stream whose energy must be expended on the penetration of one particle to ultralarge depths:

$$N_\varepsilon = \frac{e}{e_p} = \frac{\rho S_p H}{m_p} \left(\frac{U_c}{U_A} \right)^2 \quad (4)$$

or, for a spherical particle of density ρ_p and radius r_p ,

$$N_\varepsilon = \frac{\rho \pi r_p^2 H}{4 \rho_p \frac{4}{3} \pi r_p^3} \left(\frac{U_c}{U_A} \right)^2 = \frac{3}{4} \frac{\rho}{\rho_p} \frac{H}{r_p} \left(\frac{U_c}{U_A} \right)^2. \quad (5)$$

The inverse quantity $\varepsilon = 1/N_\varepsilon$ is the efficiency of the stream. According to the available experimental and computational data¹⁻⁸ one has $U_c \approx 600$ m/s, $U_A \approx 1500$ m/s, $H = L/2 \approx 10^{-1}$ m, $r_p = 10^{-6}$ m, $\rho/\rho_p \approx 0.5-8$, and $N_\varepsilon \geq 10^4$. Consequently, for the efficiency of the stream we get a value $\varepsilon \leq 10^{-4}$ (or, equivalently, 0.01%), as was assumed in Ref. 6 and 8.

Knowing the efficiency of the stream under conditions of SDP, one can easily calculate the average mass content of powder in a target which is actually achievable in an experiment. If M_L is the mass of a powder charge, then the total mass of the inserted powder is $m = \varepsilon M_L$, and the average mass content in the target for a spherical particle is

$$c_m = \frac{m}{M_T} = \varepsilon \frac{M_L}{M_T} = \frac{4}{3} \frac{\rho_p}{\rho} \frac{r_p}{H} \left(\frac{U_A}{U_c} \right)^2 \frac{M_L}{M_T}, \quad (6)$$

where M_T is the mass of the target. Under standard experimental conditions¹⁻⁵ one has $M_L \approx 0.1$ kg and $M_T \approx 0.25$ kg, and so $c_m \leq 0.3 \times 10^{-4}$ (0.003%). Considering the various losses involved in achieving SDP in real experiments, one would expect this value to be lower still, so that formula (6) can be regarded as an estimate of the maximum average

mass concentration of an inserted substance that one could expect in an experiment. It should also be taken into account that the real distribution of the concentration over depth in the target is highly nonuniform and has a great many local extrema. Furthermore, penetration all the way through the target may occur.

From the foregoing analysis one can estimate the concentration levels of a substance inserted into a metallic target under conditions of one-shot loading by the superdeep penetration technique.

¹S. K. Andilevko, O. V. Roman, V. A. Shilkin, and S. M. Usherenko, *J. Phys.* IV **4**, 802 (1994).

²S. M. Usherenko, *Conditions for Superdeep Penetration and the Development of a Process for the Hardening of Tool Steels by a High-Velocity Stream of Powdered Materials* [in Russian], Candidate's Dissertation, Belorussian Polytechnical Institute, Minsk (1983), 256 pp.

³S. K. Andilevko, V. G. Serov, V. A. Shilkin, and S. M. Usherenko, in *High-Energy Processing of Materials* [in Russian], edited by V. V. Sobolev, Dnepropetrovsk (1997), pp. 8–14.

⁴S. K. Andilevko, *Superdeep Mass Transport of Discrete Microparticles in Metal Obstacles under Loading by a Stream of Powder* [in Russian], Candidate's Dissertation, Institute of Heat and Mass Transfer, Minsk (1991), 106 pp.

⁵V. A. Shilkin, *Structure and Properties of the Heat-Treated Steel R6M5 Hardened by a High-Velocity Stream of Powdered Materials* [in Russian], Candidate's Dissertation, Belorussian Polytechnical Institute, Minsk (1986), 172 pp.

⁶S. K. Andilevko, *J. Phys.* IV **7**, 729 (1997).

⁷L. V. Al'tshuler, S. K. Andilevko, G. S. Romanov, and S. M. Usherenko, *Pis'ma Zh. Tekh. Fiz.* **15**, 55 (1989) [*Sov. Tech. Phys. Lett.* **15**, 186 (1989)].

⁸S. K. Andilevko, V. A. Shilkin, S. M. Usherenko, and G. S. Romanov, *Int. J. Heat Mass Transf.* **36**, 1113 (1993).

Translated by Steve Torstveit

The Smoluchowski problem in polyatomic gases

A. V. Latyshev and A. A. Yushmanov

Moscow Pedagogical University

(Submitted March 10, 1998)

Pis'ma Zh. Tekh. Fiz. **24**, 85–89 (September 12, 1998)

A model kinetic equation is constructed which describes the behavior of molecular (polyatomic) gases in which the vibrational degrees of freedom are “frozen” and the rotational degrees of freedom are treated quasiclassically. An analytical solution is obtained for the Smoluchowski problem of the temperature jump and weak evaporation above a planar surface in a half space. Numerical calculations are carried out. © 1998 American Institute of Physics. [S1063-7850(98)01409-8]

The Smoluchowski problem has attracted steady attention for a long time now. This problem is of interest because of its theoretical importance and numerous practical applications. For a simple gas this problem has been treated by analytical methods¹ and by approximate and numerical methods for the total Boltzmann equation.^{2,3}

The cited papers have dealt with the case of a monatomic gas. At the same time, the majority of gases are polyatomic (molecular). It is therefore indisputably of interest to investigate the case of molecular gases. Kinetic processes in molecular gases are more complicated than in a monatomic (simple) gas.⁴ For this reason, model collision integrals play a more important role. An important circumstance is that for many molecular gases there exists a wide range of temperatures (from tens to thousands of kelvins) in which, on the one hand, the vibrational degrees of freedom or “frozen,” i.e., do not contribute to the thermodynamic and kinetic properties of the gas, and, on the other hand, the rotational degrees of freedom can be treated quasiclassically.⁵ It is this study that we consider here.

Model collision integrals for this case have been considered in Refs. 6–8. A model collision integral for a diatomic gas was considered in Ref. 9, and the problem of the temperature jump was addressed. In the present paper we consider a generalization of the approach proposed in Ref. 9 to the case of polyatomic gases, i.e., gases whose molecules contain three or more atoms.

A model kinetic equation of the Bhatnagar–Gross–Krook (BGK) type for the steady-state case has the familiar form

$$\mathbf{v} \cdot \nabla f = \nu(f_{\text{eq}} - f). \tag{1}$$

Here \mathbf{v} is the velocity of the molecules, $f(\mathbf{r}, \mathbf{v})$ is the distribution function, and ν is the collision frequency of the molecules. The function f_{eq} is the equilibrium distribution function with averaged characteristics:

$$f_{\text{eq}} = n_{\text{eq}} \left(\frac{m}{2\pi kT_{\text{eq}}} \right)^{\frac{3}{2}} \exp \left[-\frac{m}{2kT_{\text{eq}}} (\mathbf{v} - \mathbf{u}_{\text{eq}})^2 \right],$$

where m is the mass of a molecule and k is Boltzmann's constant.

The quantities n_{eq} , T_{eq} , and \mathbf{u}_{eq} are calculated as moments of the distribution function f .

In the case when the internal degrees of freedom are quasiclassical, the model kinetic equations for polyatomic gases can be written in the form (1) with an equilibrium distribution function

$$f_{\text{eq}}^p = n_* \frac{(m^3 J_1 J_2 J_3)^{\frac{1}{2}}}{(2\pi kT_*)^3} \exp \left[-\frac{m}{2kT_*} (\mathbf{v} - \mathbf{u}_*)^2 - \frac{J_1 \omega_1^2 + J_2 \omega_2^2 + J_3 \omega_3^2}{2kT_*} \right].$$

Here J_1 , J_2 , and J_3 are the principal moments of inertia of the molecule, and $\omega = (\omega_1, \omega_2, \omega_3)$ is the angular velocity vector of its rotation. The quantities n_* , \mathbf{u}_* , and T_* are determined as the corresponding moments of the distribution function $f(\mathbf{r}, \mathbf{v}, \omega)$:

$$n_* = \int f d^3 v d^3 \omega, \quad \mathbf{u}_* = \frac{1}{n_*} \int \mathbf{v} f d^3 v d^3 \omega,$$

$$T_* = \frac{1}{3kn_*} \int \left[\frac{m}{2} (\mathbf{v} - \mathbf{u}_*)^2 + \frac{1}{2} (J_1 \omega_1^2 + J_2 \omega_2^2 + J_3 \omega_3^2) \right] \times f d^3 v d^3 \omega.$$

Below we will be interested in the case when the gradients of the thermodynamic quantities are small. We will also assume that the velocity of the gas is small in a reference frame tied to the interface. Then the distribution function can be written in the linearized form $f = f_0(1 + \varphi)$. Here

$$f_0 = n_s \frac{(m^3 J_1 J_2 J_3)^{1/2}}{(2\pi kT_s)^3} \exp \left[-\frac{mv^2}{2kT_s} - \frac{J_1 \omega_1^2 + J_2 \omega_2^2 + J_3 \omega_3^2}{2kT_s} \right],$$

T_s is the surface temperature, n_s is the density of the saturated vapor of the surface material at the surface temperature, and $|\varphi| \ll 1$.

In this case linearizing the model collision integral in (1) leads to the following kinetic equation:

$$(\mathbf{v} \cdot \nabla \varphi) + \nu \varphi = \left[\frac{\delta n}{n_s} \left(\frac{mv^2}{2kT_s} - \frac{J_1 \omega_1^2 + J_2 \omega_2^2 + J_3 \omega_3^2}{2kT_s} \right) + \frac{m}{kT_s} \mathbf{u}_* \cdot \mathbf{v} \right]. \tag{2}$$

Here

$$\delta n = n_* - n_0 = \int f_0 \varphi d^3 v d^3 \omega,$$

$$\mathbf{u}_* = \frac{1}{n} \int f_0 \varphi \mathbf{v} d^3 v d^3 \omega, \quad \delta T = T_* - T_s,$$

$$\frac{\delta T}{T_s} = -\frac{\delta n}{n_s} + \frac{2}{3knT_s} \int f_0 \varphi \left[\frac{mv^2}{2} + \frac{1}{2}(J_1 \omega_1^2 + J_2 \omega_2^2 + J_3 \omega_3^2) \right] d^3 v d^3 \omega.$$

We introduce a Cartesian coordinate system with its origin on the interface between the gas and condensed phase and its x axis perpendicular to the surface and directed into the gas. We suppose that in the gas far from the surface there is a temperature gradient perpendicular to the surface. Evaporation and condensation processes can occur at the surface, and there can be a mean-mass velocity of the gas in the direction toward or away from the the surface. Then $T = T_e + Ax$ for $x \rightarrow \infty$. Here $A = (dT/dx)_{x=\infty}$; the quantity $\Delta T = T_e - T_s$ is called the temperature jump. We denote the velocity of the gas from the surface as U .

The kinetic equation (2) can be written as follows in dimensionless variables:

$$\xi_x \frac{\partial \varphi}{\partial x} + \varphi(x, \xi, \omega) = \frac{4}{\pi^2} \int e^{-\xi^2 - \omega^2} k(\xi, \omega; \xi', \omega') \times \varphi(x, \xi', \omega') \omega'^2 d^3 \xi' d^3 \omega'. \quad (3)$$

Here

$$k(\xi, \omega; \xi', \omega') = 1 + 2\xi\xi' + \frac{1}{3}(\xi^2 + \omega^2 - 3)(\xi'^2 + \omega'^2 - 3)$$

is the kernel of the equation.

We shall assume that the molecules are reflected from the wall in a purely diffuse manner, i.e., $f(0, \xi, \omega) = f_0$, if $\xi_x > 0$. For the function φ we then get

$$\varphi(0, \xi, \omega) = 0, \quad \text{if } \xi_x > 0. \quad (4)$$

Far from the wall the distribution function should go over to the Chapman–Enskog distribution, i.e.,

$$\varphi(0, \xi, \omega) = \varphi_{as}(x, \xi, \omega) + O(1), \quad \text{if } x \rightarrow \infty, \quad \xi_x < 0, \quad (5)$$

where

$$\varphi_{as} = \varepsilon_n + 2U\xi_x + \varepsilon_t(\xi^2 + \omega^2 - 3) + K(x - \xi_x)(\xi^2 + \omega^2 - 4), \quad K = A/T_s.$$

We expand the function φ in the two orthogonal directions, $e_1 = 1$ and $e_2 = \xi^2 + \omega^2 - 3$:

$$\varphi = h_1(x, \xi_x) + \gamma(\xi^2 + \omega^2 - 3)h_2(x, \xi_x), \quad \gamma^2 = \frac{1}{3}. \quad (6)$$

We introduce the column vector $h = [h_1 h_2]^t$. Then on the basis of Eq. (3) we obtain a system of equations which can be written in vector form as (we have set $\mu = \xi_x$):

$$\mu \frac{\partial h}{\partial x} + h(x, \mu) = \frac{1}{\sqrt{\pi}} \int_{-\infty}^{\infty} e^{\mu'^2} K_0(\mu, \mu') h(x, \mu') d\mu'. \quad (7)$$

Here the matrix function $K_0(\mu, \mu') = K(\mu') + 2\mu\mu' L(\mu')$ is the kernel of Eq. (7),

$$K(\mu) = \begin{vmatrix} 1 & \kappa(\mu) \\ \kappa(\mu) & \kappa^2(\mu) + 5/6 \end{vmatrix}, \quad L(\mu) = \begin{vmatrix} 1 & \kappa(\mu) \\ 0 & 0 \end{vmatrix},$$

$$\kappa(\mu) = \gamma \left(\mu^2 - \frac{1}{2} \right).$$

Using expansion (6), we can put the boundary conditions (4) and (5) in the form

$$h(0, \mu) = \begin{vmatrix} 0 \\ 0 \end{vmatrix}, \quad \mu > 0, \quad (8)$$

$$h(x, \mu) = h_{as}(x, \mu) + O(1), \quad x \rightarrow \infty, \quad \mu < 0, \quad (9)$$

where

$$h_{as}(x, \mu) = \begin{vmatrix} \varepsilon_n + 2U\mu - K(x - \mu) \\ \frac{1}{\gamma}(\varepsilon_t + K(x - \mu)) \end{vmatrix}.$$

We will skip over the solution of the problem (7)–(9), which is known from Refs. 1 and 9, and give the formulas for calculating the temperature jump and concentration jump in dimensional form:

$$\varepsilon_t = \delta_T l K + \gamma_U 2U, \quad \varepsilon_N = \delta_N + \gamma_N 2U,$$

where δ_t and δ_N are the coefficients of the temperature jump and concentration jump, and U is the dimensional evaporation velocity.

Numerical calculations show that $\delta_T = 1.87224$. We note that for a diatomic gas this quantity has a value of 2.05647 (Ref. 9), and for a simple gas, 2.2049 (Ref. 1). Thus the temperature jump decreases monotonically as the number of atoms in a molecule increases (at a constant Prandtl number).

The proposed method of analytical solution can be applied to a wide class of boundary-value problems for polyatomic gases.

This study was supported by a grant from the Russian Fund for Fundamental Research (Project Code 97-01-00333).

¹A. V. Latyshev, *Prikl. Mat. Mekh.* **54**, 581 (1990).
²E. P. Gross, E. A. Jackson, and S. Ziering, *Phys. Fluids* **2**, 432 (1959).
³Y. Onishi and Y. Sone, *J. Phys. Soc. Jpn.* **44**, 1981 (1978).
⁴V. M. Zhdanov and M. Ya. Alievskii, *Transport and Relaxation Processes in Molecular Gases* [in Russian], Nauka, Moscow (1989), 336 pp.
⁵L. D. Landau and E. M. Lifshitz, *Statistical Physics*, 2nd ed., Pergamon Press, Oxford (1969) [Russian original, Nauka, Moscow (1964), 567 pp.].
⁶V. A. Rykov, *Izv. Akad. Nauk SSSR, Mekh. Zhidk. Gaza* **XX**, No. 6, 105 (1975).
⁷I. N. Larina and V. A. Rykov, in *Numerical Methods in the Dynamics of Dilute Gases*, Vol. 4 [in Russian], Computational Center of the Academy of Sciences of the USSR, Moscow (1978), pp. 52–68.
⁸I. N. Larina and V. A. Rykov, *Izv. Akad. Nauk SSSR, Mekh. Zhidk. Gaza* **XX**, No. 5, 141 (1986).
⁹A. V. Latyshev and A. A. Yushkanov, *Teor. Mat. Fiz.* **95**, 530 (1993).

Conducting properties and structure of nonstoichiometric orthorhombic phase of $\text{YBa}_2\text{Cu}_3\text{O}_{7-x}$ obtained by high-temperature vacuum annealing

I. Khidirov, V. T. Ém, N. N. Mukhtarova, and A. S. Rakhimov

Institute of Nuclear Physics, Academy of Sciences of the Republic of Uzbekistan, Tashkent
(Submitted March 6, 1997)

Pis'ma Zh. Tekh. Fiz. **24**, 90–95 (September 12, 1998)

Neutron and x-ray diffraction studies are carried out which show when the orthorhombic phase of $\text{YBa}_2\text{Cu}_3\text{O}_{7-x}$ ($x \approx 0.02$) is heat treated at temperatures of 430–550 K under tunnel high-vacuum pumping, a partial emission of oxygen from the O(1) positions (with coordinates 0;0;0.1578) and O(4) positions (with coordinates 0;1/2;0) occurs with no change in the symmetry or in the unit cell parameters. The temperature dependence of the electrical resistivity in the temperature interval 77–300 K shows a semiconducting character. © 1998 American Institute of Physics. [S1063-7850(98)01509-2]

The compound $\text{YBa}_2\text{Cu}_3\text{O}_{7-x}$ has a low value of the enthalpy of the oxidation reaction, a fact which indicates that the bonding of some of the oxygen in the crystal lattice is weak.¹ This suggests that the oxygen can be extracted from the $\text{YBa}_2\text{Cu}_3\text{O}_7$ lattice without a change in the orthorhombic symmetry not only by chemical means in a medium of H_2 at low temperatures, as was done in Ref. 2, but also by continuous high-vacuum pumping at comparatively low temperatures (430–550 K). In this paper we present results from a study of the conducting properties and structure of a high- T_c superconducting ceramic after such heat treatment.

The samples chosen for the study were polycrystalline $\text{YBa}_2\text{Cu}_3\text{O}_{6.98}$ prepared by ceramic technology. The transition temperature T_c was determined from the temperature dependence of the ratio $R(T)/R(300\text{ K})$; the resistance was measured by the four-contact method. X-ray diffraction measurements were made on powder samples on a DRON-3M x-ray diffractometer (CuK_α radiation), and the neutron diffraction measurements were made on a DN-500 neutron diffractometer mounted on the thermal port of the reactor at the Institute of Nuclear Physics of the Academy of Sciences of the Republic of Uzbekistan in Tashkent ($\lambda = 1.085 \text{ \AA}$).

The initial sample had an orthorhombic unit cell with the parameters $a = 3.837(2)$, $b = 3.886(5)$, and $c = 11.673(5) \text{ \AA}$; the temperature of the transition to the superconducting state was $T_c = 87 \text{ K}$ (Fig. 1). After the temperature dependence $R(T)$ was measured, the sample was loaded into a vacuum furnace and annealed at a temperature of 520 K for 24 h. The vacuum inside the furnace was maintained at a level of $2 \times 10^{-3} \text{ Pa}$ or better by continuous pumping.

After annealing the sample retained its orthorhombic structure without any noticeable changes in the lattice parameters. However, the temperature dependence of the resistivity in the interval 77–300 K acquired a semiconducting character (Fig. 1).³ Measurement of the magnetic susceptibility showed that the loss of superconducting properties occurred throughout the entire volume of the sample, and not only in a surface layer. Analogous results were obtained after vacuum annealing for 24 h at temperatures of 430, 470, 530, and 550 K. It should be noted that the loss of superconductivity after vacuum annealing at temperatures of 480–550 K with a half-hour hold had been observed previously⁴ from the temperature dependence of the magnetic susceptibility χ .

The character of the distribution of oxygen in the O(1)–O(5) positions of the unit cell of the annealed samples was determined by a neutron-diffraction analysis, which can give a more accurate determination of the oxygen concentration in the lattice than a chemical analysis can.^{5,6} An attempt to determine the oxygen content from the ratio of the intensities of certain reflections, as was proposed in Refs. 5 and 6, did not meet with success here, since the results of the analysis depended on the choice of reflection. This ambiguity can be accounted for by the fact that the methods proposed in Refs.

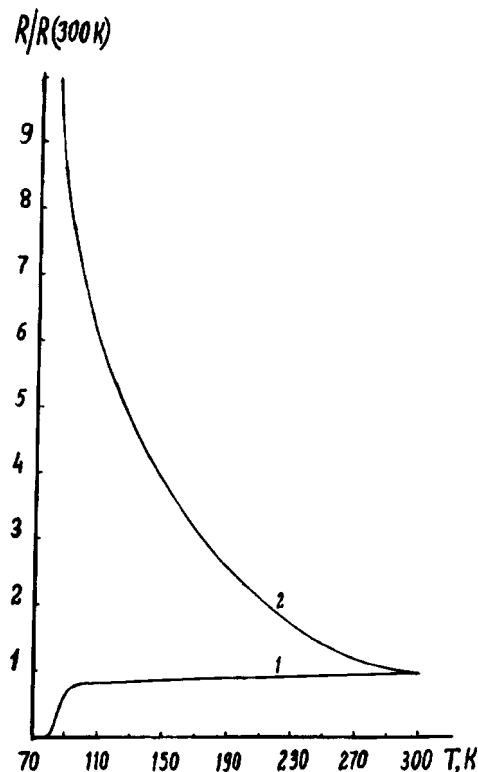


FIG. 1. $R(T)/R(300\text{ K})$: 1 — initial ceramic $\text{YBa}_2\text{Cu}_3\text{O}_{7-x}$; 2 — after annealing in vacuum at 520 K for 24 h.

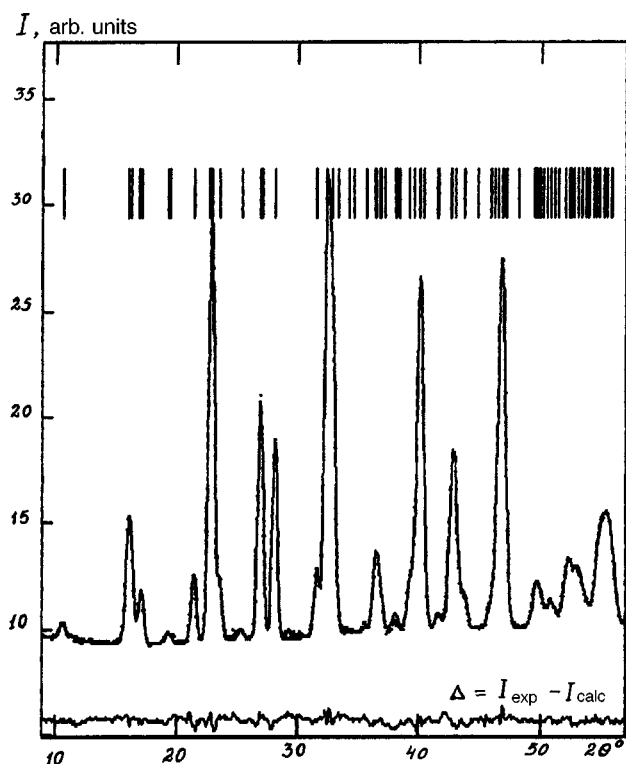


FIG. 2. Neutron diffraction curves of a $\text{YBa}_2\text{Cu}_3\text{O}_{6.67}$ sample obtained by vacuum annealing at $T = 520$ K. The points are experimentally observed, the solid curve is calculated; Δ is the difference (the observed minus the calculated).

5 and 6 are reliable only in the case when all the oxygen positions except O(4) and O(5) are occupied. We therefore used the Rietveld method⁷ to determine the oxygen concentration by a minimization of the uncertainty factors in the determination of the structure upon arbitrarily specified variations of the oxygen concentration in all the positions. The smallest values of the uncertainty factors were obtained under the assumption that the oxygen content after annealing had decreased to $x = 0.33 - 0.23$, values which correspond to compositions $\text{YBa}_2\text{Cu}_3\text{O}_{6.67-6.77}$ (see Fig. 2 and Table I). What occurs here is not a transition of oxygen from the O(4) positions (with coordinates $0; 1/2; 0$) to the O(5) position ($1/2; 0; 0$), as is observed at relatively high temperatures in an oxygen medium,⁸ but a decrease in the amount of oxygen in

TABLE I. Structural characteristics of $\text{YBa}_2\text{Cu}_3\text{O}_{6.77}$ obtained by low-temperature vacuum annealing.

Atom	x	y	z	Δz	$B, \text{\AA}^2$	$\Delta B, \text{\AA}^2$	n^*	Δn
Y	1/2	1/2	1/2	0.0000	1.01	0.22	1.00	0.00
Ba	1/2	1/2	0.1864	0.0006	0.61	0.18	2.00	0.00
Cu1	0	0	0	0.0000	0.91	0.21	1.00	0.00
Cu2	0	0	0.3560	0.0005	0.73	0.12	2.00	0.00
O1	0	0	0.1574	0.0008	0.53	0.12	1.87	0.04
O2	1/2	0	0.3737	0.0008	0.60	0.12	2.04	0.04
O3	0	1/2	0.3825	0.0010	0.68	0.12	2.06	0.05
O4	0	1/2	0	0.0000	1.72	0.50	0.80	0.03
O5	1/2	0	0	0.0000	0.00	0.00	0.00	0.00

$R_p = 1.80\%$, $R_{wp} = 2.25\%$, $R_{br} = 4.84\%$, $R_f = 3.67\%$

* n is the number of atoms in the positions, and B is the thermal factor.

the O(1) positions (with coordinates $0; 0; 0.1578$) and O(4) positions, with a complete lack of oxygen in the O(5) positions. This result can apparently be attributed to the lowered binding energy of the O(1) and O(4) atoms, as is attested to by the high values of the thermal factors determined for single crystals in Ref. 9. It should be noted that a substantial decrease of the occupation of the O(1) positions has been observed previously in the tetragonal phase after quenching from 1027 K,⁸ but here, because of the high temperature, there also occurs a disordering of the oxygen atoms over the O(4) and O(5) positions.

Thus in the low-temperature vacuum annealing of $\text{YBa}_2\text{Cu}_3\text{O}_{7-x}$ a portion of the oxygen is removed from the lattice, but because of the relatively low annealing temperature the kinetic processes of restructuring are sluggish, and the orthorhombic phase with nearly the original values of the lattice parameters is "frozen in." This agrees with the data of Ref. 2, according to which the restructuring of the orthorhombic phase is sluggish at temperatures below 600 K.

It can be supposed that that the observed change in the character of the conduction after vacuum annealing is related to the density of defects in the oxygen positions O(1), since it is the character of the occupation of these positions that distinguishes orthorhombic phases which are close in composition but obtained by different methods: high-temperature annealing in vacuum; at high temperature in an oxygen medium;¹⁰ and at low temperatures in a hydrogen medium.² Consequently, the electron-transport properties of the superconducting ceramic depend importantly on the degree of occupation of the O(1) as well as O(4) oxygen positions.

In summary, taking the compound $\text{YBa}_2\text{Cu}_3\text{O}_{7-x}$ as an example, we have shown that by continuous high-vacuum pumping at temperatures of 430–550 K one can extract oxygen from the lattice of the superconducting ceramic without altering the symmetry and lattice parameters, but the resulting compound $\text{YBa}_2\text{Cu}_3\text{O}_{6.67-6.77}$ has a semiconducting character of the temperature dependence of the resistivity in the temperature interval 77–300 K.

This study was financed by the Foundation for Support of Basic Research of the Academy of Sciences of the Republic of Uzbekistan.

¹P. K. Gallagher, Adv. Ceram. Mater. 2, 632 (1987).
²Yu. M. Baïkov, S. K. Filatov, V. V. Semin et al., Pis'ma Zh. Tekh. Fiz. 16(3), 76 (1990) [Sov. Tech. Phys. Lett. 16(2), 116 (1990)].
³I. Khidirov, A. S. Rakhimov, and V. T. Ém, IYAF RUZ. Preprint No. 3-9-527 [in Russian], Institute of Nuclear Physics, Republic of Uzbekistan, Tashkent (1991), 7 pp.
⁴A. G. Merzhanov, Yu. N. Barinov, I. P. Borovinskaya et al., Pis'ma Zh. Tekh. Fiz. 15(11), 1 (1989) [Sov. Tech. Phys. Lett. 15(6), 413 (1989)].
⁵V. E. Arkhipov and V. E. Naïsh, Sverkhprovodimost' (KIAE) 2, 71 (1989).
⁶I. S. Latergaus, V. T. Ém, and M. Yu. Tashmetov et al., IYAF AN RUZ. Preprint No. P-3-383 [in Russian], Institute of Nuclear Physics, Republic of Uzbekistan, Tashkent (1989), 16 pp.
⁷H. M. Rietveld, J. Appl. Crystallogr. 2, 65 (1969).
⁸V. A. Somenkov, V. P. Glazkov, A. S. Ivanov et al., JETP Lett. 46, 542 (1987).
⁹V. N. Molchanov, L. A. Muradyan, and V. I. Simonov, JETP Lett. 49, 257 (1989).
¹⁰I.É. Graboř and V. I. Putyaev, Zh. Vses. Khim. O-va. 34, 473 (1989).

Mechanism for the dependence of the photoemission threshold of a photocathode on its irradiance

Kh. N. Vezirov

Photoelectronics Research Institute, Baku, Azerbaijan

(Submitted April 15, 1997; resubmitted January 20, 1998)

Pis'ma Zh. Tekh. Fiz. **24**, 1–6 (September 26, 1998)

Secondary electron emission is shown to occur at the boundary of the working region of a photocathode when current flows through this region, causing a deviation from the known classical laws of photoemission. It is established that the sensitivity and photoemission threshold of the photocathode depend on the strength of the photocurrent flowing through it.

© 1998 American Institute of Physics. [S1063-7850(98)01609-7]

In studies of M-9 image converters¹ with silver–oxygen–cesium photocathodes it was observed that for some samples, the sensitivity and long-wavelength photoemission threshold of the photocathode regions adjacent to the baffle depend on the strength of the total current flowing through the photocathode.

In order to clarify the mechanism responsible for this effect, M-9 image converters were fabricated (Fig. 1) for which the diameters of the working regions of the photocathode and the luminescence screen were 3.5 and 5 cm respectively (for normal M-9 image converters these dimensions are 5 cm). The investigations were carried out as follows. A saturation voltage was created between the photocathode 1 and the screen 2 of the image converter and the spectral sensitivity characteristics of the photocathode section 3 adjacent to the baffle 4 (i.e., the section directly adjacent to the boundary of the working region of the photocathode) were recorded by systematically measuring the photocurrents generated as a result of exposure to monochromatic radiation 5 at wavelengths between 0.4 and 1.7 μm modulated, for example, at a frequency of 1000 Hz. The diameter of the light beam did not exceed 0.1 mm and the radiation was supplied from an MDR-2 monochromator. The power of the radiation 5 was then increased and the spectral sensitivity characteristic of the same section of photocathode was measured again. Several more measurements were then made with increasingly powerful radiation fluxes 5, i.e., higher photocurrents.

It can be seen from Fig. 2 that the sensitivity and long-wavelength photoemission threshold of a single point 3 on the photocathode depend on the power of the radiation flux incident at this point. At first glance, this clearly contradicts the classical photoemission laws, according to which the ratio of the change in the photocurrent to the change in the radiant flux incident on the photocathode is a constant known as the sensitivity: $S = dJ/d\Phi$.

It was also observed that in those image converters where a working (high) voltage was created between the photocathode and the anode (luminescence screen), and the central parts of the photocathode were irradiated and not the edge (i.e., the radiation 6 is incident on the photocathode and

not the radiation 5), the luminescence 7 from the center of the luminescence screen was also accompanied by an image of the boundary of the photocathode working region in the form of a luminous ring 8 at the edge of the screen. The brightness of this ring 8 depended on the strength of the total current through the photocathode, i.e., on the irradiance of the center of the photocathode.

Assuming that the emission from the luminescence screen only occurs under electron bombardment and that in the image converter each point on the surface of the luminescence screen corresponds to a single point on the surface of the photocathode, we conclude that when the central parts of the photocathode are irradiated, electrons are emitted from the sections 3 adjacent to the baffle and on reaching the peripheral sections of the screen, they cause it to luminesce in the form of a ring 8.

It was established in earlier investigations² that when a photocathode is fabricated by conventional technology, it has a gap at points adjacent to the baffle. Microscopic investigations showed that the width of this gap is of order a micron (between 0.2 and 2 μm). This leads to the establishment of an enhanced intermediate resistance R between the baffle and the photocathode. Direct measurements revealed that this resistance is of order 5 M Ω . In consequence, almost all the voltage formed in the photocathode film as a result of photoemission of electrons into vacuum, between the illuminated point on the photocathode and the baffle, is incident at the gap in the photocathode film since the resistance of this film is considerably lower (of order kilohms). Thus, regardless of whether photoemission occurs as a result of irradiation of some point on the photocathode, the flow of current through the photocathode film leads to the formation of an electric field in the gaps, whose strength E is given by

$$E = \frac{U}{L}, \quad (1)$$

where U is the potential difference between the edges (i.e., on different sides) of the gap (i.e., between the baffle and the edge of the photocathode). Calculations show that if the total current through the photocathode is 1 μA , the voltage U is approximately 5 V. Equation (1) gives a strength E of order

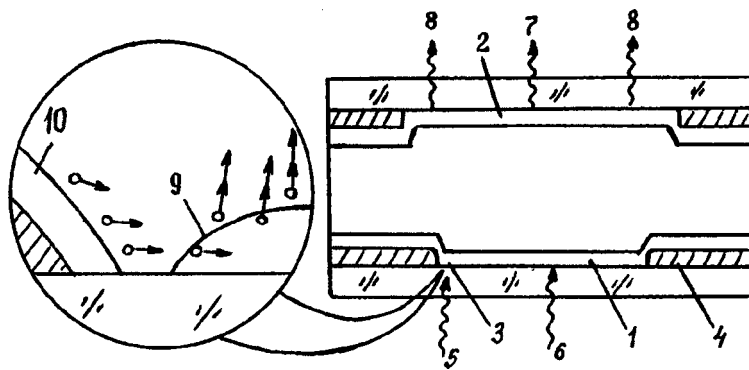


FIG. 1. Cross section of image converter. The primary electrons are denoted by points with a single arrow and the secondary electrons by points with two arrows.

5×10^4 V/cm. It is known³ that field emission from the photocathode can easily occur at these strengths. Thus, there is no doubt that when current flows through the photocathode, field emission occurs from the edge of the baffle and after entering the strong electric field in the gap and undergoing acceleration, the emitted electrons bombard the boundary of the working region of the photocathode.² This inevitably leads to secondary electron emission and regardless of the coefficient of secondary electron emission (which may be greater or less than 1), some of these secondary electrons escape into vacuum.

Some of the field-emission electrons may also be incident on sections 9 of the photocathode surface adjacent to the gap and bordering on vacuum, i.e., near point 3. This also gives rise to secondary electron emission from these sections 9 of the photocathode surface (for precisely these reasons, when the central sections of the photocathode were irradiated and not section 3 electrons were also emitted from section 3, and these electrons bombarded the edge of the luminescence screen, causing it to luminesce in the form of a ring). It is known^{4,5} that for photocathodes the coefficient of secondary electron emission for low primary electron energies increases with increasing energy (and therefore U , which is proportional to the current J). Thus, as the photocurrent strength (and therefore the current in the gap) increase as a result of increasing illumination (radiation power), the potential difference U and the secondary electron emission current will

also increase. This is why the brightness of the luminescence ring 8 at the edge of the screen also increases as a function of the illumination of the center of the photocathode.

It should also be borne in mind that the width L of the gap in the photocathode film is comparable with the wavelength of the recorded radiation (i.e., the wavelength of the radiation 5) incident on the boundary of the photocathode working region (i.e., near the gap). It can thus be reliably stated that diffraction must take place and some of the radiation flux 5 incident from the substrate at the edge of the photocathode working region, after being diffracted, will reach the photocathode region 10 situated in the gap at the edge of the baffle, thereby also causing photoemission from these sections 10. Under the influence of the electric field the work function of the photocathode section 10 decreases by $\Delta e\phi$, which is known⁶ to be given by

$$\Delta e\phi = 3.79 \times 10^{-4} \sqrt{E}. \quad (2)$$

As a result of the reduction in the work function of the section 10, the long-wavelength photoemission threshold of this section shifts toward longer wavelengths and this shift will be proportional to $\Delta e\phi$. By substituting the value of E obtained above (5×10^4 V/cm) into Eq. (2), we determine the predicted decrease in the work function $\Delta e\phi \approx 0.08$ eV. With this decrease in the work function the long-wavelength photoemission threshold should be shifted from $1.56 \mu\text{m}$ (Fig. 2) to $1.7 \mu\text{m}$. In practice the threshold was shifted to $1.65 \mu\text{m}$ (Fig. 2), which agrees fairly well with the theory and confirms the accuracy of the proposed hypothesis. If we take into account Eqs. (1) and (2) and also the fact that U is proportional to the photocurrent strength (more accurately the total current J passing through the photocathode) and the intermediate resistance R , it becomes clear that $\Delta e\phi = 3.79 \times 10^{-4} \sqrt{KJR/L}$, where K is a numerical coefficient of order 1.

To conclude, it can be assumed that photoelectron emission from regions of the photocathode adjacent to the baffle is also accompanied by secondary electron emission from these sections and by photoelectron emission from those sections of the photocathode situated near the gap at the edge of the baffle.

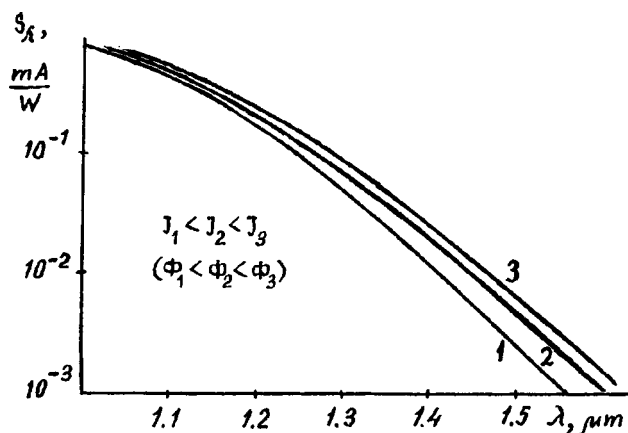


FIG. 2. Spectral sensitivity characteristics of the same point 3 on the photocathode adjacent to the baffle as a function of the radiation power 5 used for the measurements.

¹M. M. Butslav, B. M. Stepanov, and S. D. Fanchenko, *Image Converters and Their Application in Scientific Research* [in Russian], Nauka, Moscow (1978), 432 pp.

²Kh. N. Vezirov, *Pis'ma Zh. Tekh. Fiz.* **17**(14), 81 (1991) [Sov. Tech. Phys. Lett. **17**, 525 (1991)].

³A. A. Iznar, *Electron-Optical Devices* [in Russian], Mashinostroenie, Moscow (1977), 264 pp.

⁴A. H. Sommer, *Photoemissive Materials: Preparation, Properties, and Uses* (Wiley, New York, 1968; Énergiya, Moscow 1973, 177 pp.).

⁵I. M. Bronshtein and B. S. Fraiman, *Secondary Electron Emission* [in Russian], Nauka, Moscow (1969), 408 pp.

⁶*Handbook of Tables of Physical Quantities*, edited by I. K. Kikoin [in Russian], Nauka, Moscow (1976), 1008 pp.

Translated by R. M. Durham

Generation of superradiance pulses by high-current subnanosecond electron bunches moving in a periodic slow-wave structure

N. S. Ginzburg, Yu. V. Novozhilova, I. V. Zotova, A. S. Sergeev, A. D. R. Phelps, A. W. Cross, S. M. Wiggins, V. Khi, K. Ronald, V. G. Shpak, M. I. Yalandin, S. A. Shunaïlov, M. R. Ul'maskulov, and V. P. Tarakanov

Institute of Applied Physics, Russian Academy of Sciences, Nizhniĭ Novgorod Strathclyde University, Glasgow, UK

Institute of Electrophysics, Ural Branch of the Russian Academy of Sciences, Ekaterinburg Institute of High-Temperature Physics, Russian Academy of Sciences, Moscow

(Submitted March 23, 1998)

Pis'ma Zh. Tekh. Fiz. **24**, 7–13 (September 26, 1998)

The generation of ultrashort microwave pulses was observed experimentally in the superradiance of high-current electron bunches propagating through a periodic slow-wave structure. The process included particle bunching within the bunch followed by coherent emission from the entire volume of the bunch. © 1998 American Institute of Physics. [S1063-7850(98)01709-1]

An analysis of the multifrequency dynamics of backward-wave oscillators made in Ref. 1 showed that as the injection current increases, steady-state oscillation is replaced by self-modulation. It was observed that the amplitude of the first pulse formed under these conditions in the initial stage of the transition process is substantially (by a factor of two or three) greater than the amplitude of the steady-state oscillation. It was shown in Ref. 2 that this pulse is superradiant^{4–7} since its formation is partly attributable to electron bunching and partly to the relative influence of different parts of the electron pulse caused by slippage of the wave relative to the particles. As a result, in a certain range of parameters the peak power of this pulse increases as the square of the current, which is indicative of coherent emission in the initial part of the current pulse. Thus, if the length of the beam current pulse is limited to a level sufficient for the formation of a superradiant pulse, the generation of high-power ultrashort microwave signals may be predicted. The present paper reports an experimental investigation of the generation of subnanosecond pulses on the basis of this mechanism.

A RADAN-303 nanosecond accelerator with a subnanosecond pulse-shortening device was used to inject short, 0.5–0.9 ns, high-current, 1–2 kA, electron pulses with a particle energy of 220–250 keV (Refs. 8 and 9). These pulses were generated in a magnetically insulated coaxial explosive-emission diode. A specially designed diode assembly ensured that the accelerating gap could be varied smoothly in order to vary the injection current. The signals were recorded using a 7 GHz Tektronix-7250 digitizing oscilloscope. The high-current electron bunches were focused using a static magnetic field of up to 10 T generated by a superconducting solenoid. This field could sustain a pulse-periodic regime corresponding to an injector timing frequency of 25 Hz.

A typical oscilloscope trace of a microwave signal is shown in Fig. 1a, consisting of several pulses. The first pulse is the superradiant pulse and the subsequent pulses are produced by reflection of this pulse at the boundary between the

corrugated and regular exit waveguide. The amplitudes of the secondary pulses decreased appreciably as the depth of corrugation decreased smoothly at this boundary. However, additional reflections were useful to determine the group velocity of the radiation over the interval between pulses, which was 0.3 ns and agreed with the results of the numerical simulation of the superradiance process made using the KARAT code. Figure 2a shows the geometry of the system and the pattern of longitudinal electron bunching observed as the bunch passes through the slow-wave system. The envelope of the time dependence of the radiation power (Fig. 2b) accurately reproduces the oscilloscope trace of the microwave signal.

Figure 1b gives the peak power as a function of the guiding magnetic field. The figure clearly shows a region of cyclotron absorption near 3.5 T and two regions of emission with weak (1.5–3 T) and strong (>4 T) magnetic fields. It is known from previous studies of long-pulse relativistic backward-wave tubes that these sources have two regions of efficient generation separated by a cyclotron absorption band which appears when the cyclotron resonance condition is satisfied for the fundamental harmonic of the wave propagating in a periodic slow-wave system.^{10–13} The first experimental investigations of the generation of superradiant pulses on the basis of this mechanism were carried out using a relatively weak focusing magnetic field of 2 T generated by a pulsed solenoid,¹⁴ which was lower than the value corresponding to the cyclotron absorption band. Figure 1b shows that for strong (exceeding the resonance value) magnetic fields the peak radiation power is between four and five times higher than that obtained in previous experiments. The increase in power is mainly attributable to the improved quality of the hollow electron beam formed by the exploding cathode and to a reduction in the wall thickness to 0.4 mm. In addition, focusing of the electrons by the strong magnetic field allows the gap between the slow-wave system and the bunch to be reduced, which increases the coupling impedance and the corresponding gain.

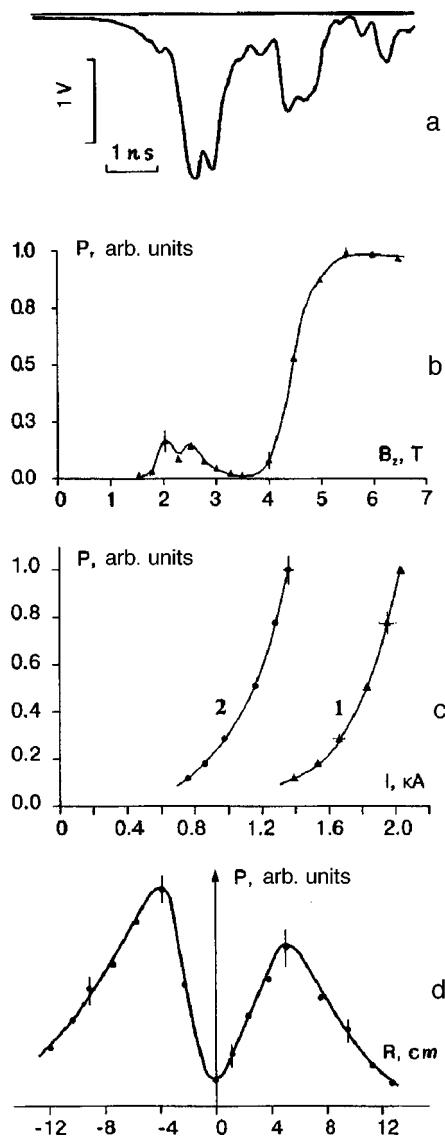


FIG. 1. a — Oscilloscope trace of microwave signal, b — peak power versus induction of guiding magnetic field, c — peak superradiance power versus injection current (I) and transmitted current (2), and d — angular distribution of radiation.

The peak power was investigated as a function of the bunch current by varying the length of the anode–cathode accelerating gap. When this gap was varied between 3 and 11 mm, the bunch current varied between 1.3 and 2.1 kA. However, this was accompanied by a change in the diode impedance and the average particle energy varied in the range 200–250 keV. Another complicating factor in the experiments was the misalignment (~ 0.5 mm) of the coil of the superconducting transporting solenoid and the electrodynamic slow-wave system, which resulted in appreciable current losses as the bunch passed through the drift channel.

Figure 1c gives the peak superradiance power as a function of the injection current and the transmitted current. Both dependences show satisfactory agreement with the quadratic dependence of the power on the current obtained from the theoretical analysis. The frequency measurements were made by observing the signal from a hot-carrier detector after the radiation had passed through waveguide filters with different

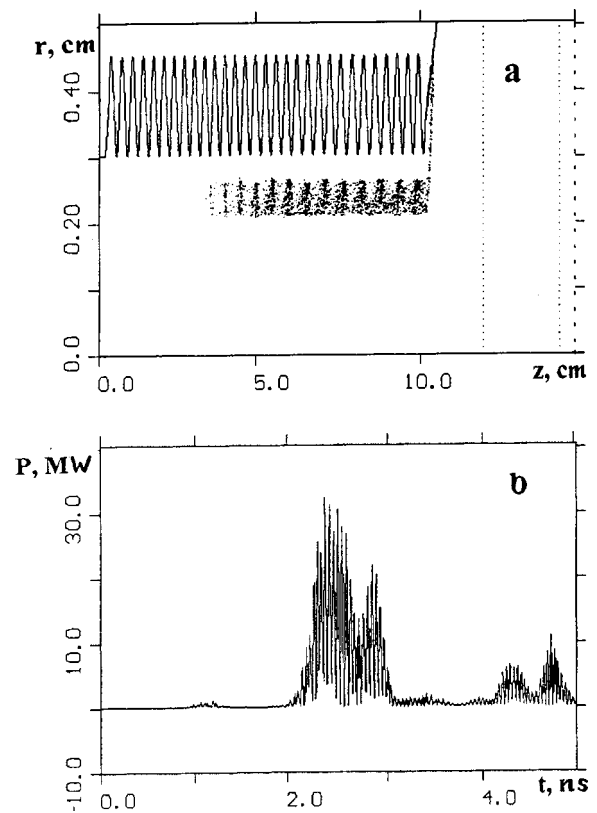


FIG. 2. Results of a simulation of superradiance: a — geometry of system in polar coordinates and particle bunching at time 1 ns; b — output power of radiation as a function of time.

cutoff frequencies. According to these measurements, the central radiation frequency corresponded to the calculated frequency of 39 GHz and the relative spectral band was 5%.

The radiation was polarized in the TM_{01} mode which, after emission into free space, has only the radial component of the electric field. When the receiving horn was rotated through 90° , the amplitude of the detector signal was reduced at least threefold. The angular distribution of the radiation measured by moving the horn along one of the coordinates is shown in Fig. 1d and has a minimum at the center characteristic of the TM_{01} mode. Note that the field distribution in Fig. 1d is asymmetric. This asymmetry can be attributed to the orientation of the germanium detector relative to the electric field gradient. The field distribution changes to mirror-symmetric when the detector is rotated through 180° . The absolute radiation power obtained by integrating the detector readings over the angular distribution gives an estimate of 4–5 MW. The high peak power of the radiation was also confirmed by the emission from a panel of neon lamps positioned 30 cm from the exit horn. In this case, the emission pattern accurately corresponded to the TM_{01} mode.

Another important factor confirming the high radiation power was the rf breakdown of air at atmospheric pressure which was observed when the radiation was focused by a parabolic mirror or inside a tapering conical waveguide. Moreover, a comparison with the results of previous observations of rf breakdowns from nanosecond and subnanosecond microwave and video pulses indicates that the real peak power was considerably higher than the level obtained from

the detector readings. At this point, it should be noted that experiments using backward-wave tubes with 4–5 ns microwave pulses^{13,15} indicate that a power level of 4–5 MW is insufficient for the evolution of breakdown even for such relatively long pulses. However, experiments using subnanosecond video pulses demonstrate¹⁵ that for such short durations the electric field breakdown strength should be 150 kV/cm. Using a standard procedure to calculate the field in a conical waveguide, we find that a radiation power of 25–30 MW should correspond to superradiant pulses of this field strength. Note that the detector was calibrated using a magnetron with 100 ns pulses. That is to say, we can assume that the signal power was considerably underestimated when subnanosecond pulses were recorded by the hot carrier detector.

The superradiant pulses exhibited a high degree of stability and reproducibility which allowed us to achieve a pulse-periodic regime at frequencies up to 25 Hz when the RADAN 303 accelerator was operated under suitable conditions.

To sum up, as a result of these investigations we have developed a new pulsed source based on the superradiance of high-current electron bunches. Microwave pulses were obtained with megawatt powers and durations less than 1 ns, which are the shortest so far recorded. Superradiant pulses will be of interest to study nonlinear effects in plasmas and solids, and also in localized applications.

This work was supported by the Russian Fund for Fundamental Research (Grant No. 95-02-04791).

- ¹N. S. Ginzburg, S. P. Kuznetsov, and T. M. Fedoseeva, *Izv. Vyssh. Uchebn. Zaved. Radiofiz.* **21**(7), 1037 (1978).
- ²N. S. Ginzburg, Yu. V. Novozhilova, and A. S. Sergeev, *Pis'ma Zh. Tekh. Fiz.* **22**(9), 39 (1996) [*Tech. Phys. Lett.* **22**, 359 (1996)].
- ³R. H. Bonifacio, C. Maroli, and N. Piovella, *Opt. Commun.* **68**(5), 369 (1988).
- ⁴R. H. Bonifacio, B. W. J. McNeil, and P. Pierini, *Phys. Rev. A* **40**, 4467 (1989).
- ⁵N. S. Ginzburg, *Pis'ma Zh. Tekh. Fiz.* **14**, 440 (1988) [*Sov. Tech. Phys. Lett.* **14**, 197 (1988)].
- ⁶N. S. Ginzburg and A. S. Sergeev, *JETP Lett.* **54**, 446 (1991).
- ⁷G. A. Mesyats *et al.*, in *Proceedings of the Ninth IEEE International Pulsed Power Conference*, Albuquerque, NM, 1993, p. 835.
- ⁸V. G. Shpak *et al.*, in *Proceedings of the 11th International Conference on High Power Particle Beams, BEAMS'96*, Prague, Czech Republic, 1996, p. 913.
- ⁹É. B. Abubakirov, N. S. Ginzburg, N. F. Kovalev, and M. I. Fuks, *Radiotekh. Elektron.* **34**, 1058 (1989).
- ¹⁰N. F. Kovalev, M. I. Petelin, M. D. Raizer *et al.*, *JETP Lett.* **18**, 138 (1973).
- ¹¹S. D. Korovin *et al.*, *Pis'ma Zh. Tekh. Fiz.* **11**(17), 1072 (1985) [*Sov. Tech. Phys. Lett.* **11**, 445 (1985)].
- ¹²M. I. Yalandin *et al.*, in *Proceedings of the Ninth IEEE International Pulsed Power Conference*, Albuquerque, NM, 1993, p. 388.
- ¹³N. S. Ginzburg, A. S. Sergeev, I. V. Zotova *et al.*, *Nucl. Instrum. Methods Phys. Res. A* **393**, 352 (1997).
- ¹⁴A. S. Elchaninov *et al.*, in *Proceedings of the International Conference on High-Power Particle Beams, BEAMS-86*, Kobe, Japan, 1986, p. 552.
- ¹⁵M. I. Yalandin *et al.*, in *Proceedings of the SPIE International Symposium on Intense Microwave Pulses III*, San Diego, 1995, *Proc. SPIE* **2557**, 289 (1995).

Translated by R. M. Durham

Phase synchronization of switching processes in a stochastic bistable system with an aperiodic external influence

A. N. Sil'chenko, T. Kapitanik, and V. S. Anishchenko

N. G. Chernyshevskii State University, Saratov

(Submitted March 20, 1998)

Pis'ma Zh. Tekh. Fiz. **24**, 14–21 (September 26, 1998)

The synchronization of switching in a stochastic bistable system perturbed by a chaotic signal is analyzed. The effect is described in terms of the classical theory of phase synchronization.

© 1998 American Institute of Physics. [S1063-7850(98)01809-6]

It is known that when self-oscillatory systems interact, mutual and forced synchronization of the oscillations takes place.¹ Recent studies have shown that these effects are also observed in chaotic self-oscillatory systems^{2–4} and in systems with noise-controlled time scales.^{5–8} In addition, the concept of the instantaneous phase of chaotic oscillations was rigorously introduced for a Rössler system and the mutual chaotic synchronization effect was described in terms of the classical theory of phase synchronization.^{9,10} The stochastic bistable system examined here is a model describing the motion of a Brownian particle in a two-well potential and belongs to a class of nonlinear systems which do not possess natural deterministic frequencies. Their dynamics depend strongly on the noise intensity and the characteristic time scale of these systems is the average time to escape from the potential well (the Kramers time).¹¹

Stochastic bistable systems perturbed by a weak periodic signal have recently attracted close attention in connection with studies of the stochastic resonance effect.^{12–14} The response of the system to a weak periodic influence is amplified substantially and reaches a maximum at an optimum selected noise level (stochastic resonance). In the limit of a small-amplitude periodic force, stochastic resonance is described in terms of linear response theory.^{15,16} When the amplitude of the periodic influence is comparable with (but remains smaller than) the potential barrier in a stochastic bistable system, switching synchronization occurs.⁷

An analysis of the degree of predictability of the response of a bistable system using different measures of complexity revealed that stochastic synchronization is caused by self-organization of the system.⁸ The effect of mutual stochastic synchronization of switching processes in a system of two coupled bistable oscillators perturbed by statistically independent noise sources was analyzed for the first time in Refs. 6 and 18. In this case, the system has absolutely no deterministic time scales and as the coupling increases, interaction is observed between statistical time scales of the subsystems defined as moments of the distribution function. In Ref. 17 mutual and forced synchronization of switching processes in bistable stochastic systems was analyzed from the point of view of classical phase synchronization theory.

The results of recent investigations have shown that stochastic resonance also occurs in the more complicated case

when the influence is aperiodic. The concept of aperiodic stochastic resonance was introduced in Refs. 19 and 20 and it was also shown that the response of a bistable system to a slowly varying aperiodic influence may be optimized by noise. Noise optimization of the process of information transfer between two unidirectionally coupled nonlinear oscillators generating chaotic series of pulses was demonstrated in Ref. 21.

The aim of the present study is to describe aperiodic stochastic resonance in terms of phase synchronization theory. The input signal is taken as the signal generated by a certain dynamic system under conditions of dynamic chaos, whose amplitude is comparable with the height of the potential barrier. In the absence of noise, the amplitude of the signal is insufficient to cause switching in the bistable system.

As already noted, the basic model used to analyze stochastic resonance and aperiodic stochastic resonance is that of an overdamped bistable system perturbed by white Gaussian noise and an external signal described by the following stochastic differential equation

$$\dot{x} = \alpha x - x^3 + \sqrt{2D}\xi(t) + \mu y(t), \quad (1)$$

where μ is a certain constant, $y(t)$ is a chaotic signal, $\xi(t)$ is Gaussian white noise, the parameter D determines the noise intensity, and the parameter α determines the depth of the symmetric potential wells (in our case $\alpha=5$).

We shall first consider the case when the input signal is generated by a Rössler system:

$$\begin{aligned} \dot{x}_1 &= \tau(-x_2 - x_3), & \dot{x}_2 &= \tau(x_1 + 0.15x_2), \\ \dot{x}_3 &= \tau(0.2 + x_3(x_1 - 6.26)). \end{aligned} \quad (2)$$

In this case, we have $y(t)=x_1$, $\mu=0.42$, and $\tau=0.01$ (by introducing time normalization, we increase the base period of the chaotic oscillations compared with the characteristic relaxation time within the potential wells). It was shown in Ref. 10 that for a Rössler system the instantaneous phase of the chaotic oscillations can be correctly introduced by several methods. In our specific case, the instantaneous phase of the influence and the instantaneous phase of the response of a bistable system will be determined using the concept of an analytic signal^{22,23} by means of a Hilbert transform, which

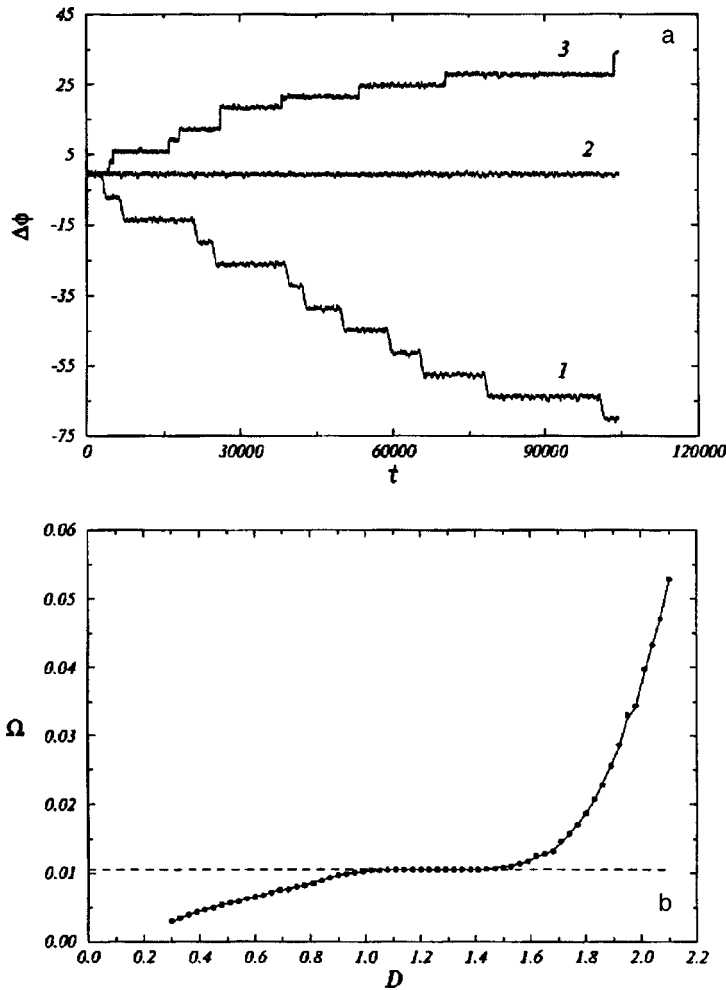


FIG. 1. a) Time dependence of the phase difference for various noise intensities for an input signal from a Rössler system: curve 1 — $D=0.9$, curve 2 — $D=1.15$, curve 3 — $D=1.4$; b) mean frequency Ω (solid curve) and mean switching frequency (circles) versus noise intensity; the dashed curve gives the mean frequency of the chaotic oscillations in the system.

has been widely used in radiophysics^{24,25} and signal processing theory.²⁶ As we know, the Hilbert transform maps an arbitrary signal $s(t)$ into an analytic signal $\psi(t)=s(t)+is_H(t)=a(t)e^{i\phi(t)}$, where $a(t)=\sqrt{s(t)^2+s_H(t)^2}$ and $\phi(t)=\arctan(s_H(t)/s(t))$, and the function $s_H(t)$ is the Hilbert transform of the initial signal $s(t)$:

$$s_H(t) = 1/\pi \int_{-\infty}^{\infty} s(\tau) d\tau / (t - \tau)$$

(the integral is taken in the sense of the Cauchy principal value).

In the classical case considered in Ref. 27, the stochastic differential equation for the phase difference has the form

$$\Delta \dot{\phi} = \delta - \epsilon \sin(\Delta \phi) + \xi(t). \tag{3}$$

In this case, the phase difference $\Delta \phi$ diffuses in the potential $V(\Delta \phi) = -\delta \Delta \phi - \epsilon \cos(\Delta \phi)$, fluctuating for a long time within the potential wells and undergoing occasional 2π jumps.²⁷ In our case, the phase of the influence is given by $\dot{\phi} = \langle \omega \rangle + \rho(\phi)$, where $\rho(\phi)$ is a small “phase noise” in the Rössler system⁹ and $\langle \omega \rangle$ is the mean frequency of the chaotic oscillations. Despite the existing phase modulation of the input signal, phase synchronization of the switching is observed at some noise intensity, as in the case of a periodic influence. In this case, the phase difference fluctuates around some fixed value (curve 2 in Fig. 1a). In the absence of synchronization the phase difference increases without

bound, accomplishing 2π jumps (curves 1 and 3 in Fig. 1a). Figure 1b gives the mean frequency $\Omega = \langle \dot{\phi} \rangle$ and the mean switching frequency determined neglecting intrawell motion, plotted as a function of the noise intensity. It can be seen that these two characteristics exhibit identical behavior and in some range of noise intensities coincide with the mean frequency of the chaotic oscillations in a Rössler system.

We shall now consider the case when the x -variable of a Lorenz system is taken as the input signal:

$$\dot{x}_1 = 10(y - x)\tau, \quad \dot{y} = (28x - y - xz)\tau, \quad \dot{z} = (xy - 8/3z)\tau. \tag{4}$$

In this case in Eq. (1) we have $y(t)=x$, $\mu=0.245$, and $\tau=0.005$. It can be seen from Fig. 2a that, as in the previous case, at some noise intensity phase synchronization of the switching is observed in the stochastic bistable system and the phase difference remains bounded (curve 2), whereas outside the synchronization range the phase difference increases without bound (curves 1 and 3). Moreover, as can be seen from Fig. 2b, the mean frequency $\Omega = \langle \dot{\phi} \rangle$ and the mean switching frequency of the bistable system demonstrate identical behavior and in a certain range of noise intensities coincide with the mean switching frequency in the Lorenz system. The investigations showed that if the chaotic

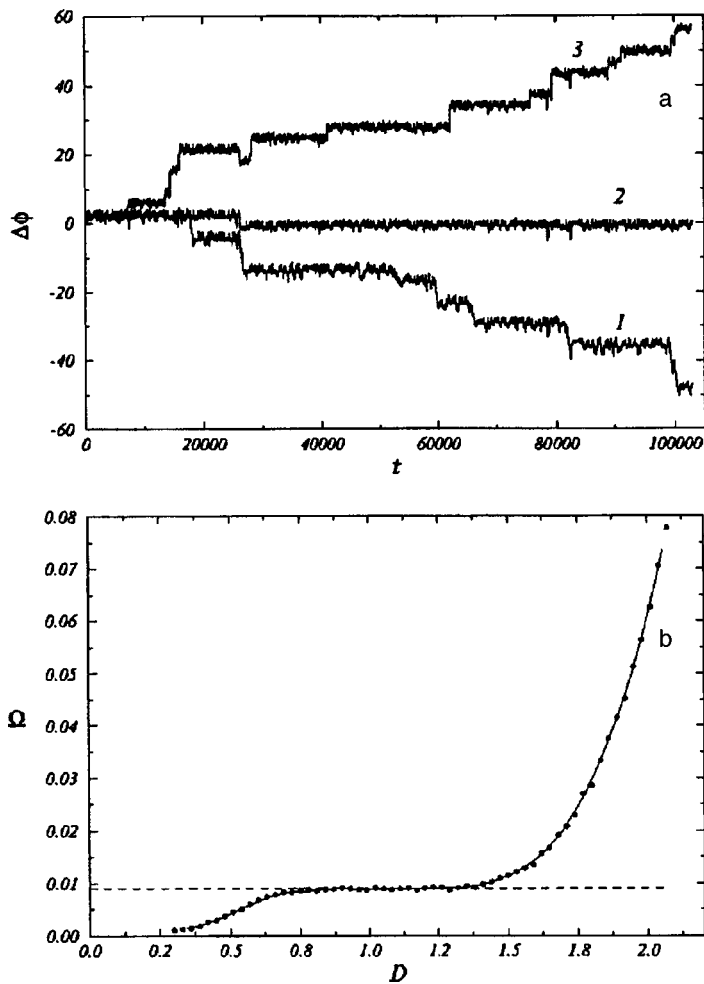


FIG. 2. a) Time dependence of the phase difference for various noise intensities for an input signal from a Lorenz system: curve 1 — $D=0.76$, curve 2 — $D=1.0$, curve 3 — $D=1.3$; b) mean frequency Ω (solid curve) and mean switching frequency (circles) versus noise intensity; the dashed curve gives the mean switching frequency in the Lorenz system.

influence has a small amplitude, locking of the mean frequencies and phase synchronization are not observed.

Thus, the results indicate that in a stochastic bistable system excited by a chaotic signal, phase synchronization of the switching and locking of the mean frequency of the chaotic influence are observed.

The authors are grateful to A. B. Neiman for discussions of the results.

- ¹I. I. Blekhnman, *Synchronization of Dynamic Systems* [in Russian], Nauka, Moscow (1971).
- ²V. S. Afraimovich, N. N. Verichev, and M. I. Rabinovich, *Izv. Vyssh. Uchebn. Zaved. Radiofiz.* **29**, 795 (1986).
- ³V. S. Anishchenko, T. E. Vadivasova, D. É. Postnov, and M. A. Safonova, *Radiotekh. Elektron.* **36**, 338 (1991).
- ⁴I. I. Blekhnman, P. S. Landa, and M. G. Rosenblum, *Appl. Mech. Rev.* **48**, 733 (1995).
- ⁵L. Gammaitoni, F. Marchesoni, and S. Santucci, *Phys. Rev. Lett.* **74**, 1052 (1995).
- ⁶A. B. Neiman, *Phys. Rev. E* **49**, 3484 (1994).
- ⁷B. V. Shulgin, A. B. Neiman, and V. S. Anishchenko, *Phys. Rev. Lett.* **75**, 4157 (1995).
- ⁸A. Neiman, B. Shulgin, V. Anishchenko, W. Ebeling, L. Schimansky-Geier, and J. Freund, *Phys. Rev. Lett.* **76**, 4299 (1996).
- ⁹M. G. Rosenblum, A. S. Pikovsky, and J. Kurths, *Phys. Rev. Lett.* **76**, 1804 (1996).

- ¹⁰A. S. Pikovsky, M. G. Rosenblum, G. V. Osipov, and J. Kurths, *Physica D* **104**, 219 (1997).
- ¹¹P. Hänggi, P. Talkner, and M. Borkovec, *Rev. Mod. Phys.* **62**, 251 (1990).
- ¹²K. Wiesenfeld and F. Moss, *Nature (London)* **373**, 33 (1995).
- ¹³A. R. Bulsara and L. Gammaitoni, *Phys. Today* **49** No. 3, 39, (1996).
- ¹⁴L. Gammaitoni, P. Hänggi, P. Jung, and F. Marchesoni, *Rev. Mod. Phys.* **70**, 223 (1998).
- ¹⁵M. I. Dykman, P. V. E. McClintock, R. Mannella, and N. Stokes, *JETP Lett.* **52**, 141 (1990).
- ¹⁶P. Jung and P. Hänggi, *Phys. Rev. A* **44**, 8032 (1991).
- ¹⁷A. N. Sil'chenko, A. B. Neiman, and V. S. Anishchenko, *Pis'ma Zh. Tekh. Fiz.* **24**(15), 12 (1998) [*Tech. Phys. Lett.* **24**, 586 (1998)].
- ¹⁸A. Neiman and L. Schimansky-Geier, *Phys. Lett. A* **197**, 379 (1995).
- ¹⁹J. J. Collins, C. C. Chow, and T. T. Imhoff, *Phys. Rev. E* **52**, R3321 (1995).
- ²⁰J. J. Collins, C. C. Chow, A. C. Capela, and T. T. Imhoff, *Phys. Rev. E* **54**, 5575 (1996).
- ²¹C. Eichwald and J. Walleczek, *Phys. Rev. E* **55**, R6315 (1997).
- ²²D. Gabor, *J. IEE London* **93**, 429 (1946).
- ²³P. Panter, *Modulation, Noise and Spectral Analysis* (McGraw-Hill, New York, 1965).
- ²⁴S. M. Rytov, *Principles of Statistical Radiophysics, Vol. 1: Elements of Random Process Theory*, 2nd ed., Springer-Verlag, New York (1987); Nauka, Moscow (1976).
- ²⁵L. A. Vaňshtein and D. E. Vakman, *Frequency Separation in the Theory of Oscillations and Waves* [in Russian], Nauka, Moscow (1983).
- ²⁶J. S. Bendat and A. G. Piersol, *Random Data: Analysis and Measurement Procedures* (Wiley, New York, 1986; Mir, Moscow 1989).
- ²⁷R. L. Stratonovich, *Topics in the Theory of Random Noise*, Gordon and Breach, New York (1963); Sovetskoe Radio, Moscow (1961).

Resonant conversion of plasmons in a rippled metal–insulator structure

V. A. Sychugov, A. V. Tishchenko, B. A. Usievich, and I. F. Salakhutdinov

Institute of General Physics, Russian Academy of Sciences, Moscow
(Submitted March 2, 1998)

Pis'ma Zh. Tekh. Fiz. **24**, 22–29 (September 26, 1998)

The propagation of long-range plasmons on a rippled metal film embedded in an insulator is studied. It is shown that the ripple of the film leads to the appearance of additional dissipative losses of these plasmons. It is established that these additional losses are caused by resonant coupling between long-range and short-range plasmons produced by the ripple of the film.

© 1998 American Institute of Physics. [S1063-7850(98)01909-0]

More than fifteen years have elapsed since it was shown in Ref. 1 that plasmons whose range substantially exceeds that of plasmons at a metal–insulator interface may exist in a thin metal film embedded in an insulator. So far, however, few experimental and theoretical studies have been devoted to long-range plasmons, and the literature contains very few reports of experimental observations and investigations of this type of plasmon.^{2–6} This is to a considerable extent attributable to the complexity of fabricating thin solid metal films ($h < 10$ nm) and also the need to ensure that the refractive indices of the media containing the metal film are the same.

As we know, long-range plasmons are usually excited using a total-internal-reflection prism or a rippled metal film. It was noted in Ref. 6 that in this last case, the usual resonant decay of the amplitude of the light beam reflected from the metal surface may be replaced by its resonant amplification as a result of the so-called “total” external reflection of light.⁷ This effect is the result of interference between the wave reflected by the structure and the wave emitted from the structure as a result of its ripple. The constructive nature

of the interference is responsible for a resonant increase in the amplitude of the reflected wave.

In order to achieve a high reflection coefficient, the dissipative losses of the long-range plasmons should be substantially lower than the radiation losses caused by the ripple of the metal film. It was shown in Ref. 6 that this condition may be satisfied with a suitable choice of film thickness, ripple period, and depth. As an example, Fig. 1 shows the calculated and experimentally determined angular dependence of the coefficient of reflection of a light beam (all the calculations and experiments were made for $\lambda = 0.63 \mu\text{m}$) from the surface of a thin rippled copper film ($h = 9$ nm) with ripple period $\Lambda = 0.37 \mu\text{m}$ and depth $2\sigma = 33$ nm. The metal film was positioned between media having refractive indices of 1.512 and 1.507.

Our investigations showed that the problem of selecting suitable parameters of the rippled structure for the existence of long-range plasmons is complicated by the existence of so-called short-range plasmons which have high dissipative losses and high propagation constants. Figure 2 gives these parameters for short- and long-range plasmons as a function

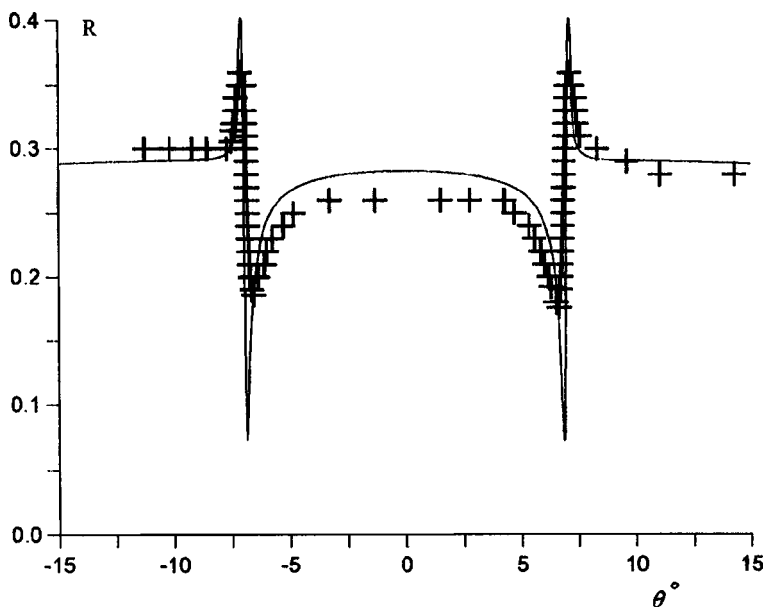


FIG. 1. Angular dependence of the coefficient of reflection of light from the rippled surface of a thin copper film of thickness $h = 9$ nm, $2\sigma = 33$ nm, and $\Lambda = 0.37 \mu\text{m}$. The calculated curve was obtained for $\epsilon = (-27.0, 5.0)$.

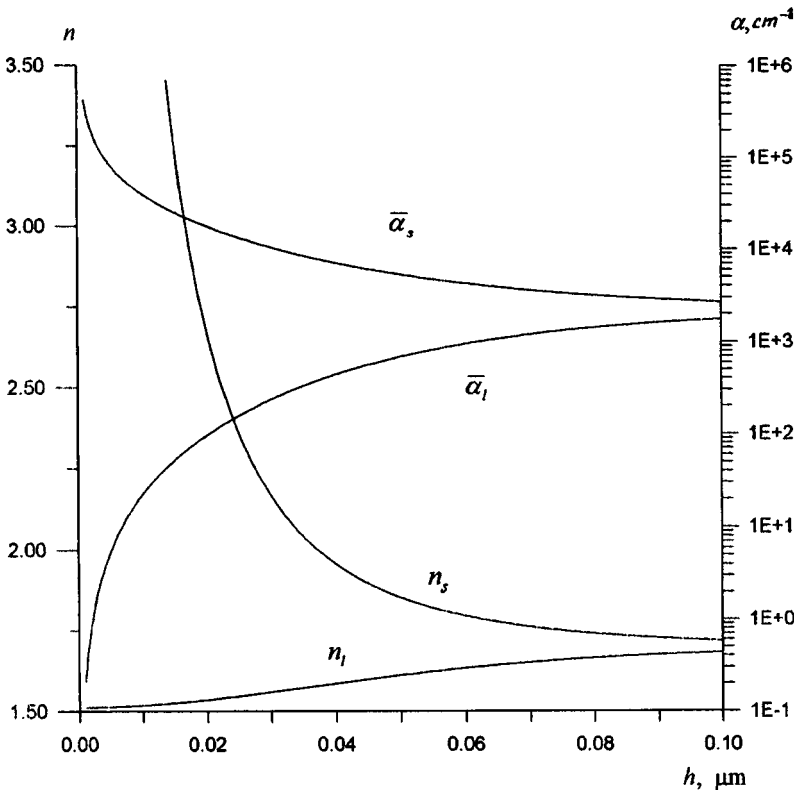


FIG. 2. Real part of the propagation constants n of long- and short-range plasmons and attenuation factor α as a function of the thickness of the copper film.

of the thickness of a copper film embedded in an insulator with $n = 1.512$. When the ripple of this structure has a suitable period, this may lead to compensation of the difference between the propagation constants of the long- and short-range plasmons propagating in the same direction, i.e., they become equal:

$$k(n_s^* - n_l^*) = K = \frac{2\pi}{\Lambda}, \tag{1}$$

where n_l^* and n_s^* are the effective refractive indices of the long- and short-range plasmons, respectively.

This factor is responsible for the resonant transfer of energy between the plasmons. In this particular case, the long- and short-range plasmons propagate in the same direction and as a result of the strong attenuation of the short-range plasmon, energy is transferred from the long-range to the short-range plasmon. If a long-range plasmon is excited at a grating, its amplitude $A_l(x)$ varies along the grating within the exciting beam as follows:

$$\frac{dA_l}{dx} = -\bar{\alpha}_l A_l - \tilde{\alpha}_{\text{rad}} A_l - \kappa A_s + \beta A_{\text{in}}, \tag{2}$$

$$\frac{dA_s}{dx} = -\bar{\alpha}_s A_s + \kappa A_l, \tag{3}$$

where κ is the coefficient of coupling of two plasmons at the grating, $\bar{\alpha}_{l(s)}$ is the attenuation factor of a long-range (short-range) plasmon moving over a smooth metal film, $\tilde{\alpha}_{\text{rad}}$ is the radiative loss factor of the long-range plasmon, $A_{l(s)}$ are the plasmon amplitudes, A_{in} is the amplitude of the incident

wave, and β is the coefficient of coupling between the incident wave and a long-range plasmon excited by this wave.

In the Rayleigh–Fourier approximation, the coefficient of coupling between the plasmons has the form

$$\kappa^2 = \frac{(N_0^s)^2 (N_0^l)^2}{h_l n_l h_s n_s} \left[k\sigma \frac{\epsilon_1 n_s n_l - \epsilon_0 N_1^l N_1^s}{(\epsilon_0 + \epsilon_1) n_s n_l - \epsilon_0 \epsilon_1} \right]^2, \tag{4}$$

where

$$h_{l(s)} = h - \frac{2\epsilon_0 \epsilon_1}{ik N_1^{l(s)} [(\epsilon_0 + \epsilon_1) n_{l(s)}^2 - \epsilon_0 \epsilon_1]},$$

$$N_0^{l(s)} = \sqrt{\epsilon_0 - n_{l(s)}^2}, \quad N_1^{l(s)} = \sqrt{\epsilon_1 - n_{l(s)}^2}$$

n_l, n_s are the propagation constants of the long- and short-range plasmons normalized to $k = 2\pi/\lambda$.

Figure 3 gives κ as a function of the thickness of the metal film ($2\sigma = 33 \text{ nm}$). The coupling coefficient not only determines the length $L = \pi/(2|\kappa|)$ for transfer of energy from the long-range to the short-range plasmon, but also the attenuation factor of the long-range plasmon at the grating. The attenuation factor of long-range plasmons in a rippled metal film is higher than the attenuation $\bar{\alpha}_l$ on a smooth film. This increase is attributed to the radiation losses $\tilde{\alpha}_{\text{rad}}$ of the long-range plasmons at the ripple and the additional dissipative losses $\tilde{\alpha}_{\text{dis}}$ caused by the transfer of energy from long-range to short-range plasmons:

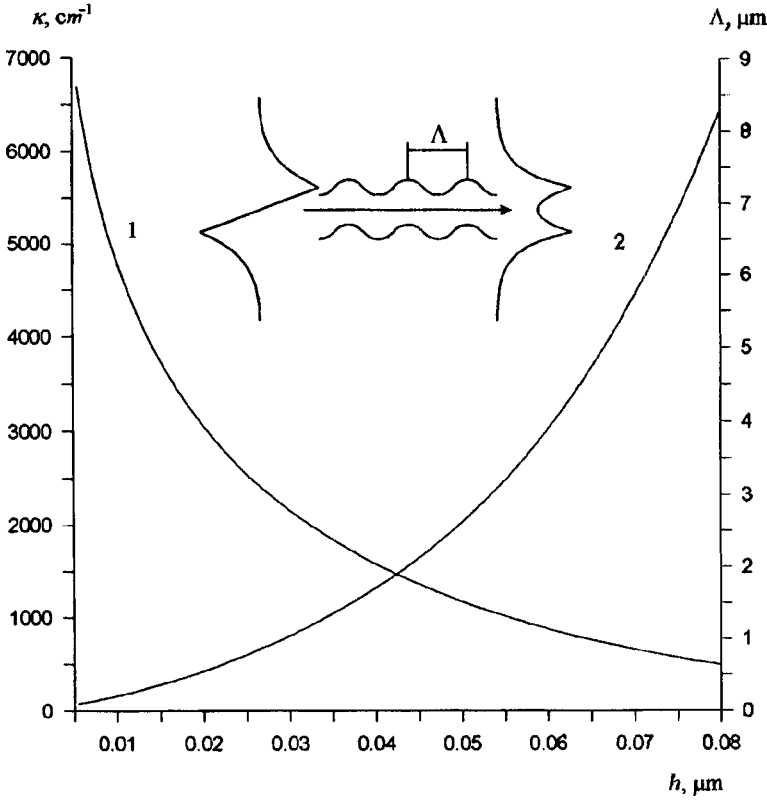


FIG. 3. Coupling coefficient between long- and short-range plasmons at a rippled copper film as a function of film thickness (curve 1) and resonant period of the ripple as a function of film thickness (curve 2).

$$\alpha = \bar{\alpha}_l + \tilde{\alpha}_{\text{rad}} + \tilde{\alpha}_{\text{dis}}, \quad (5)$$

where

$$\begin{aligned} \tilde{\alpha}_{\text{rad}} = \text{Re} \left\langle \frac{(N'_0)^2 \left(\frac{k\sigma}{2} \right)^2 \left[2N'_1 + 2(\varepsilon_0 - \varepsilon_1) \right. \right. \\ \times \frac{(\varepsilon_1 n_l n_r - \varepsilon_0 N'_1 N'_1)}{(\varepsilon_0 + \varepsilon_1) n_l^2 - \varepsilon_0 \varepsilon_1} \left. \left. \frac{n_l n_r}{i \varepsilon_1 N'_0 \cot \left(\frac{k N'_0 h}{2} \right) + \varepsilon_0 N'_1} \right. \right. \\ \left. \left. + \frac{N'_1 N'_0}{\varepsilon_1 N'_0 + i \varepsilon_0 N'_1 \cot \left(\frac{k N'_0 h}{2} \right)} \right] \right\rangle, \quad (6) \end{aligned}$$

$$\tilde{\alpha}_{\text{dis}} = \frac{|\kappa|^2}{\bar{\alpha}_s}, \quad (7)$$

where $N'_{0,1} = \sqrt{\varepsilon_{0,1} - n_r^2}$, and $n_r = n_l - \lambda/\Lambda$ is the normalized projection of the wave vector of the exciting plasma of the bulk wave.

Equation (7) was obtained from Eqs. (2) and (3) assuming that the excitation of a long-range plasmon on a rippled metal film is a steady-state process.

Figure 4 gives the additional attenuation factor of a long-range plasmon on a rippled copper film ($h = 9 \text{ nm}$, $\lambda = 0.37 \text{ } \mu\text{m}$, $2\sigma = 33 \text{ nm}$) as a function of the thickness of the metal film. The position of the resonant absorption peak of a long-range plasmon on the thickness scale h (for a given wavelength) is determined by the period of the ripple, the amplitude is determined by the ripple depth, and the width

by the short-range plasmon losses. Figure 5 gives the dependence $R(\Theta)$ for two thicknesses of copper film. In particular, Fig. 5 shows that the reflection peak disappears when the long-range plasmon losses are high. We should also mention the—at first glance—paradoxical observation deduced from formula (7): the additional dissipative losses for long-range plasmons decrease as the loss factor for a short-range plasmon at a smooth metal surface increases. However, if we

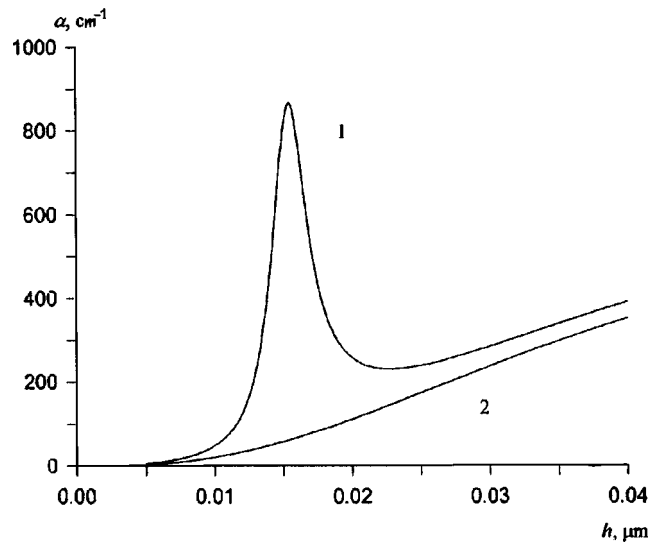


FIG. 4. Dependence of the additional losses $\tilde{\alpha}_{\text{rad}} + \tilde{\alpha}_{\text{dis}}$ (curve 1) and $\tilde{\alpha}_{\text{rad}}$ (curve 2) of a long-range plasmon at a rippled copper film versus thickness ($2\sigma = 33 \text{ nm}$).

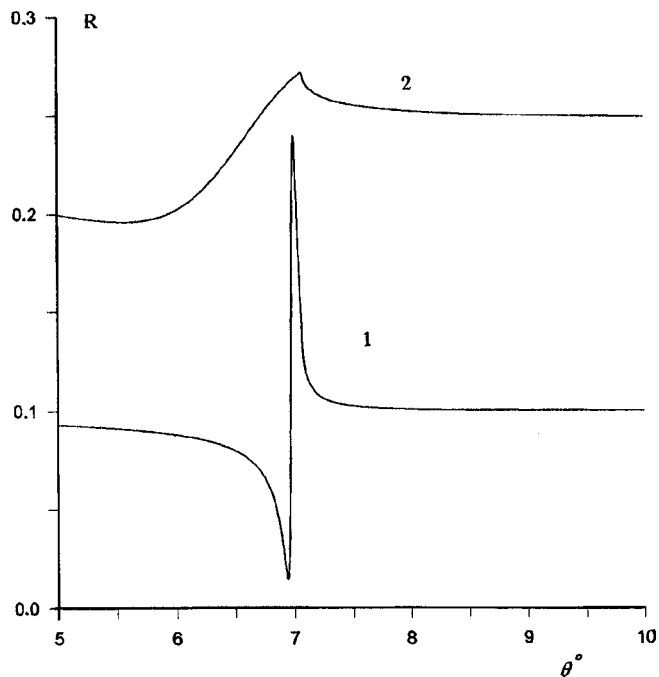


FIG. 5. Angular dependence of the coefficient of reflection of light from the rippled surface of a thin metal film for $h=9$ nm (curve 1) and 16.3 nm (curve 2). The thickness of 16.3 nm corresponds to the maximum additional loss factor.

bear in mind that the fraction of energy transferred from the long-range to the short-range plasmon depends on the amplitude of the excited short-range plasmon, which is inversely

proportional to the losses $\bar{\alpha}_s$, the dependence of $\bar{\alpha}_{\text{dis}}$ on $\bar{\alpha}_s$ given by formula (7) becomes understandable and almost obvious.

To sum up, the energy loss mechanism in a long-range plasmon at a rippled metal film identified in our analysis imposes certain constraints on the choice of parameters of the rippled structure which must be taken into account when developing any devices using surface electromagnetic waves in thin rippled metal films. We also note that studies of sinusoidal gratings are needed. Only these gratings can ensure minimum additional losses, because otherwise coupling between long-range and short-range plasmons can occur at higher-order spatial harmonics of the grating profile.

This work was supported by the Russian Fund for Fundamental Research, Grant No. 97-02-16857.

¹D. Sarid, Phys. Rev. Lett. **47**, 1927 (1981).

²F. Yang, J. R. Sambles, and G. W. Bradberry, Phys. Rev. B **44**, 5855 (1991).

³R. A. Booman, G. A. Olson, and D. Sarid, Appl. Opt. **25**, 2729 (1986).

⁴K. R. Welford and Y. R. Sambles, J. Mod. Opt. **35**, 1467 (1988).

⁵T. Sterkenburgh and H. Franke, J. Appl. Phys. **81**, 1011 (1997).

⁶I. F. Salakhutdinov, V. A. Sychugov, A. V. Tishchenko *et al.*, Kvant. Elektron. (Moscow) **24**, 815 (1997).

⁷G. A. Golubenko, A. S. Svakhin, V. A. Sychugov, and A. V. Tishchenko, Kvantovaya Elektron. (Moscow) **12**, 1334 (1985) [Sov. J. Quantum Electron. **15**, 886 (1985)].

Translated by R. M. Durham

Fiber-optic gyroscope with suppression of excess noise from the radiation source

É. I. Alekseev, E. N. Bazarov, Yu. A. Barannikov, V. P. Gapontsev, V. P. Gubin,
I. É. Samartsev, and N. I. Starostin

Institute of Radio Engineering and Electronics, Russian Academy of Sciences (Fryazino Branch)
(Submitted March 5, 1998)

Pis'ma Zh. Tekh. Fiz. **24**, 30–35 (September 26, 1998)

A new optical system is proposed and investigated experimentally for a Sagnac fiber interferometer in which the excess noise of the wide-band radiation source is suppressed. A tenfold improvement in the sensitivity of a fiber-optic gyroscope with an erbium/ytterbium fiber superfluorescent light source was achieved experimentally. It is shown that the identity of the polarization characteristics of the interferometer channels plays an important role.

© 1998 American Institute of Physics. [S1063-7850(98)02009-6]

Recent progress achieved in low-coherence interferometry, including fiber-optic gyroscopy, is to a considerable extent attributable to the successful development of superfluorescent fiber sources using fibers doped with ions of rare-earth metals.¹ A promising source for fiber-optic gyroscopes is an erbium/ytterbium superfluorescent fiber source² which has a high output power and highly stable parameters in the 1.55 μm range.

It has been established that superfluorescent fiber sources (and other wide-band radiation sources) have an enhanced level of intensity noise (excess noise), which may be between one and two orders of magnitude higher than the fundamental limit determined by the shot noise. The properties of the excess noise are such that it can be compensated in various two-channel systems for photodetection of the interferometer signal.^{2–5} This involves equalizing the delay times of the radiation in the signal and reference channels whose polarization characteristics should be identical. In Refs. 4 and 5 the noise in a Sagnac interferometer is compensated by using an additional fiber delay line in the reference channel. In Ref. 6 we proposed a fiber-optic gyroscope in which both channels were based on a common fiber circuit and a balanced detector using a specially directed 3×3 coupler.

Here we propose and investigate experimentally a new optical system for a Sagnac fiber interferometer with compensation for the excess noise of the source. We also identify the mechanisms limiting the degree of suppression of the excess noise in two-channel optical systems used in fiber interferometers.

The apparatus (Fig. 1) consists of a “minimal” circuit of an all-fiber fiber-optic gyroscope with an additional channel to compensate for the noise of the superfluorescent fiber source (1). The minimal circuit is formed by a polarizer P_1 (2), a directional coupler DC_1 (3), a phase modulator PM (4), a fiber loop FL (5) (with a fiber length of 500 m and diameter 13 cm), and a signal photodetector PD_1 (6), with a polarization-insensitive optical circulator OC (7) used as the input coupler. The main elements of the reference channel are a coupler DC_2 (8) at one end of the fiber loop, a polarizer P_2 (9), and a photodetector PD_2 (10). In addition, two polarization controllers PC_1 (11) and PC_2 (12) are also incorpo-

rated in the circuit to fine-tune the polarization characteristics of the channels required for the elements of an isotropic fiber. A controllable fiber attenuator CA (13) is also included to vary the optical power.

Thus, in this system the fiber loop is used in the signal and reference channels of the interferometer so that the difference between the time delays of the signals may be made fairly small and stable, which is required for efficient noise suppression.

The output signals from the photodetectors are fed to a subtractor (14), and the first harmonic of the modulation frequency generated by a master oscillator MO (15) at frequency 42 kHz is detected by a phase detector PD (16).

The Er/Yb superfluorescent fiber source is similar to that described in Ref. 2. The output power is 80 mW and the spectrum has a power-weighted mean width $\Delta\lambda = 7$ nm with an average wavelength $\lambda_0 = 1.54 \mu\text{m}$.

Figure 2 gives the coefficient of noise suppression $K = U/U_c$ as a function of the optical power P at the photodetector. Here U and U_c are the mean-square noise voltage at the exit from the subtractor without and with compensation. The measurements were made for several configurations of the optical system: curve 1 for the complete circuit shown in Fig. 1, curve 2 in the absence of PC_2 , and curve 3 in the absence of P_2 and PC_2 in the reference channel. Note that PC_1 is used for tuning to the maximum of the interference signal of the fiber-optic gyroscope. In this case, the plane of polarization of the input radiation is oriented parallel to one of the axes of birefringence of the fiber loop, as can be assessed from the remanent polarization of the radiation at the exit from the reference channel: this is 52% for optimum tuning of PC_1 and decreases to 29% in the worst case as a result of depolarization in the fiber loop.

Figure 2 also gives the calculated dependence $K(P) = U/U_c$ (curve 4). The values of U_c (allowing for summation of the uncorrelated noise in both channels) and U are $U_c = (2U_h^2 + 2U_d^2 + 2U_e^2 + 2U_s^2)^{1/2}$ and $U = (U_c^2 + U_{ex}^2)^{1/2}$, where U_h , U_d , U_e , U_s , and U_{ex} are the mean-square voltages of the resistor thermal noise, the shot noise of the photodiode dark current, the electronics noise, and the shot and

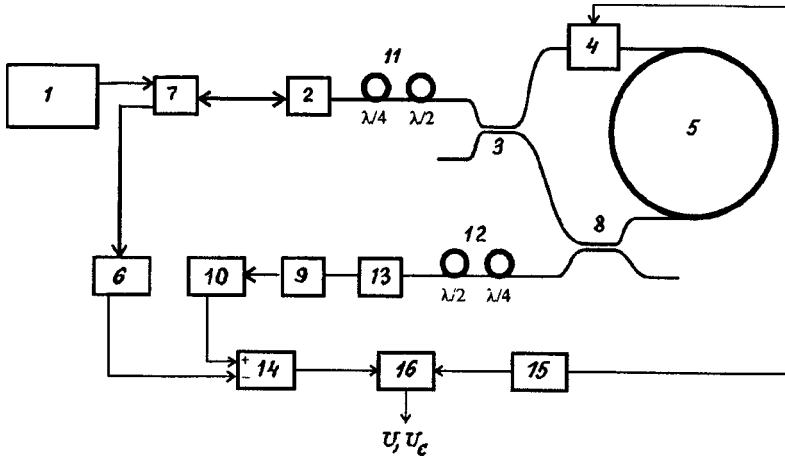


FIG. 1. Schematic diagram of apparatus.

excess radiation noise, respectively, where $U_h^2 = 4k_B TRB$, $U_d^2 = 2ei_d R^2 B$, $U_e^2 = \rho_e B$, $U_s^2 = 2eqPR^2 B$, and $U_{ex}^2 = q^2 P^2 R^2 \lambda_0^2 B / \Delta \lambda c$. Here k_B is the Boltzmann constant, T and R are the temperature and resistance of the photodetector resistor, B is the measurement band, e is the electron charge, i_d is the dark current of the photodetector, ρ_e is the spectral density of the electronics noise, q is the quantum sensitivity of the photodiode, and c is the velocity of light. The calculations were made for $T=300$ K, $R=1.4$ k Ω , $i_d=30$ nA, $\rho_e = 3$ nV/Hz^{1/2}, and $q=0.75$ A/W.

It can be seen from Fig. 2 that in this fiber-optic gyroscope system, the excess noise of the source is suppressed almost to the level of the radiation shot noise (curves 1 and 4). A necessary condition for this is that the signal and reference channels of the interferometer have identical polariza-

tion characteristics, which is achieved by tuning P_2 and PC_2 . Investigations show that the main mechanism limiting the degree of suppression of the excess noise is depolarization of the radiation in the long fiber loop, which leads to the appearance of an unpolarized component at the fiber exit whose noise is not correlated with that of the polarized input component. This can explain the weak suppression of the noise when the signal and reference channels of the interferometer are not completely identical (curves 2 and 3 in Fig. 2). Note that in the absence of an unpolarized component (for example, when the elements of the fiber-optic gyroscope are made of a fiber which conserves the polarization in which one polarization mode is excited) the elements P_2 and PC_2 are not needed for noise compensation.

The sensitivity of this prototype fiber-optic gyroscope with noise suppression was ~ 0.4 K/h (for $B=100$ Hz and $P=140$ μ W) which was ten times better than that without the noise suppression system. This value corresponds to a random walk coefficient⁵ of 7×10^{-4} K/(h)^{1/2}. A relatively wide band was selected to ensure that the white noise of the radiation exceeded the short-term zero variations of the fiber-optic gyroscope caused by other mechanisms (polarization pedestal).

To sum up, we have proposed and investigated experimentally a new Sagnac fiber interferometer system where the excess noise of the radiation source is suppressed. It is shown that the degree of noise suppression may be limited by depolarization of the radiation if the polarization characteristics of the signal and reference channels are nonidentical. A tenfold improvement (almost to the level of the radiation shot noise) in the sensitivity of a fiber-optic gyroscope with a 1.55 μ m erbium/ytterbium fiber source was achieved experimentally.

The authors are grateful to A. I. Sazonov, V. V. Fomin, V. M. Brylov, and B. G. Ignatov for assistance and useful discussions.

This work was supported by the Russian Fund for Fundamental Research, Grant No. 96-02-18434.

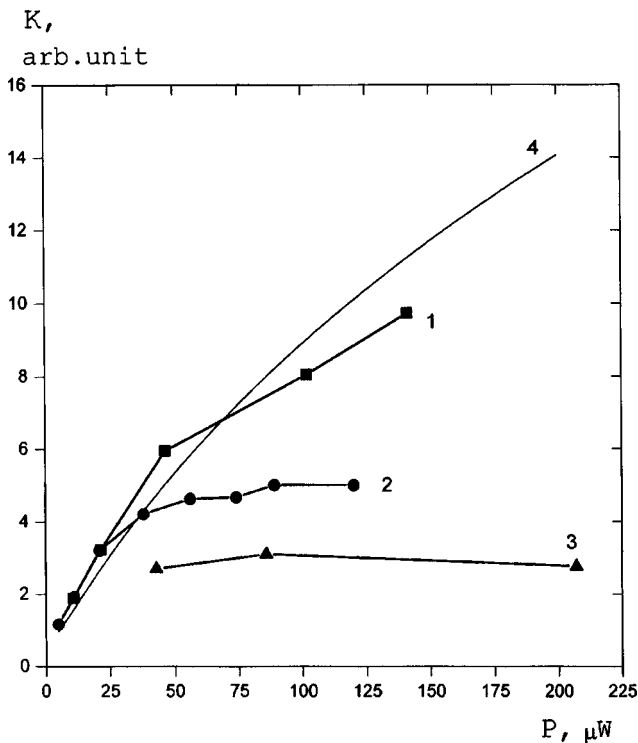


FIG. 2. Degree of noise suppression versus optical power at photodetector: 1 — with polarizer and controller in reference channel, 2 — only with polarizer, 3 — without polarizer and controller, and 4 — calculated values.

¹ P. F. Wysocki, M. J. F. Digonnet, B. J. Kim, and H. J. Shaw, J. Lightwave Technol. 12, 550 (1994).

² É. I. Alekseev, E. N. Bazarov, Yu. A. Barannikov et al., Pis'ma Zh. Tekh. Fiz. 23(23), 1 (1997) [Tech. Phys. Lett. 23, 899 (1997)].

³P. R. Morkel, R. I. Laming, H. O. Edwards, and D. N. Payne, in *Proceedings of the Conference on Lasers and Electrooptics, CLEO'90*, Anaheim, Calif. (1990), p. 154.

⁴R. P. Moeller and W. K. Burns, *Opt. Lett.* **16**, 1902 (1991).

⁵W. K. Burns and R. P. Moeller, *Proc. SPIE* **2837**, 381 (1996).

⁶E. I. Alekseev and E. N. Bazarov, *Pis'ma Zh. Tekh. Fiz.* **23**(15), 36 (1997) [*Tech. Phys. Lett.* **23**, 589 (1997)].

Translated by R. M. Durham

Influence of condensation of the emission spectrum on intracavity laser spectral analysis

A. P. Savikin and V. B. Tsaregradskii

N. I. Lobachevskii State University, Nizhnii Novgorod

(Submitted March 31, 1998)

Pis'ma Zh. Tekh. Fiz. **24**, 36–43 (September 26, 1998)

A model of condensation of the laser emission spectrum in the spectral ranges of the absorption lines of the substance being studied was developed on the basis of a frequency-dependent absorbing intracavity lens. This model can explain most spectral condensation effects. It was shown that condensation of the emission spectrum is generally observed experimentally as a deformation of the dip profile in the laser emission spectrum. An analysis is made of the possibility of determining the concentration of an absorbing substance by measuring the spectral position of the peak of the condensed line. © 1998 American Institute of Physics. [S1063-7850(98)02109-0]

INTRODUCTION

In the wide-band variant of intracavity laser spectroscopy information on the object being studied is obtained by analyzing the shape and intensity of the absorption line profile (dips in the laser emission spectrum at the position of the absorption lines). In view of the high sensitivity of the emission spectrum to frequency-dependent insertion losses and the speed of the analysis, the intracavity method has been widely used to study weakly absorbing media. While the method was being developed, an increase in the output intensity of the laser radiation was recorded experimentally in spectral ranges corresponding to the absorption lines of the gaseous medium in the cavity of the wide-band laser.¹ In some cases, the laser emission spectrum collapsed to form narrow lines whose spectral position on either side of the center of the absorption line was unpredictable.

This effect, which has attracted the attention of many researchers, was subsequently called emission spectrum condensation.

It was shown in Ref. 2 that the lens-like property of the intracavity absorbing medium arises because the refractive index exhibits a spectral dependence as a result of the selective absorption and a geometrical dependence as a result of the radial concentration gradient

Such properties are exhibited for example, by the gas discharge in the tube of an OKG-13 He–Ne laser with a capillary diameter of 1.8–2.0 mm and by alkali metal vapor in the tube furnace of a graphite atomizer which we used in our experiments.

The condensation mechanism was explained in terms of changes in the losses. An analysis of the stability of a two-mirror cavity configuration containing a selectively absorbing medium with a transversely nonuniform refractive index³ showed that the increase in the spectral power of the output radiation is caused by a reduction in the total losses (as a result of diffraction) for the cavity modes located in the spectral regions of the absorption lines compared with the losses of the empty cavity modes.

This model of condensation based on a frequency-dependent absorbing intracavity lens explains most of the spectral condensation effects observed in our experiments and in those carried out by other researchers.

The dependence of the laser radiation spectrum on the characteristics of the absorbing medium near resonance lines suggests that spectral condensation may be used in spectral analysis. In many cases, this may be slightly preferable to varying the relative depth of the dips by an intracavity method. This particularly applies to high-intensity resonance lines which completely quench the lasing.

EXPERIMENT AND DISCUSSION OF RESULTS

The experiments were carried out with a pulsed laser using ethanol solutions of organic dyes. Pumping was provided by second harmonic pulses from a YAG:Nd³⁺ laser at an angle of a few degrees to the longitudinal axis of a two-mirror cavity.

The experiment showed that the intracavity field has no appreciable influence on the spectral position of the condensation line. The condensed line is located at the same distance from the center of the absorption line for both the output radiation spectrum from the beam axis and from the edge of the beam (Fig. 1).

In intracavity laser spectral analysis, the sensitivity (the relative depth of the dips in the lasing spectrum) depends strongly on the degree of excess of the pumping over the threshold.⁴

In addition, as in Ref. 4, it was shown in our experiments that if the width of the monochromator instrumental function exceeds the absorption line width, this reduces the sensitivity of the intracavity laser spectroscopy and leads to substantial errors in the quantitative measurements.

This is because if the resolution of the spectral apparatus is inadequate, radiation from parts of the spectrum matched with the absorption line $\Delta\nu_{\text{abs}}$ and from other sections $\Delta\nu_{\text{las}}$ is incident on the photodetector. The lower the resolution of the monochromator, the larger the ratio $\Delta\nu_{\text{las}}/\Delta\nu_{\text{abs}}$ and the

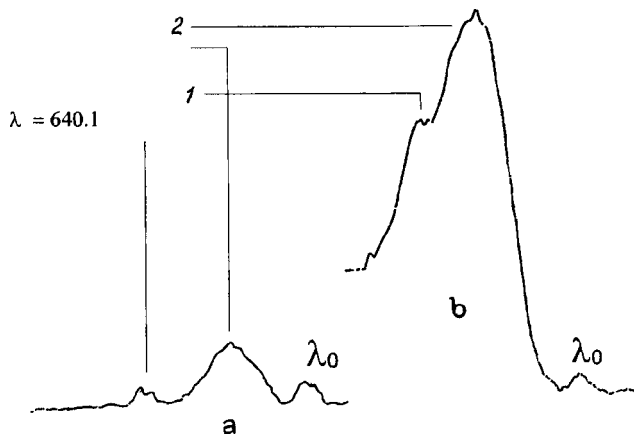


FIG. 1. Condensation of the emission spectrum of a dye laser in the Ne absorption range $\lambda_0 = 640.23$ nm ($\Delta\lambda_e = -0.057$ nm): a — beam edge, b — beam center; 1 — emission line, 2 — condensed line.

smaller is the relative depth of the dips in the lasing spectrum for the same quantities of absorbing material.

Intracavity laser spectra obtained experimentally using the method of crossed dispersions of a diffraction monochromator and a Fabry–Perot interferometer were used to estimate the sublevel populations of the 1S Ne metastable state in a gas discharge, which showed good agreement with the data given in Ref. 5.

Table I gives various parameters for three closely spaced spectral lines.

It can be seen that the distance of the condensed line peak from the center of the absorption line is proportional to the transition intensity Nf , so that the concentration of a substance and the transition probability can be determined by measuring $\Delta\lambda_e$.

A DFS-8 spectrograph can measure wavelength to within 5×10^{-3} nm, which gives an error of around 1% in the measurements of Nf .

It was shown in Ref. 6 that the spectral dependence of the focal length of a selective gas lens is determined by the refractive index of the medium near the absorption line with the wavelength λ_0 :

$$F(\lambda) = \frac{a^2 \alpha}{8l} \frac{\Delta\lambda}{N_m f_{mn}} \frac{9n}{9m}, \quad (1)$$

where a is the tube diameter, l is its length,

$$\alpha = 4\pi m c^2 / (l^2 \lambda_0^3),$$

g_m and g_n are the statistical weights of the lower and upper levels of a transition with the oscillator strength f_{mn} , and $\Delta\lambda = \lambda - \lambda_0$.

TABLE I.

λ , nm	640.225	633.443	638.299
Transition	$1S_5 \rightarrow 2P_9$	$1S_5 \rightarrow 2P_8$	$1S_4 \rightarrow 2P_7$
f	0.37	0.08	0.17
Nf , cm^{-3}	6×10^{11}	1.3×10^{11}	1×10^{11}
$\Delta\lambda_e$, nm	0.03–0.07	0.014	0.01

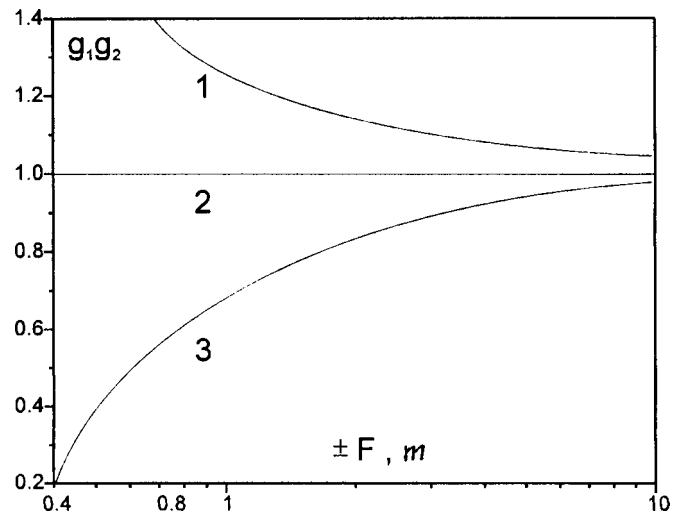


FIG. 2. Curves of $g_1 g_2(F)$ for a cavity with plane mirrors. $L = 0.3$ m, $l = 0.04$ m, $l_1 = 0.1$ m, and $l_2 = 0.26$ m. Focal length of intracavity lens: 1 — $F < 0$; 2 — $F = \infty$; 3 — $F > 0$.

The principal planes of the system coincide with the center of the absorbing cell. The optical strength of the lens is proportional to the transition intensity $N_m f$ and decreases with distance from the center of the absorption line. After measuring the spectral position of the condensed line and checking the estimated dependence of the configurational parameters on the optical strength of the intracavity lens, we can find the transition parameters.

This method was used to estimate the concentration of sodium vapor in a graphite atomizer.

The cavity of a laser using an ethanol solution of rhodamine 6G was formed by plane wedge-shaped mirrors. The unfilled cavity ($r_{1,2} = \infty$) is located at the stability boundary. The parameters g_1 and g_2 for a cavity with an intracavity lens have the form⁶

$$g_1 = 1 - \frac{l_2}{F} - \frac{l}{2F} = 1 - \frac{2l_2 + l}{2F},$$

$$g_2 = 1 - \frac{2l_1 + l}{2F}. \quad (2)$$

To estimate the stability of the cavity, we take the following parameters: cavity length $L = 0.3$ m, length of graphite rod in atomizer $l = 0.04$ m, distance between ends of rod and nontransmitting and exit mirrors $l_1 = 0.1$ m, $l_2 = 0.26$ m, respectively:

$$g_1 g_2 = (1 - 0.28/F)(1 - 0.12/F). \quad (3)$$

The dependence $g_1 g_2(F)$ is plotted in Fig. 2. For all real values of F , a positive lens transfers the cavity to the stable region, gradually ($F \rightarrow \infty$) approaching the boundary $g_1 g_2 = 1$. In this case, the diffraction losses decrease. A negative lens transfers the cavity to the region $g_1 g_2 > 1$ with high diffraction losses. Thus, in an axisymmetric aligned cavity condensation should only be observed from one wing of the absorption line.

Investigations reported in Ref. 6 indicate that a thermal lens induced by the pump radiation in a laser medium does

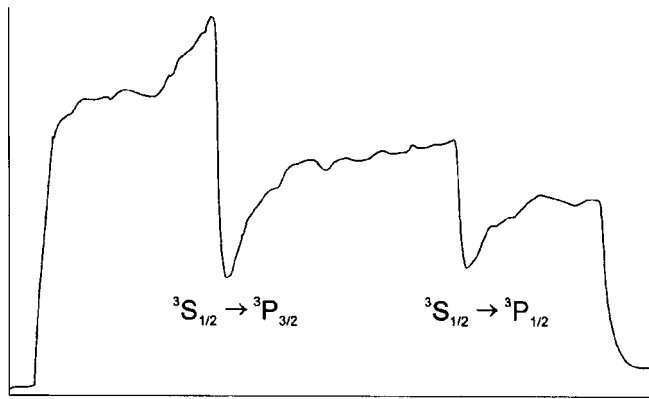


FIG. 3. Condensation of the emission spectrum of a rhodamine laser near the absorption lines of atomic sodium.

not have time to affect the condensation because of the time required for its formation. It was shown in Ref. 3 that when the temperature varies over in the cross section of the tube furnace of a graphite atomizer, the absorbing vapor forms a selective gas lens which is diverging on the long-wavelength wing and converging on the short-wavelength wing of the absorption line. As a result, condensation of the emission spectrum will be observed most frequently at $\lambda = \lambda_0 - \Delta\lambda$.

At the distance $\Delta\lambda \approx 0.12$ nm from the center of the absorption line of the $3^2S_{1/2} - 3^2P_{1/2}^0$ $f = 1.03$ sodium transition at $\lambda = 588.995$ nm, no amplification of the lasing intensity is observed (Fig. 3). It can be seen from the dependence $g_1 g_2 (1/F)$ in Eq. (2) that for $F = 10$ m we obtain $g_1 g_2 = 0.96$, which is almost equal to $g_1 g_2 = 1$. Using expression (1), we obtain $Nf \approx 5 \times 10^{13} \text{ cm}^{-3}$. Taking into account the oscillator strength of the transition, we obtain the concentration $N \approx 5 \times 10^{13} \text{ cm}^{-3}$ which corresponded to the sodium concentration in the volume being analyzed (volume of inner cavity of tube furnace $V \approx 0.5 \text{ cm}^3$, mass $m \approx 10^{-9} \text{ g}$).

CONCLUSIONS

Although these estimates are preliminary and require additional measurements, this approach to the phenomenon of condensation from the viewpoint of the losses proved fruit-

ful. Not only was the increase in the spectral power explained but various additional details in the condensation of the emission spectrum were also identified. It was found that this effect was characterized not only by an increase, but also by a decrease in intensity additional to the absorption. As a result of the corresponding dependence of the configurational parameters of a cavity with a selective intracavity gas lens, the spectral dependence of the selective diffraction losses is a combination of extended sections of enhanced and reduced intensity in the lasing spectrum near the wings of the absorption lines (Fig. 3).

Thus, condensation is generally observed as a deformation of the dip profile in the laser emission spectrum. The increase in the spectral power of the laser radiation in the presence of condensation may differ and may be observed over a fairly broad spectral range. In our experiment³ the distortion of the absorption line profile observed as a more steeply sloping dip and a more gently sloping opposite side (compared with the undistorted profile) was observed down to low concentrations of the absorbing substance, as far as 10^{-9} g/cm^3 .

Thus, in quantitative analyses using intracavity laser spectroscopy, the spectral dependence of the configurational parameters of the laser system must be estimated and attempts should also be made to suppress the lens property of the absorbing medium.

¹P. K. Runge, *Opt. Commun.* **4**, 195 (1971).

²O. S. Morozov, A. P. Savikin, and V. B. Tsaregradskiĭ, in *Abstracts of Papers presented at the Conference on Nonlinear and Coherent Effects in Intracavity Laser Spectroscopy*, Kirovograd, 1988 [in Russian], p. 24.

³O. S. Morozov, A. P. Savikin, and V. B. Tsaregradsky, *Laser Phys.* **5**, 899 (1995).

⁴S. F. Luk'yanenko, M. M. Makogon, and L. N. Sinitsa, *Intracavity Laser Spectroscopy: Principles and Applications* [in Russian], Nauka, Novosibirsk (1985), 121 pp.

⁵*Spectroscopy of Gas-Discharge Plasmas*, edited by S. É. Frish [in Russian], Nauka, Leningrad (1970), 362 pp.

⁶V. A. Gur'ev, M. S. Malyshev, and A. P. Savikin, *Holography: Theoretical and Applied Topics* [in Russian] (1995), p. 200.

Translated by R. M. Durham

Gasdynamic phenomena accompanying the motion of shock waves and objects in a low-temperature nonequilibrium plasma

A. P. Bedin

A. F. Ioffe Physicotechnical Institute, Russian Academy of Sciences, St. Petersburg

(Submitted March 30, 1998)

Pis'ma Zh. Tekh. Fiz. **24**, 44–49 (September 26, 1998)

An analysis is made of gasdynamic anomalies observed during the motion of shock waves and objects in a low-temperature nonequilibrium plasma. It is shown that these anomalies are associated with behavior of sound propagating in a nonequilibrium plasma. © 1998 American Institute of Physics. [S1063-7850(98)02209-5]

It has now been established as a result of experimental investigations that when a shock wave or a flying object enters a gas discharge zone, the following anomalous effects occur: acceleration of shock waves^{1–8} and changes in their structure,^{5–8,10,11} changes in the flow around objects (in particular, increased separation of the shock wave front from the object),¹² changes in the aerodynamic characteristics of objects, especially the drag coefficient,^{13,14} changes in the ablation and heat flux to the object,¹⁵ and so on. These effects are observed when shock waves and objects propagate in weakly ionized nonequilibrium glow and rf discharge plasmas in different gases (air, Ar, CO₂, and so on) at pressures of 1–100 Torr, gas kinetic temperatures $T = 300$ –1400 K, electron temperatures $T_e = 1$ –6 eV, and $n_e = 5 \times 10^{10}$ – 10^{12} cm⁻³.

Although these phenomena vary greatly, in each case the same factor is responsible for their occurrence, that is the characteristic of sound propagation in nonequilibrium excited media. The present study is based on this viewpoint.

A specific feature of the propagation of shock waves in a weakly ionized nonequilibrium plasma is that the single-wave structure characteristic of normal gases changes to a three-wave structure, comprising leader, precursor, and residual wave. Each element of this split shock wave has its own amplitude and moves at its own velocity, where $V_L > V_P > V_R$ (the subscripts L , P , and R refer to the leader, the precursor, and the residual wave, respectively). The leader is formed as a result of a perturbation of the charged component of the plasma and has a small amplitude because of the low concentration of this component in a gas discharge so that it has no appreciable influence on the gasdynamic processes. The precursor is formed by a packet of high-frequency acoustic waves and the residual wave is formed by low-frequency acoustic waves. Their separation arises from the difference in the velocities of the precursor and the residual wave ($V_P > V_R$) and is also attributable to the appreciable difference, and in some cases change in sign, of the damping factor of high-frequency sound in nonequilibrium excited media (see the review presented in Ref. 16). The propagation velocities of the precursor and the residual wave are related by $V_R/V_P \approx 0.68$ (see Fig. 1). Also plotted is the normalized precursor velocity (its parameters are

denoted by the subscript P) as a function of the shock wave velocity V in air unperturbed by a discharge, $\bar{V}_P/\sqrt{T_P} = V_P\sqrt{T}/V\sqrt{T_P} = f(V)$. The solid curve corresponds to

$$V_P = V(1 + 0.46e^{-0.7(M-1)})\sqrt{T_P}/T, \quad (1)$$

which averages the experimental data for $\bar{V}_P/\sqrt{T_P} > 1$ (the case $\bar{V}_P/\sqrt{T_P} = 1$ corresponds to equilibrium flows). It can be seen that although the data given in Ref. 9 correctly reflect the tendency of the ratio $\bar{V}_P/\sqrt{T_P}$ to increase for $M = V/a \rightarrow 1$ (a is the velocity of sound in air), they nevertheless lie outside the general dependence $\bar{V}_P/\sqrt{T_P} = f(V)$. Thus, the averaged curve is plotted neglecting these data. It follows from Eq. (1) that the velocity of sound in the plasma is $a_P = 1.46a\sqrt{T_P}/T$. Estimates made using the change in the separation of the shock wave front in the plasma¹² give $a_P = 1.48a\sqrt{T_P}/T$, and those made using the change in the drag coefficient¹⁷ give $a_P = 1.45a\sqrt{T_P}/T$. With this in mind, Eq. (1) may be rewritten as

$$M_P = M(1 + 0.46e^{-0.7(M-1)})/1.46. \quad (2)$$

It is clear from Eqs. (1) and (2) that the propagation velocity of strong shock waves in the plasma (precursor) is the same as in air heated to the temperature of the plasma. However, the Mach number in the plasma is 1.46 times lower than that in heated air. The propagation velocity of weak shock waves in the plasma is higher and the Mach number is lower than that in heated air. Assuming that the velocity of the residual wave is $V_R = 0.68V_P$ and taking $a_P = 1.46a_R$, we can easily establish that $M_R = M_P$, i.e., the propagation velocity of the residual wave is lower than that of the precursor but their Mach numbers are the same.

Similar phenomena (acceleration of shock waves, their splitting into three waves, and changes in the velocity of sound) are found in an Ar plasma (Fig. 1, see also data given in Refs. 2, 3, and 5). The data plotted in Fig. 1 indicate that the velocity of sound in an Ar plasma may be $a_P \sim 1.3a\sqrt{T_P}/T$.

Since $V_P > V_R$ holds and the damping factor of high-frequency sound decreases appreciably and even changes sign in nonequilibrium excited media, the precursor, comprising the high-frequency part of the shock wave, is sepa-

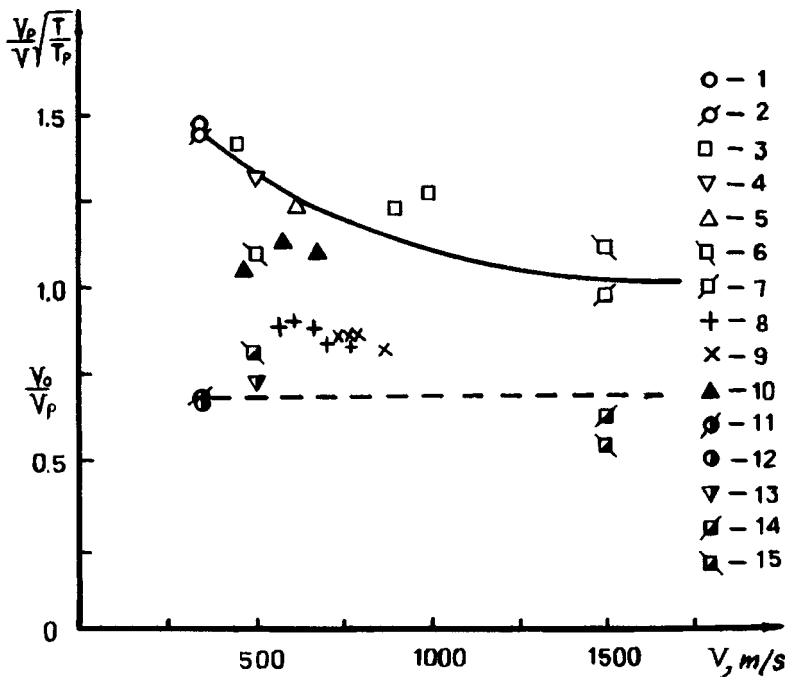


FIG. 1. Relative propagation velocities of precursor and residual wave in plasma as a function of shock wave velocity in a gas unperturbed by a discharge. Precursor, air: 1 — Ref. 12, 2 — Ref. 17, 3 — Ref. 4, 4 — Ref. 7, 5 — Ref. 5, 6 — Ref. 6, 7 — Ref. 8, 8 — Ref. 9, input energy 450 W; 9 — Ref. 9, input energy 100 W; argon: 10 — Ref. 3. Residual wave, air: 11 — Ref. 17, 12 — Ref. 12, 13 — Ref. 7, 14 — Ref. 8, and 15 — Ref. 6.

rated from the residual wave by the distance $\Delta_{PR} = (V_P - V_R)t \approx 0.5V_R t$, which only increases with time. Thus, under the conditions of a ballistic experiment, the precursor is always outside the field of view of the objective when a model is photographed, and the photographs only show the model and the residual wave (see Ref. 15, for example). The increase in the separation of the precursor from the residual wave has the result that from a certain time onward, the precursor ceases to influence the residual wave and thus the flow around the object. In a gas discharge the flow parameters behind the precursor and the residual wave can thus be calculated using the number $M_R = M_P$ (see Eq. (2)) and the parameters of unperturbed flow, using the equation for a normal shock. If the separation of the precursor from the residual wave is not too great, the perturbation of the flow field ahead of the residual wave must be taken into account to calculate the flow parameters behind this wave. Table I gives the results of calculations of the ratio of the static pressures behind the precursor in a plasma at $T = 350$ K and behind a shock wave propagating in air at the velocity $V = 500 - 1500$ m/s at $T = 293$ K, which are compared with an experiment carried out under the same conditions. The calculations were made using the standard formulas for a normal shock using Eq. (2), where the adiabatic exponent was taken to be 1.4 for air and 1.3 for plasma.

It can be seen from Table I that the calculated data agree satisfactorily with the experiment. The static pressure behind strong shock waves in plasma is approximately half that in air, according to the tabular data. The initial pressure behind

the shock waves and the pressure behind the shock waves reflected by the walls is also substantially lower in plasma than in air.¹⁷ This implies that the local loads on an object flying into plasma should be substantially lower than those in normal air. The aerodynamic characteristics of simple objects and the forces acting on them in a plasma may be estimated approximately from results of their measurements in any gas using the conversion relations

$$C_{X,Y,P} = C_{X,Y} \bar{P}'_{RP} / \bar{P}'_R,$$

$$X_P, Y_P = 0.5 C_{X,Y} \rho_P V^2 \bar{P}'_{RP} / \bar{P}'_R, \tag{3}$$

where $\bar{P}'_R = 2P'_R / \rho V^2$, P'_R is the pressure at the critical point of the object, X and Y are the drag and the lift of the object, and the subscript P refers to the plasma. Such a conversion is possible because in any two media including a plasma we have $C_{X,Y1} / \bar{P}'_{O1} \approx C_{X,Y2} / \bar{P}'_{O2}$ (Ref. 17). In any conversion it should be borne in mind that for an object having the same flight velocities, the number $M = M_R = M_P$ in a plasma is ~ 1.5 times lower than that in air heated to the plasma temperature. It should be noted that at subsonic flight velocities ($M_R < 0.8$) this conversion is unlikely to give good results because of a possible substantial variation of the base pressure in the plasma. In addition to reducing the local and integrated loads, the lower Mach number M in a plasma compared with heated air should also lead to a lower initial

TABLE I.

$V, m/s$	500	500	1250	1500	1500
P_{2P}/P_2 calculated	0.814	0.814	0.519	0.493	0.493
P_{2P}/P_2 experimental	0.761 (Ref. 6)	0.667 (Ref. 7)	0.426 (Ref. 8)	0.561 (Ref. 8)	0.463 (Ref. 6)

temperature and density behind the shock wave. Estimates show that in a plasma the specific heat flux at the critical point on a sphere

$$q_R = 0.9 Pr_2^{-0.6} C_p (T_r - T_w) \sqrt{\rho_2} \mu_2 V_\infty / R, \quad (4)$$

where R is the radius of the sphere and the remaining notation is conventional, is approximately half that in hot air. For the estimates it was assumed that the Prandtl number, the specific heat, and the viscosity of the air and the plasma are the same. However, the experimental data¹⁵ indicate that the ablation at a sphere and thus the heat flux to it are approximately four times lower in a plasma compared with heated air. It can thus be postulated that in a nonequilibrium plasma the transport coefficients vary and in particular, the viscosity is lower than that of equilibrium heated air. This must influence the flow of plasma around objects in subsonic flight regimes.

¹A. I. Klimov, A. N. Koblov, G. I. Mishin *et al.*, *Pis'ma Zh. Tekh. Fiz.* **8**, 439 (1982) [*Sov. Tech. Phys. Lett.* **8**, 192 (1982)].

²I. V. Basargin and G. I. Mishin, Preprint No. 880 [in Russian], A. F. Ioffe Physicotechnical Institute, Academy of Sciences of the USSR, Leningrad (1984), 22 pp.

³I. V. Basargin and G. I. Mishin, *Pis'ma Zh. Tekh. Fiz.* **11**, 209 (1985) [*Sov. Tech. Phys. Lett.* **11**, 85 (1985)].

⁴A. I. Klimov, G. I. Mishin, and A. B. Fedotov, *Pis'ma Zh. Tekh. Fiz.* **15**(20), 31 (1989) [*Sov. Tech. Phys. Lett.* **15**, 800 (1989)].

⁵I. V. Basargin and G. I. Mishin, in *Main Results of Scientific Activity, 1989/90* [in Russian], A. F. Ioffe Physicotechnical Institute, Academy of Sciences of the USSR, Leningrad (1991), pp. 100–103.

⁶G. I. Mishin, A. I. Klimov, and A. Yu. Gridin, *Pis'ma Zh. Tekh. Fiz.* **17**(16), 84 (1991) [*Sov. Tech. Phys. Lett.* **17**, 602 (1991)].

⁷A. Yu. Gridin and A. I. Klimov, *Khim. Fiz.* **12**, 363 (1993).

⁸A. Yu. Gridin, A. I. Klimov, and K. V. Khodataev, *Teplofiz. Vys. Temp.* **32**, 486 (1994).

⁹P. A. Voïnovich, A. P. Ershov, S. E. Ponomareva *et al.*, *Teplofiz. Vys. Temp.* **29**, 582 (1991).

¹⁰I. V. Basargin and G. I. Mishin, *Pis'ma Zh. Tekh. Fiz.* **15**(8), 55 (1989) [*Sov. Tech. Phys. Lett.* **15**, 311 (1989)].

¹¹I. V. Basargin and G. I. Mishin, *Zh. Tekh. Fiz.* **66**(7), 198 (1996) [*Tech. Phys.* **41**, 742 (1996)].

¹²G. I. Mishin, Yu. L. Serov, and I. P. Yavor, *Pis'ma Zh. Tekh. Fiz.* **17**(11), 65 (1991) [*Sov. Tech. Phys. Lett.* **17**, 413 (1991)].

¹³A. P. Bedin and G. I. Mishin, *Pis'ma Zh. Tekh. Fiz.* **21**(1), 14 (1995) [*Tech. Phys. Lett.* **21**, 5 (1995)].

¹⁴A. P. Bedin, Preprint No. 1680 [in Russian], A. F. Ioffe Physicotechnical Institute, Russian Academy of Sciences, St. Petersburg (1996), 40 pp.

¹⁵Yu. L. Serov, and I. P. Yavor, *Zh. Tekh. Fiz.* **65**(3), 38 (1995) [*Tech. Phys.* **40**, 248 (1995)].

¹⁶A. I. Osipov and A. V. Uvarov, *Inzh.-Fiz. Zh.* **55**(1), 149 (1988).

¹⁷A. P. Bedin, *Pis'ma Zh. Tekh. Fiz.* **23**(16), 88 (1997) [*Tech. Phys. Lett.* **23**, 654 (1997)].

Translated by R. M. Durham

Heating of a current filament and formation of constrictions in a pulsed vacuum discharge

E. A. Zverev and I. A. Krinberg

Irkutsk State University

(Submitted March 6, 1998)

Pis'ma Zh. Tekh. Fiz. **24**, 50–56 (September 26, 1998)

It is shown that a rapid current rise in a pulsed vacuum discharge is accompanied by enhanced compression of the current filament by its self-induced magnetic field. As a result, a constriction forms at a distance $L \approx 1$ mm from the cathode and the electron temperature increases to 10^2 – 10^3 eV at currents of order 1 kA. This behavior explains the observed increase in the degree of ion charge and the appearance of x-rays as the current pulse length decreases. The criterion for a rapid rise is the condition $\tau < L/V \approx 10^{-7}$ s, where τ is the characteristic current amplification time and $V \approx 10^6$ is the velocity of the cathode plasma. © 1998 American Institute of Physics. [S1063-7850(98)02309-X]

1. Measurements have shown^{1–3} that the charge state of the ions in the cathode plasma jet of a steady-state vacuum arc discharge only depends on the cathode material and varies negligibly over a wide range of current ($I \approx 50$ – 1200 A) and interelectrode gaps ($l = 1$ – 50 cm). The average ion velocity also varies little with current, remaining in the range $V \approx (1-3) \times 10^6$ m/s (Refs. 4 and 5). These observations agree with the established ideas⁶ that amplification of the current merely leads to an increased number of cathode microspots of size $d_m \approx 1$ μ m, emitting plasma microjets with current $I_m \approx 1$ – 5 A (Refs. 7 and 8). Since an isolated microjet is accelerated to the maximum velocity $V_0 \approx 5(ZT_*/m)^{1/2} \approx 10^6$ cm/s and undergoes maximum heating to $T_* \approx 5$ – 10 eV at distances $r < 30d_m$ from the cathode surface,^{7,9} the entire cathode plasma jet formed at $r > 10^2 d_m$ conserves the same velocity V_0 and almost the same charge state (“frozen” ionization approximately corresponding to the maximum temperature⁷ T_*) but the electron temperature drops to $T_e \approx T_*/3 \approx 1$ – 3 eV (Ref. 10). However, measurements in nonsteady vacuum discharges reveal a substantial increase in the average ion charge Z (for $\tau = 1$ μ s this is doubled¹¹) and electron temperature (in Ref. 12 this was by two orders of magnitude for $\tau \approx 1$ ns) as the current pulse length decreases. Thus, the aim of the present study was to investigate the dynamics of a cathode plasma jet during a rapid current rise using a magnetohydrodynamic model developed in Refs. 10 and 13 for steady-state conditions.

2. In single-fluid magnetohydrodynamics the initial system of equations for a nonsteady-state, current-carrying plasma has the form

$$\frac{\partial \rho}{\partial t} + \nabla \cdot (\rho \mathbf{V}) = 0, \quad \nabla \cdot \mathbf{j} = 0, \quad (1)$$

$$\rho \frac{\partial \mathbf{V}}{\partial t} + \rho (\mathbf{V} \cdot \nabla) \mathbf{V} = -\nabla P + \frac{1}{c} \mathbf{j} \times \mathbf{B}, \quad (2)$$

$$\frac{\partial (\rho \mathcal{E})}{\partial t} + \nabla \cdot (\rho \mathcal{E} \mathbf{V}) = -\nabla \cdot (P \mathbf{V}) + \frac{j^2}{\sigma}, \quad (3)$$

$$\nabla \times \mathbf{B} = \frac{4\pi}{c} \mathbf{j}, \quad \nabla \cdot \mathbf{B} = 0. \quad (4)$$

Here ρ , P , and \mathbf{V} are the plasma mass density, pressure, and velocity, \mathbf{j} is the current density, \mathbf{B} is the magnetic field, $\mathcal{E} = 3T_e/2m + V^2/2$ is the energy density, σ is the plasma conductivity, and m is the ion mass. Bearing in mind that the temperatures satisfy $T_e \gg T_i/Z$, we shall neglect the ion pressure,⁹ assuming $P = T_e N_e$, where N_e is the electron number density.

In what follows we will use the spherical coordinate system (r, θ, ψ) . As in Refs. 10 and 13, we shall assume that compression of the plasma jet by its own self-induced magnetic field is accompanied by the same compression of the current channel and the rate of compression is much lower than the propagation velocity of the jet toward the anode, i.e., $V_\theta \ll V_r$, and the cross section of the jet $S = 2\pi r^2(1 - \cos \alpha)$ is an element of a spherical surface where $\alpha(r, t)$ is the angle corresponding to the lateral boundary of the jet. In order to convert to a one-dimensional approximation, we shall assume that T_e , V_r , and $j_r = j$ are constant over the cross section S but we shall take into account the dependence of the particle density $\rho(\theta)$ and the compression rate $V_\theta(\theta)$ on the polar angle θ . For its profile we use the simplest monotonic dependence on the angle $V_\theta = V_\alpha \theta/\alpha$, where $V_\alpha = r \partial \alpha / \partial t$ is the velocity of the jet boundary. Averaging Eqs. (1)–(3) over the cross section of the jet with allowance for Eq. (4), we find^{10,13}

$$\frac{\partial \rho}{\partial t} + \frac{\partial (\rho V_r S)}{S \partial r} = 0, \quad j = I/S, \quad (5)$$

$$\frac{\partial (\rho V_r)}{\partial t} + \frac{\partial (\rho V_r^2 S)}{S \partial r} = -\frac{\partial P}{\partial r}, \quad (6)$$

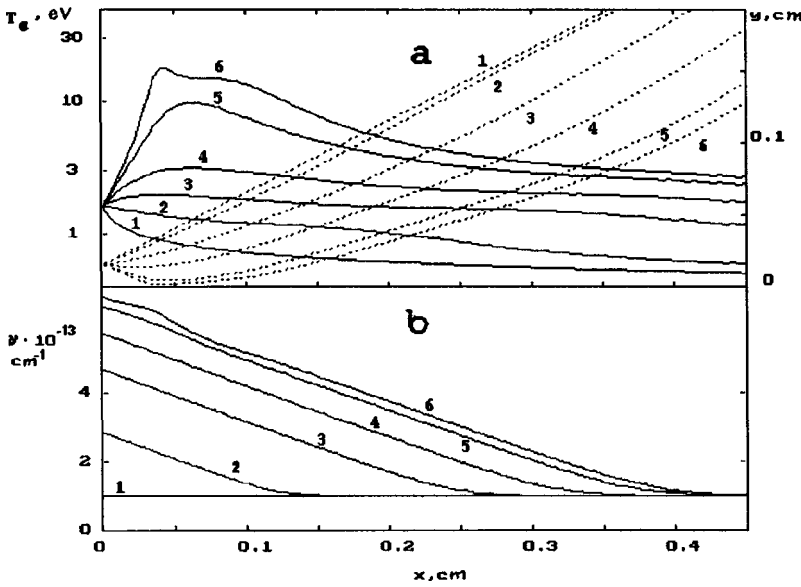


FIG. 1. Parameters of plasma jet for $I=5 \text{ A/ns}$ ($\tau \approx 10^2 \text{ ns}$) at various times: 1, 2, 3, 4, 5, 6 — $t=0, 35, 70, 90, 105, 110 \text{ ns}$; a — electron temperature (solid curve) and jet profile (dashed curve), b — number of ions per unit length.

$$\frac{\partial(\rho\mathcal{E})}{\partial t} + \frac{\partial(\rho V_r \mathcal{E} S)}{S \partial r} = - \frac{\partial(\rho V_r P S)}{S \partial r} + \frac{j^2}{\sigma}. \quad (7)$$

Here $\rho = mN_e/Z$, $P = N_e T_e$, and $\sigma(T_e)$ are the plasma density, pressure, and conductivity averaged over the cross section.

Multiplying the θ projection of Eq. (2) by $1 - \cos \theta$ and integrating over θ between 0 and α , we obtain the equation of motion of the lateral boundary of the jet

$$f(\alpha) \left(\frac{\partial(\rho V_\alpha)}{\partial t} + \frac{\partial(\rho V_r V_\alpha S)}{S \partial r} \right) = \frac{P}{r} - \frac{I^2}{2c^2 r S}. \quad (8)$$

The function $f(\alpha)$ in Eq. (8) depends weakly on the particle density distribution $\rho(\theta)$ over the cross section of the jet and is subsequently taken as $f(\alpha) = \alpha^2/6$ (Ref. 10).

The system of equations (5)–(8) was solved numerically by the particle-in-cell method.¹⁴ Since in this model the particle fluxes in the cross section were taken into account by varying the cross section of the jet, the change in the cross sections of the cells was calculated at the same time as the fluxes following the order of the calculations in the particle-in-cell method.¹⁴

3. The amplification of the discharge current in the cathode plasma jet was simulated as follows. We assumed that the current increases linearly with time, i.e., $I = I_0 + \dot{I}t$, where $\dot{I} = \text{const}$. We also assumed that the microjets merge at the distance $r_0 \approx 300 \mu\text{m}$, and the size of the initial cross section of the total jet $S_0 \approx r_0^2 \approx 10^5 \mu\text{m}^2$ ($\alpha_0 \approx \pi/6$) (Ref. 13) remains constant during the current amplification process. This assumption is acceptable for the time interval studied $t < 300 \text{ ns}$ since, according to Refs. 6 and 8, new cathode microspots (ectons) form predominantly beneath the existing plasma. Thus, an increase in the cross section S_0 can only be expected at $t \approx 10 \mu\text{s}$ (Ref. 2), which corresponds to the cathode heating time. It was also assumed that $I = I_0 = 100 \text{ A}$ at $t = 0$, since at lower currents the jet undergoes no significant compression by its own self-induced magnetic field and the plasma parameters of the entire cathode plasma jet approxi-

mately correspond to those of a single microjet¹³ (which were used as the initial condition). It was assumed that the current is amplified as a result of the formation of new microspots emitting electrons and cathode material with a characteristic dimensionless ratio of mass flux G_m to electric current $ZeG_m/mI_m \approx 0.1$ (Ref. 6). Since the total current is $I(t) = nI_m$ (where $n(t)$ is the number of microspots), and the material flux through the initial cross section is $\rho_0 V_0 S_0 = nG_m$, we find $\rho_0(t) = \rho_0(0)I(t)/I_0$, i.e., the plasma density at the boundary increases simultaneously with the current. The remaining plasma parameters at the boundary $r = r_0$ were assumed to be constant, $V_r = V_0 \approx 4(5ZT_*/3m)^{1/2}$, $V_\alpha = 0$, $T_e = 0.2T_*$, i.e., they were determined by the microjet temperature.^{10,13} The following calculations were made for a Cu and Ti cathode with $Z \approx 2$, $T_* \approx 8 \text{ eV}$, $V_0 \approx 3 \times 10^6 \text{ cm/s}$, and $N_{e0} = \rho_0(0)/m \approx 2 \times 10^{16} \text{ cm}^{-3}$ (Ref. 13).

4. Figures 1 and 2 give results of calculations of the temperature T_e and number of ions per unit length $\nu = N_i S$ ($N_i = N_e/Z$). Also shown is the time evolution of the jet profile $y(x)$, where x and y are the distances parallel and perpendicular to the jet. It can be seen that the compression and heating of the jet are determined to a considerable extent by the time Δt needed by the plasma to fill the interelectrode gap and the characteristic current rise time τ , which can be estimated as $\Delta t = L/V_0$ (for $L = 0.1 - 1 \text{ cm}$ $\Delta t \approx 10^2 \text{ ns}$) and $\tau \approx I/\dot{I}$. In the first case (Fig. 1), we find $\tau \approx \Delta t$ and the plasma can propagate to an appreciable extent over the entire discharge gap, and compression and a rise in temperature are observed along the entire cathode plasma jet whose velocity $V_r \approx V_0$ remains almost constant. In the second case (Fig. 2), we find $\tau \ll \Delta t$ and the heavy particle density ν can only increase near the cathode, whereas the current (transported predominantly by electrons) is amplified along the entire jet. Thus, the jet begins to undergo compression mainly ahead of the front of the material flux where the ratio of the mass flux $m\nu V_r$ to the electric current I becomes substantially lower than the initial value $G_m/I_m \approx 0.1m/Ze$. Figure 2 shows that a constriction begins to develop in the plasma jet, i.e., a local

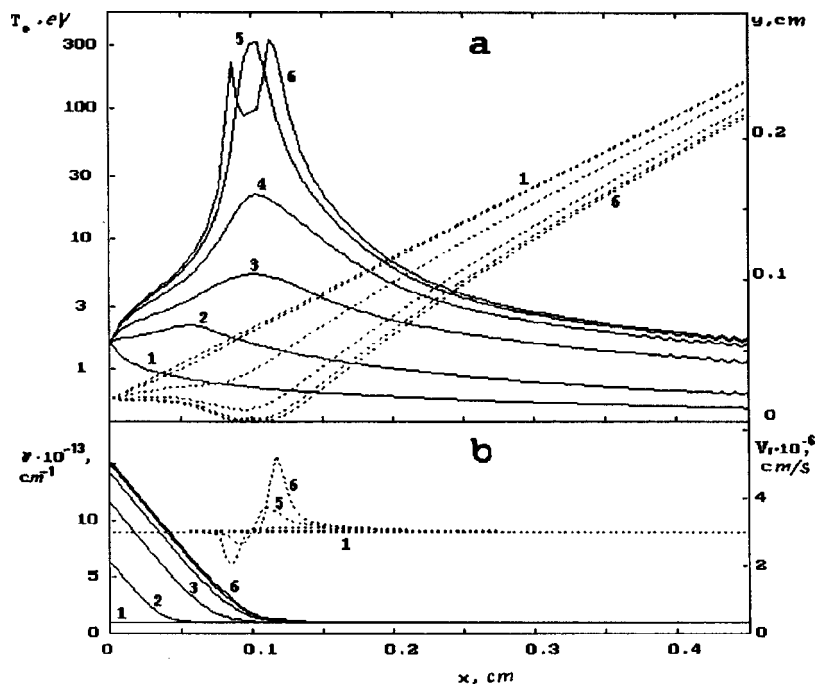


FIG. 2. Parameters of plasma jet for $\dot{I} = 50 \text{ A/ns}$ ($\tau \approx 10\text{--}20 \text{ ns}$) at various times: 1, 2, 3, 4, 5, 6 — $t = 0, 10, 20, 25, 26.5, 27 \text{ ns}$; a — electron temperature (solid curve) and jet profile (dashed curve), b — number of ions per unit length (solid curve) and plasma velocity (dashed curve).

narrowing of the jet cross section. The temperature increases here to $T_e \approx 300 \text{ eV}$ and the plasma begins to be squeezed out of the constriction region. Study of the further evolution of the constriction would have been meaningless, since the condition $V_r \gg V_a$ used in the present model begins to be violated.

These model calculations have shown that unlike a vacuum arc where magnetic compression merely slows the cooling of the plasma (conserving $T_e \approx T_*/3$ (Refs. 10 and 13), in a nonsteady-state cathode plasma jet, a region of compression forms where the electron temperature substantially exceeds the temperature of the initial cathode microjets ($T_e \gg T_*$). Thus, the primary ions in the microjet may undergo further ionization, increasing the charge state Z , which explains the increase in Z observed with decreasing current pulse length.¹¹ The model values of the electron temperature $T_e \approx 100\text{--}300 \text{ eV}$ obtained for $\tau \approx 20 \text{ ns}$ agree with the value $T_e \approx 1 \text{ keV}$ obtained from the x-ray spectrum of a cathode plasma for $\tau < 1 \text{ ns}$.

- ¹I. G. Brown and J. E. Galvin, *IEEE Trans. Plasma Sci.* **17**, 679 (1989).
- ²A. Anders, S. Anders, B. Juttner, and I. G. Brown, *IEEE Trans. Plasma Sci.* **21**(3), 305 (1993).
- ³V. M. Lunev, V. G. Padalka, and V. M. Khoroshikh, *Zh. Tekh. Fiz.* **47**, 1491 (1977) [*Sov. Phys. Tech. Phys.* **22**, 858 (1977)].
- ⁴V. M. Lunev, V. D. Ovcharenko, and V. M. Khoroshikh, *Zh. Tekh. Fiz.* **47**, 1486 (1977) [*Sov. Phys. Tech. Phys.* **22**, 855 (1977)].
- ⁵J. Kutzner and H. C. Miller, *J. Phys. D* **25**, 686 (1992).
- ⁶G. A. Mesyats, *Usp. Fiz. Nauk* **165**, 601 (1995).
- ⁷I. A. Krinberg and M. P. Lukovnikova, *J. Phys. D* **29**, 2901 (1996).
- ⁸V. F. Puchkarev and M. B. Bochkarev, *J. Phys. D* **27**, 1214 (1994).
- ⁹I. A. Krinberg, M. P. Lukovnikova, and V. L. Papernyi, *Zh. Éksp. Teor. Fiz.* **97**, 806 (1990) [*Sov. Phys. JETP* **70**, 451 (1990)].
- ¹⁰I. A. Krinberg and E. A. Zverev, *Pis'ma Zh. Tekh. Fiz.* **23**(11), 47 (1997) [*Tech. Phys. Lett.* **23**, 435 (1997)].
- ¹¹A. Anders, I. Brown, R. Macgill, and M. Dickinson, *Rev. Sci. Instrum.* **67**, 1202 (1996).
- ¹²V. I. Baryshnikov and V. L. Papernyi, *J. Phys. D* **28**, 2519 (1995).
- ¹³I. A. Krinberg and E. A. Zverev, *Fiz. Plazmy* **24** No. 7 (1998).
- ¹⁴O. M. Belotserkovskii, and Yu. M. Davydov, *Particle-in-Cell Method in Gas Dynamics* [in Russian], Nauka, Moscow (1982), 392 pp.

Translated by R. M. Durham

Emission of a surface acoustic wave by an internal acoustic wave propagating near the surface

S. G. Suchkov

N. G. Chernyshevskii State University, Saratov

(Submitted January 19, 1998)

Pis'ma Zh. Tekh. Fiz. **24**, 57–61 (September 26, 1998)

It was observed that the propagation of an internal acoustic wave near a surface is accompanied by the excitation of a surface acoustic wave directed at an angle to the internal wave.

© 1998 American Institute of Physics. [S1063-7850(98)02409-4]

An internal (bulk) acoustic wave propagating along a surface is not a natural wave of an elastic half-space since it does not satisfy the boundary conditions at the surface¹ which are satisfied by a surface acoustic wave (SAW), and thus does not exist without a source of excitation. Strictly speaking, the term “internal acoustic wave at a surface” denotes that part of the angular spectrum of the bulk acoustic waves excited by a source positioned near the surface of a piezoelectric crystal, which propagate at small angles to the surface and whose electric field makes a perceptible contribution to the surface electric potential.² However, a good approximation is to represent an internal acoustic wave at a surface as a planar internal acoustic wave with the wave vector directed inside the crystal but with the group velocity vector parallel to the surface of the crystal.³ This representation will be used in what follows.

It is known that the acoustic wave impedance is proportional to the propagation velocity of the acoustic wave. Thus, the wave impedance of any internal wave propagating along a surface is higher than the wave impedance of the surface wave. The surface region of an elastic medium may be considered to be a set of four channels for the propagation of elastic energy, consisting of three channels for bulk waves and one channel for the surface wave. From the principle of least action, in the presence of several channels for the propagation of elastic energy with different wave impedance, energy will be transferred from a channel with high impedance (high velocity) to channels with lower impedance. The phase condition for the excitation of a slow surface wave when a fast wave propagates along a surface, $k_s \cos \theta = k_b$, where k_s is the wave number of the surface acoustic wave and k_b is the wave number of the internal acoustic wave propagating along the surface, is similar to the phase condition in the Vavilov–Cherenkov effect and the direction of propagation of the surface wave relative to the wave at the surface is determined by the “Cherenkov” angle $\theta = \arccos(v_s/v_b)$.

This effect was analyzed theoretically by using the method of finite differences to solve a model boundary-value problem involving the excitation of an isotropic elastic quarter-space by a longitudinal wave source located close to the surface $y=0$ (Fig. 1a). The calculations showed that for small x , the amplitude of the elastic displacements \mathbf{u} of the

points on the surface $y=0$ is close to zero, but with a further increase in the distance from the source, the amplitude of the elastic displacements u_y begins to increase almost exponentially. The components u_x and u_z also appear and increase by the same amount, which indicates that a surface wave is excited which propagates at the angle $\theta = \arctan(u_z/u_x)$ to the direction of the wave. The dashed curve gives the magnitude of the displacement vector \mathbf{u} of the points on the surface as a function of the coordinate x .

This effect was checked experimentally by fabricating an *ST*-cut quartz device in the form of a filter with waves excited along the *X* axis (Fig. 1b). The device was formed by a single input interdigital transducer with a central SAW frequency of ~ 80 MHz (1) and two output interdigital transducers, one the same as the input transducer (2) and the other having a central SAW frequency of ~ 145 MHz (3), turned through a certain angle and displaced from the axis connecting the input and first output transducers. The periods of these transducers differed approximately by a factor of 1.79 in accordance with the ratio of the longitudinal wave velocity of the internal wave to the surface wave velocity. The distance between the centers of transducers Nos. 1 and 2 was 11 mm and the Cherenkov phase angle allowing for the anisotropy of the SAW velocity as calculated in Ref. 4 was $\theta = 56.2^\circ$. As a result of the deflection of the SAW energy flux through the angle $\Delta\theta = -9.4^\circ$, the digits in transducer No. 3 were inclined to the perpendicular to the transducer axis by the same angle, and the angle of inclination of the axis of transducer No. 3 to the *X* axis was $\approx 46^\circ$.

When a signal at frequency ~ 145 MHz was supplied to input transducer No. 1, this effectively excited a longitudinal wave propagating along the surface which was received by the first output transducer No. 2 with unmatched losses of ~ 40 dB (Fig. 2), and a surface wave signal corresponding to insertion losses of 56 dB was recorded from the second output transducer No. 3 at a frequency of ~ 145 MHz. We shall analyze how this signal level is made up. The filter consisting of two interdigital transducers Nos. 1 and 2 had unmatched losses of 40 dB when operated with a longitudinally polarized bulk acoustic wave propagating at the surface at frequency ~ 145 MHz (SSBAW-*L* in Fig. 2). Assuming that the diffraction losses of the internal wave at the surface for the experimental conditions are around 3 dB (Ref. 2), the

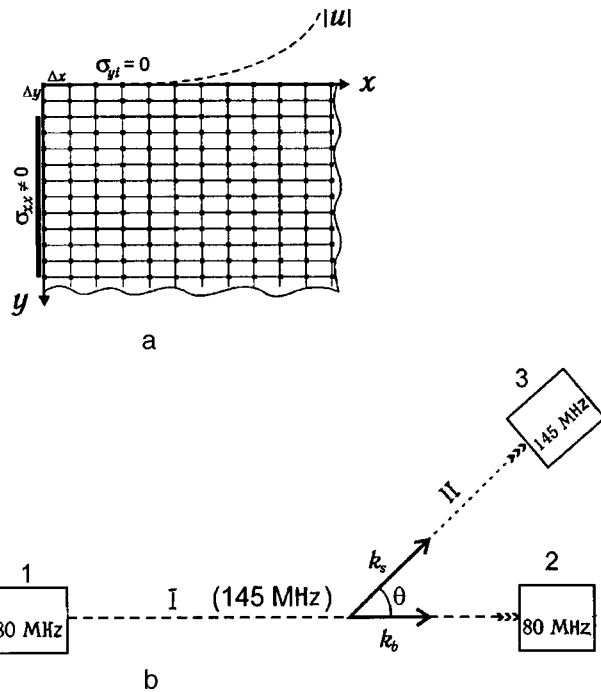


FIG. 1. Diagrams of theoretical modeling (a) and experimental observation (b) of SAW emission (II) accompanying the propagation of a surface-skimming internal acoustic wave (I).

insertion losses for transducer No. 1 are around 18 dB. The insertion losses for the second output transducer, No. 3, receiving a synchronous SAW at frequency ~ 145 MHz were around 13 dB (the same as for transducers Nos. 1 and 2 at 80 MHz). Thus, the transducers alone introduce losses of approximately 31 dB. The surface wave is excited over the entire propagation path of the internal wave so that if the aperture of transducer No. 3 is ~ 1 mm, approximately 10% of the total SAW energy flux may be removed which gives a further 10 dB losses. The symmetry of the SAW radiation introduces 3 dB losses.

This leaves losses of around 12 dB which account for the fraction of the energy of the internal wave lost as a result of emission of the surface wave over the entire $\sim 300\lambda$ propagation path.

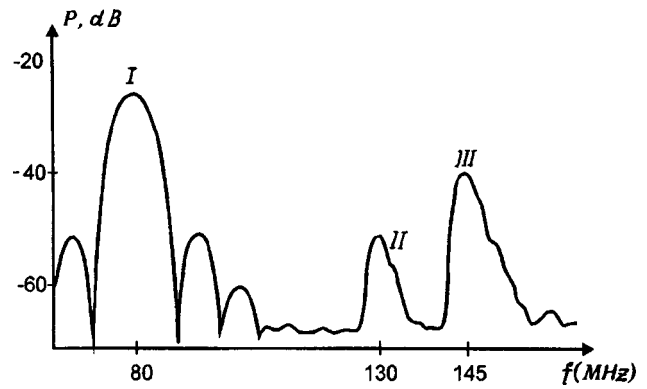


FIG. 2. Amplitude-frequency characteristic of filter formed by interdigital transducers Nos. 1 and 2.

This level of emission has no significant influence on the insertion losses of a longitudinal surface-skimming wave filter fabricated of *ST*-cut quartz, but for other cuts and crystals, the level of SAW emission may increase appreciably. As a result of reflection of SAWs from the side faces of the crystal the pulsed response and thus the amplitude-frequency characteristic of the filter are distorted appreciably. This can be seen clearly in Fig. 2 where the responses from the longitudinal (SSBAW-*L*) and fast transverse (SSBAW-*FT*) waves at the surface have impaired symmetry and shape compared with the SAW response. Thus, it is advisable to make the lateral faces of the crystal dispersive in devices for surface-skimming bulk acoustic waves.

In conclusion, the author thanks V. I. Fedosov (Institute of Radio Electronics of the Russian Academy of Sciences) for assistance and useful discussions.

¹A. Ballato and T. J. Lukaszek, IEEE Trans. Microwave Theory Tech. **MTT-27**, 1004 (1979).

²D. I. Mezhuiev, A. M. Zaslavskii, and S. G. Suchkov, Radiotekh. Elektron. **30**, 1713 (1985).

³S. G. Suchkov *et al.*, Radiotekh. Elektron. **30**, 373 (1985).

⁴T. I. Kazachkova and S. G. Suchkov, Élektron. Tekh. Ser. 1, No. 1, 114 (1979).

Translated by R. M. Durham

Electron entrainment current in gases bombarded with beams of fast highly-charged ions

A. B. Voïtkiv and B. G. Krakov

Institute of Electronics, Uzbek Academy of Sciences, Tashkent
(Submitted January 30, 1997; resubmitted March 6, 1998)
Pis'ma Zh. Tekh. Fiz. **24**, 62–65 (September 26, 1998)

It is shown that asymmetry in the ejection of electrons in an elementary collision event between an atom and a fast highly-charged ion may lead to a macroscopic effect, the electron entrainment current, when a gas target is bombarded by a beam of fast highly-charged ions. The entrainment current is calculated for the bombardment of a helium target by a 25 MeV/u Mo⁴⁰⁺ beam. © 1998 American Institute of Physics. [S1063-7850(98)02509-9]

Recently considerable attention has been paid to studying the ionization of atoms in collisions with fast highly-charged ions (see Refs. 1–6 and the literature cited therein). An interesting phenomenon observed in these studies is the appreciable asymmetry in the ejection of electrons when the atoms are ionized: most of these electrons have positive velocity projections on the direction of motion of the fast highly-charged ion. For example, in an experiment¹ to study the single ionization of helium atoms by Ni²⁴⁺ ions (collision energy 3.6 MeV/u) it was found that even in so-called soft collisions, around 90% of the electrons ejected from the helium atoms propagate in the range $0 \leq \vartheta \leq \pi/2$, where the angle of emission ϑ is measured from the direction of the velocity of the fast highly-charged ion. A theoretical analysis^{1,7} of the single ionization of helium in soft collisions yields similar asymmetries for the ejection of electrons. Experiments also show that similar asymmetry is observed for double and higher degrees of ionization of atoms in collisions with fast highly-charged ions.^{5,6}

Here we show that the asymmetry in the ejection of electrons observed in a microscopic collision event may lead to a macroscopic effect, the electron entrainment current, when a gas target is bombarded by a beam of fast highly-charged ions and we shall estimate the density of this current. We shall assume that a gas having the atomic density n_a is bombarded by a beam of fast particles having the density n_i and the velocity v ($v \gg v_0 = 2 \times 10^8$ cm/s). We shall assume that $d^2\sigma_e/(d\varepsilon \cdot d\Omega)$ is the double differential cross section for the “formation” of a free electron of energy ε with a specific direction of emission from the atom when an incident highly-charged ion collides with a target atom. Then

$$\Delta n_e = n_i n_a v \frac{d^2\sigma_e}{d\varepsilon d\Omega} \Delta\varepsilon \Delta\Omega \quad (1)$$

is the number of electrons having energies in the narrow range between ε and $\varepsilon + \Delta\varepsilon$ and emerging within the small solid angle element $\Delta\Omega$, produced per unit target volume per unit time in collisions with a bombarding particle beam. Let us assume that $\tau_e(\varepsilon)$ is the average time interval between the

ejection of an electron from the parent atom and a collision with some other atom. We shall subsequently assume that the gas target is fairly dense so that the electron mean free path and thus the time $\tau_e(\varepsilon)$ is determined by collisions with target atoms and not with the chamber walls (for the usual densities of highly-charged ions in a beam the densities of product recoil ions are far lower than the density of neutral gas atoms, so that collisions between electrons and recoil ions can be neglected). As usual (see, for example, Ref. 8), we shall assume that on average the first electron–atom collision caused the electron to be knocked out from the current, i.e., the time $\tau_e(\varepsilon)$ is the lifetime of an electron of energy ε in the current. We can then write:

$$\frac{d}{dt} \Delta N_e = - \frac{\Delta N_e}{\tau_e(\varepsilon)} + n_i n_a v \frac{d^2\sigma_e}{d\varepsilon d\Omega} \Delta\varepsilon \Delta\Omega, \quad (2)$$

where ΔN_e is the density of free electrons participating in the current having energies between ε and $\varepsilon + \Delta\varepsilon$ and directions of velocity within $\Delta\Omega$. Assuming that the fast particle beam was injected into the target at time $t=0$ and neglecting the delay (because of the high velocity of these particles), we obtain assuming $\lim_{\Delta\Omega \rightarrow 0} \lim_{\Delta\varepsilon \rightarrow 0} \Delta N_e / (\Delta\Omega \Delta\varepsilon) = d^2 N_e / d\varepsilon d\Omega$:

$$\frac{d^2 N_e}{d\varepsilon d\Omega} = n_i n_a v \tau_e(\varepsilon) \frac{d^2\sigma_e}{d\varepsilon d\Omega} (1 - \exp(-t/\tau_e(\varepsilon))). \quad (3)$$

The expression for the electron current density has the form

$$j_{el} = -|e| \int d\Omega \int d\varepsilon v_e \cos \vartheta \frac{d^2 N_e}{d\varepsilon d\Omega}, \quad (4)$$

where e is the electron charge and v_e is the electron velocity. In the steady-state regime ($t \gg \tau_e$), we find from Eqs. (3) and (4)

$$j_{el} = -|e| n_i n_a v \int d\Omega \int d\varepsilon v_e \cos \vartheta \tau_e(\varepsilon) \frac{d^2\sigma_e}{d\varepsilon d\Omega}. \quad (5)$$

Since $\tau_e(\varepsilon) = 1/(n_a \sigma_{ea} v_e)$, where $\sigma_{ea}(\varepsilon)$ is the total cross section for interaction between an electron of energy ε and an atom, we have

$$j_{el} = -A_{el} |e| n_i v, \quad (6)$$

where

$$A_{\text{el}} = 2\pi \int_0^\infty \frac{d\varepsilon}{\sigma_{ea}(\varepsilon)} \int_0^\pi d\vartheta \sin \vartheta \cos \vartheta \frac{d^2\sigma_e}{d\varepsilon d\Omega}. \quad (7)$$

The number of electrons produced by a beam of fast highly-charged ions in a gas is proportional to the density of gas atoms, and their lifetime in the current is inversely proportional to this density. Thus, the final expression (6) for the electron current density does not depend on the atomic density. Since the cross sections for ionization of atoms in collisions with fast highly-charged ions decrease fairly rapidly with the degree of ionization (the cross sections decrease particularly rapidly in the transition from single to double ionization; see Refs. 5 and 6), for estimates we can assume $d^2\sigma_e/d\varepsilon d\Omega = d^2\sigma_e^{(1+)}/d\varepsilon d\Omega$, where the right-hand side contains the double differential cross section for single ionization of an atom. By way of example we shall estimate the density of the electron current formed by bombardment of a gas consisting of helium atoms by a Mo^{40+} (25 MeV/u) ion beam (the reaction $(25 \text{ MeV/u})\text{Mo}^{40+} + \text{He} \rightarrow \text{Mo}^{40+} + \text{He}^+ + e^-$ is one of the very few involving fast highly-charged ions for which tabular data are available for the double differential cross section for single ionization^{9,2,10}). To obtain the complete cross sections $\sigma_{ea}(\varepsilon)$ for interaction between electrons and helium atoms we used known data (see Refs. 8 and 11–13) on the cross sections for elastic and inelastic collisions. The numerical calculations yield $A_{\text{el}} = 2.1$ and

$$j_{\text{el}}^{\text{He}} = -2.1|e|n_i v. \quad (8)$$

For beam ion densities $n_i \approx (1-100) \text{ cm}^{-3}$ and ion velocity $v \approx 7 \times 10^9 \text{ cm/s}$, which corresponds to the energy 25 MeV/u,

we have $j_{\text{el}}^{\text{He}} \approx 2 \times (10^{-9} - 10^{-7}) \text{ A/cm}^2$, which is quite sufficient to observe this effect experimentally.

In conclusion, the authors would like to thank Professors A. S. Baltenkov and V. Kh. Ferleger for useful discussions.

¹R. Moshhammer, J. Ullrich, M. Unverzagt *et al.*, Phys. Rev. Lett. **73**, 3371 (1994).

²N. Stolterfoht, H. Platten, G. Schiwietz *et al.*, Phys. Rev. A **52**, 3796 (1995).

³R. Moshhammer, M. Unverzagt, W. Schmitt, J. Ullrich, and H. Schmidt-Böcking, Nucl. Instrum. Methods Phys. Res. B **108**, 425 (1996).

⁴R. Moshhammer, J. Ullrich, M. Unverzagt *et al.*, Nucl. Instrum. Methods Phys. Res. B **107**, 62 (1996).

⁵P. Jardin, A. Cassimi, J. P. Grandin, D. Hennecart, and J. P. Lemoigne, Nucl. Instrum. Methods Phys. Res. B **107**, 41 (1996).

⁶M. Unverzagt, R. Moshhammer, W. Schmitt, R. E. Olson, P. Jardin, V. Mergel, J. Ullrich, and H. Schmidt-Böcking, Phys. Rev. Lett. **76**, 1043 (1997).

⁷A. B. Voïtkiv, J. Phys. B **29**, 5344 (1996).

⁸D. R. Bates, *Atomic and Molecular Processes* (Academic Press, New York, 1962; Mir, Moscow, 1964, 777 pp.).

⁹N. Stolterfoht, D. Schneider, J. Tanis *et al.*, Europhys. Lett. **4**, 899 (1987).

¹⁰N. Stolterfoht, D. Schneider, J. Tanis *et al.*, Preprint, Hahn-Meitner-Institut (1995).

¹¹N. F. Mott and H. S. W. Massey, *The Theory of Atomic Collisions*, 3rd ed. (Clarendon Press, Oxford, 1965; Mir, Moscow, 1969, 765 pp.).

¹²G. F. Drukarev, *Collisions of Electrons with Atoms and Molecules* (Plenum Press, New York, 1987) [Russ. original, Nauka, Moscow, 1978, 256 pp.].

¹³M. B. Shan, D. S. Elliot, P. McCallion, and H. B. Gilbody, J. Phys. B **21**, 2751 (1988).

Translated by R. M. Durham

Possibility of increasing proton rejection by detecting primary cosmic radiation electrons using an ionization-neutron calorimeter

G. I. Merzon, V. A. Ryabov, T. Saito, H. Sasaki, A. P. Chubenko, and A. L. Shchepetov

*P. N. Lebedev Physics Institute, Russian Academy of Sciences, Moscow Tokyo University,
Japan Kochi University, Japan*

(Submitted August 25, 1997; resubmitted April 10, 1998)

Pis'ma Zh. Tekh. Fiz. **24**, 66–73 (September 26, 1998)

Measurements were made of the neutron yields from a lead absorber 60 cm thick in electromagnetic cascades initiated by 200–600 MeV electrons. A comparison between the neutron yields obtained for electrons and the results of similar measurements for protons and pions suggests that the rejection factor of the proton background is increased $\sim 10^2$ times when an ionization-neutron calorimeter is used to measure primary cosmic radiation electrons at energies above 100 GeV. © 1998 American Institute of Physics. [S1063-7850(98)02609-3]

INTRODUCTION

At present, one of the most important problems in the physics of cosmic rays and astrophysics involves measuring the energy spectrum of primary electrons at energies above 100 GeV. Interest in primary electrons is by no means accidental. As a result of a rapid increase in the energy losses ($\sim E_e^2$, where E_e is the primary electron energy) through synchronous radiation in the magnetic field of our galaxy and inelastic scattering by relict photons (inverse Compton effect), primary electrons ($E_e > 100$ GeV) may reach the Earth from near (≤ 10 kpc) galactic sources such as Vela, Geminga, and Loops I, II, III, and IV. In this case, the electron spectrum in the range $E > 1$ TeV should undergo substantial changes, including the appearance of strong irregularities, whose observation could reveal the age of the sources and even elucidate the mechanisms for the generation of high-energy cosmic particles in these sources.

Figure 1 shows the present state of the experimental investigations of the primary electron spectra. It can be seen that no experimental data are available on the spectrum above 1 TeV. Some measurements have been made in the range 100–1000 GeV, but the results of different studies are contradictory so that no definitive conclusion can be drawn on the primary electron spectrum.

In many respects, this situation is a consequence of the difficulties involved in distinguishing the electrons under conditions where the primary proton background predominates. To illustrate this Fig. 1 shows the proton spectrum, and it can be seen that at $E \sim 1$ TeV the proton intensity is more than 10^3 times higher than the predicted electron intensity.

Quite clearly, in order to achieve progress in studying the primary electron spectrum at energies above 100 GeV, a more refined experimental technique is required, different from that used in Refs. 1–7 and capable of reliably distinguishing the electrons from the primary proton background. In our view, this problem may be solved by using a new type of detector known as an ionization-neutron calorimeter (INCA), whose possibilities are studied here.

The operating principle of an INCA is as follows. For each cascade generated by a primary particle, measurements are made of the ionization signal (ionization separated in an absorber) and the neutron signal (the yield of evaporated neutrons as a result of nuclear spallation). Since the yield of evaporated neutrons in nuclear cascades should substantially exceed the neutron yield in electromagnetic cascades, the ratio of the neutron signal to the ionization signal may serve as a factor for separating the electrons and protons. In order to check out this supposition, we carried out a series of investigations using the IHEP U-70 and FIAN S-60 accelerators. The results of our measurements of the mean neutron yield $\langle \nu_n \rangle$ and fluctuations for nuclear cascades induced by pions ($E_\pi = 4$ GeV) and protons ($E_p = 70$ GeV) in the U-70 accelerator are summarized in Ref. 8. In the present study, which is a continuation of Ref. 8, we investigate the neutron yield in electromagnetic cascades initiated by electrons with energies $E_e = 200$ –600 MeV. This energy range to a considerable extent determines the neutron yield in electromagnetic cascades, since it includes the main photon absorption processes resulting in the formation of neutrons (giant resonance, deuteron photodisintegration, and formation of the resonances $\Delta(1232)$, $D_{13}(1520)$, and $P_{11}(1440)$).

EXPERIMENTAL SETUP

For the experiments we used an INCA with an absorber containing six rows of lead 10 cm thick with an area of 20×20 cm, interspersed with polyethylene plates 6 cm thick. The neutron detectors were SNM-18 helium (^3He) counters 30 cm long and 3 cm in diameter. Polonium–beryllium sources were used to determine the efficiency ε with which the evaporated neutrons were detected. The mean efficiency was $\langle \varepsilon \rangle = 7.4 \pm 0.4\%$.

Triggering the INCA had the following effects: 1) it extracted the neutron signal from a single beam particle passing through the center of the INCA, 2) it ensured that the neutron signals from two or more particles did not overlap, and 3) it eliminated background particle signals. A more detailed description of the apparatus is given in Ref. 8.

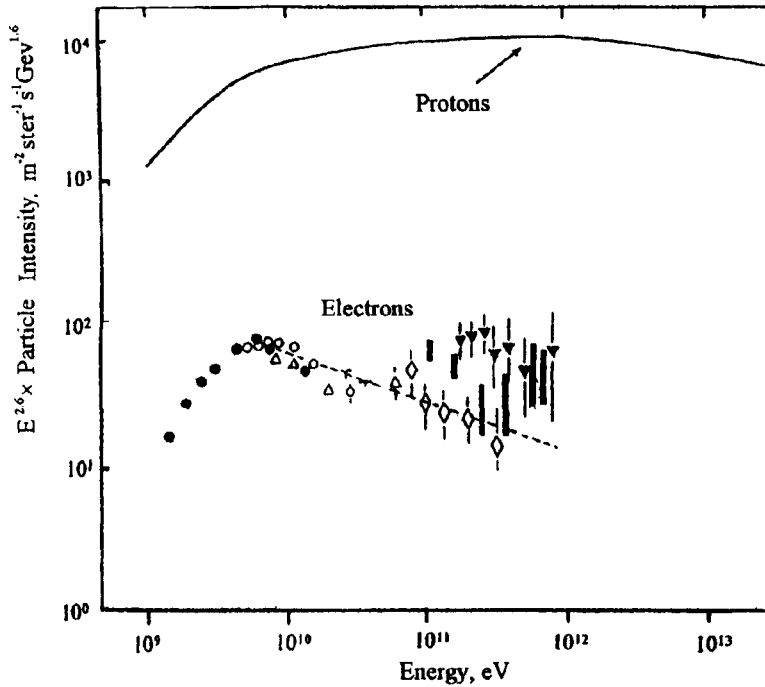


FIG. 1. Energy spectrum of primary electrons. Notation: ∇ — Ref. 1, \diamond — Refs. 2 and 3, $|$ — Ref. 4, \circ — Ref. 5, \bullet — Ref. 6, and \triangle — Ref. 7.

RESULTS AND DISCUSSION

The mean neutron yield $\langle \nu_n \rangle$ was measured at electron energies of 200, 300, 400, 500, and 600 MeV. The data obtained after subtracting the background and making the necessary corrections to the neutron detection efficiency are given in Table I. It should be noted that the background level in our experiment was comparable with the effect being measured. Thus, the values given in Table I may be slightly exaggerated because of insufficient allowance for the background.

In order to compare the values of $\langle \nu_n \rangle$ in electromagnetic and nuclear cascades, Fig. 2 gives the data for the electrons obtained here and also the results of our measurements for pions and protons.⁸ Also plotted are the results of other experiments^{9,10} and calculated data¹¹ for a calorimeter with an infinitely thick lead absorber and for a Pb absorber of finite thickness (60 cm) using the SHIELD program¹².

It can be seen from Fig. 2 that a) the results of our $\langle \nu_n \rangle$ measurements for pions and protons show good agreement with the results of other experiments and the SHIELD calculations; b) the energy dependence of the mean neutron yield $\langle \nu_n^h \rangle(E)$ in nuclear cascades has the form $\sim E^{0.8}$; c) the value of η , which is the ratio of the neutron yield $\langle \nu_n^e \rangle$ in electromagnetic cascades to the yield $\langle \nu_n^h \rangle$ in nuclear cascades, is $\eta \cong 0.01$ at energies $E = 0.6 - 1.0$ GeV.

We used the following formula to determine the energy dependence $\langle \nu_n^e \rangle(E)$ for electrons in the range above 600 MeV:

$$\langle \nu_n^e(E_e) \rangle = \int_0^\infty \int_{E_s}^{E_e} \nu_n(E) N_\gamma(E, t) \frac{dt}{\lambda_\gamma(E)} dE, \quad (1)$$

where $N_\gamma(E, t)$ is the number of γ -quanta of energy E at depth t in an electromagnetic cascade from an electron of energy E_e , E_s is the threshold energy for the photoproduction of neutrons at Pb, $\lambda_\gamma(E)$ is the absorption range of γ -quanta of energy E , and $\nu_n(E)$ is the number of neutrons formed by absorption of a γ -quantum of energy E .

From analysis of formula (1) using data on the absorption cross sections of γ -quanta¹³ and the results of electromagnetic cascade theory,^{14,15} we can draw the following conclusions: I) the values of $\langle \nu_n^e \rangle$ obtained for the electrons agree to within 20% with the data predicted from the absorption cross section of γ -quanta;¹³ II) the energy dependence $\langle \nu_n^e \rangle(E_e)$ in the range $E_e > 600$ MeV has the form

$$\langle \nu_n^e \rangle(E_e) \cong 4 \times 10^{-4} E_e \text{ (MeV)}; \quad (2)$$

III) for Pb the contribution made by photoproduction processes in the range $E_s > 1$ GeV to the coefficient of E_e in formula (2) is no more than 10%.

The agreement between the experimental and calculated values of the yields $\langle \nu_n^e \rangle(E_e)$ from formula (1) confirms the reliability of using formula (2) to extrapolate to the range $E_e > 600$ MeV. Figure 2 shows one such extrapolation. It can be seen that although η increases with increasing energy ($\sim E^{0.2}$), at 100 GeV we find $\eta < 1/20$.

Using this value of η and the distribution of the ν_n^h fluctuations⁸ in nuclear cascades from protons and pions measured in our experiments, we can estimate the probability of ρ -imitation by a cascade proton initiated by an electron (rejection coefficient) for a fixed primary particle energy. For our INCA ($\varepsilon = 7.4\%$), these estimates give $\rho \leq 8\%$ for

TABLE I.

E_e , MeV	200	300	400	500	600
$\langle \nu_n \rangle$	0.08 ± 0.015	0.07 ± 0.01	0.13 ± 0.02	0.28 ± 0.3	0.26 ± 0.03

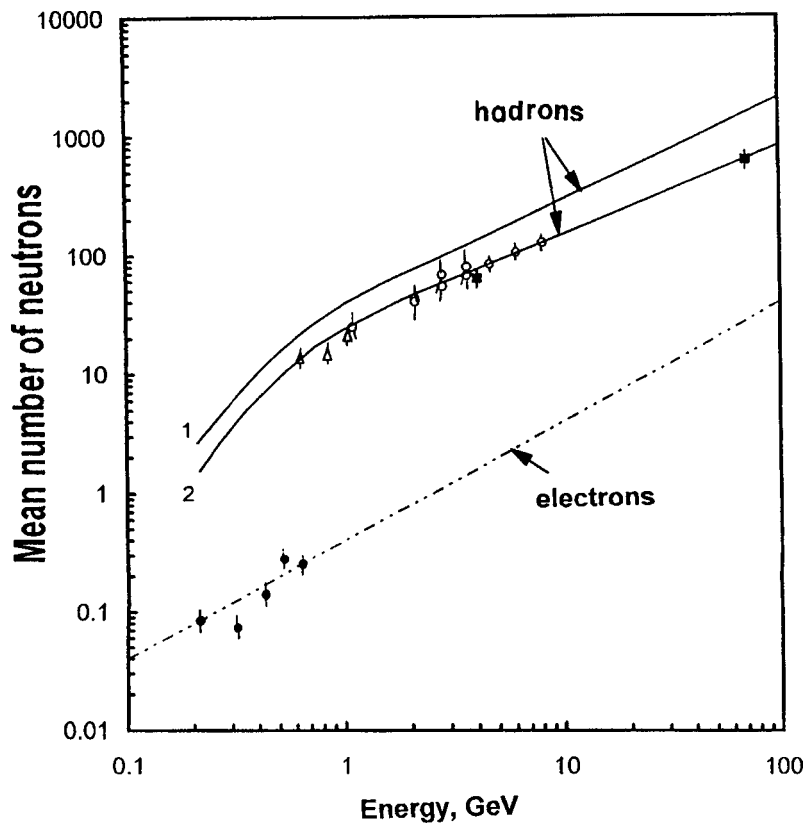


FIG. 2. Neutron yield $\langle \nu_n \rangle$ in electromagnetic cascades from electrons and in nuclear cascades from hadrons for Pb. Curve 1 — calculations¹¹ for an infinitely thick Pb absorber, curve 2 — SHIELD calculations¹² for 60 cm thick Pb. Notation: ■ — Ref. 8, ○ — Ref. 9, and △ — Ref. 10.

$E_\pi = 4$ GeV and $\rho \cong 2\%$ for $E_p = 70$ GeV. Note that the value of ρ decreases not only with increasing hadron energy but also with decreasing ε , so that in the limit $\varepsilon \rightarrow 100\%$ ρ decreases to $\sim 10^{-3}$.

In studies of primary electrons there are two factors which reduce the background from the primary protons, which are always used in experiments: 1) the point of initiation of a cascade should be located at a depth of ≤ 1 radiation length, which gives a rejection coefficient of $\sim 1/30$ (the ratio of one Pd radiation length to the proton interaction range in Pb); and 2) the incident energy spectrum of the primary protons has the result that the intensity of the γ -quanta (which imitate the electromagnetic cascades from electrons) is a factor of $\langle K_\gamma^\beta \rangle$ lower than the proton intensity, where the exponent β is the slope of the proton spectrum and K_γ is the fraction of the energy transferred to γ -quanta in p -Pb interactions. Since for the proton spectrum we have $\beta \cong 1.5$, and $\langle K_\gamma \rangle \cong 0.18-0.20$ (Ref. 16), this gives $\langle K_\gamma^\beta \rangle \cong 1/20-1/40$. The combination of these two factors reduces the background below that of the protons by more than a factor of 400.

Since INCA has an additional rejection coefficient $\rho \leq 10^{-2}$ for $E_e > 100$ GeV, when used to measure the spectrum of primary electrons with energies higher than 100 GeV, it can achieve proton rejection on the scale of $10^{-4}-10^{-5}$.

The authors are deeply grateful to V. A. Tsarev for continuous interest and support of this work.

This work was supported financially by the Russian Fund for Fundamental Research, Grant No. 97-02-17867.

- ¹K. C. Anand, R. R. Daniel, and S. A. Stephens, *Acta Phys. Hung.* **29**, Suppl. 1, 229 (1970).
- ²J. Nishimura and E. Mikimo *et al.*, *Acta Phys. Hung.* **29**, Suppl. 1, 229 (1970).
- ³T. Taira, J. Nishimura, M. Fujii *et al.*, in *Proceedings of the 23rd International Cosmic Ray Conference*, 1993, Vol. 2, OG, p. 128.
- ⁴P. Meyer and D. Müller, in *Proceedings of the 12th International Cosmic Ray Conference*, 1971, Vol 1, p. 117.
- ⁵G. Busini, R. Bellelli *et al.*, in *Proceedings of the 24th International Cosmic Ray Conference*, 1995, Vol. 3, p. 1.
- ⁶R. L. Golden, C. Grimani, B. L. Kimbell *et al.*, *Astrophys. J.* **436**, 769 (1994).
- ⁷A. Buffington *et al.*, *Astrophys. J.* **199**, 669 (1975).
- ⁸V. V. Ammosov, G. I. Merzon, T. Saito *et al.*, *Pis'ma Zh. Tekh. Fiz.* (in press).
- ⁹R. G. Vassilkov and V. I. Yurevich, in *Proceedings of the 11th Meeting of International Collaboration on Advanced Neutron Sources, ICANS-11*, KEK, Tsukuba, Japan, 1990, KEK Report 90-25 (1991), Vol. 1, p. 340.
- ¹⁰V. S. Barashenko, *Nucl. Part. Phys.* **9**, 340 (1978).
- ¹¹E. K. Gel'fand, B. V. Man'ko, and B. S. Sychev, *Izv. Ross. Akad. Nauk, Ser. Fiz.* **58**(12), 41 (1994).
- ¹²A. V. Dement'ev, N. M. Sobolevsky, and Yu. Yu. Stavitsky, *Nucl. Instrum. Methods Phys. Res. A* **374**, 70 (1996).
- ¹³Review of *Particle Properties*, *Phys. Lett. B* **204**, 122 (1988).
- ¹⁴S. Z. Belen'kiĭ, *Avalanche Processes in Cosmic Rays* [in Russian], Gostekhizdat (1948), 243 pp.
- ¹⁵B. B. Rossi and K. Greĭzen, *Rev. Mod. Phys.* **13**, 240 (1941); IL, Moscow, 1948. 132 pp.
- ¹⁶V. P. Pavlyuchenko, R. A. Nam, S. I. Nikol'skiĭ *et al.*, *Tr. Fiz. Inst. Akad. Nauk SSSR* **109**, 31 (1979).

Ion accelerator with space-time modulation of a relativistic electron beam

P. E. Belensov and A. K. Gevorkov

Sukhumi Physicotechnical Institute

(Submitted January 14, 1998)

Pis'ma Zh. Tekh. Fiz. **24**, 74–78 (September 26, 1998)

An analysis is made of a possible method of collective ion acceleration by combining spatial modulation of the electron beam potential with temporal modulation of the current. A conceptual design is proposed. © 1998 American Institute of Physics. [S1063-7850(98)02709-8]

Prospects for the development of collective methods of acceleration are associated with the possibility of exciting space-charge electric fields in electron beams, which can be used to accelerate the ions to high energies.¹

Although the high efficiency of ion acceleration in electron beams has been confirmed experimentally in many research centers,² no realistic physical system has yet been designed in which charged particles could be accelerated by collective fields.

A possible method of collective ion acceleration involves combined spatial modulation of the electron beam potential with temporal modulation of its current.³ Spatial modulation of the electron beam potential may be achieved through spatial modulation of the density by passing the electron beam through a rippled magnetic field. The accelerating electric field is created by an excess charge density near the maxima of the magnetic field. A combination of spatial modulation of the density (with the period L of the magnetic field) and temporal modulation of the beam current (with the period T) gives rise to the slow traveling wave needed to accelerate the ions, having the phase velocity

$$V_{ph} = \frac{L}{T + \frac{L}{v_{el}}} = \frac{v_{el}}{1 + \frac{\Omega}{\omega}}, \tag{1}$$

where $\Omega = 2\pi v_{el}/L$, $\omega = 2\pi/T$, and v_{el} is the velocity of the beam electrons. Under certain conditions, particles propagating synchronously with the phase velocity of the wave may be captured by it and accelerated. In order to accelerate the trapped ions, the wave phase velocity must be increased, which may be achieved by varying the period of spatial modulation of the magnetic field while the temporal modulation frequency of the beam current remains constant. The electric field structure in an accelerator based on this method can provide radial focusing of the ions as well as acceleration.

An analysis of the ion motion in this type of system shows that stable acceleration may be achieved in a range of synchronous phases lying in the range $0 \leq \varphi \leq \pi/2$.

The amplitude of the accelerating electric field in this accelerator depends on the magnitude of the electron beam current

$$E_{20} = \frac{4I_0 a_0}{c\beta R_0} f(k, R_0, b) \sin(kz), \tag{2}$$

where I_0 is the beam current, $\beta = v_{el}/c$, c is the velocity of light, R_0 is the average electron beam radius in the rippled magnetic field, $R = R_0[1 + a_0 \cos(kz)]$, $k = 2\pi/L$, a_0 is the modulation parameter of the beam boundary, b is the radius of the conducting drift tube through which the beam passes, and $f(k, R_0, b)$ is a function determining the structure of the beam space charge field (Fig. 1). High-current uniform or hollow electron beams are best used to obtain high-intensity accelerating fields. Although for the same currents and ratios b/R_0 , the maximum accelerating field on the axis of a hollow beam is only 70% of the field of a uniform beam, it is preferable to use a hollow electron beam since in this case electron fluxes with high limiting currents can be formed and transported:

$$\left. \frac{I_{0 \text{ tube}}}{I_{0 \text{ unif}}} \right|_{R_0 \rightarrow b} = \left(1 + \frac{1}{2 \ln \frac{R_0}{b}} \right) \gg 1. \tag{3}$$

For relativistic factors $\gamma \sim 1.5-2.0$, the stable currents of a hollow relativistic electron beam may reach ≈ 20 kA.

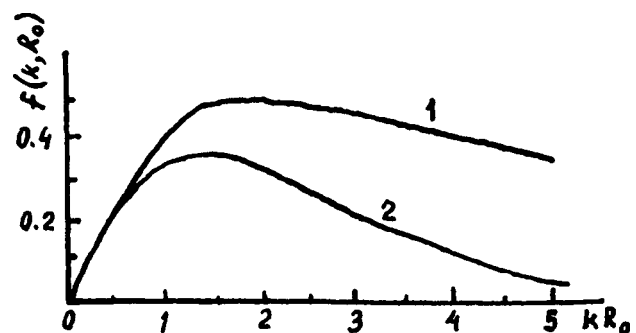


FIG. 1. Structure of accelerating fields for uniform (curve 1) and hollow (curve 2) beams.

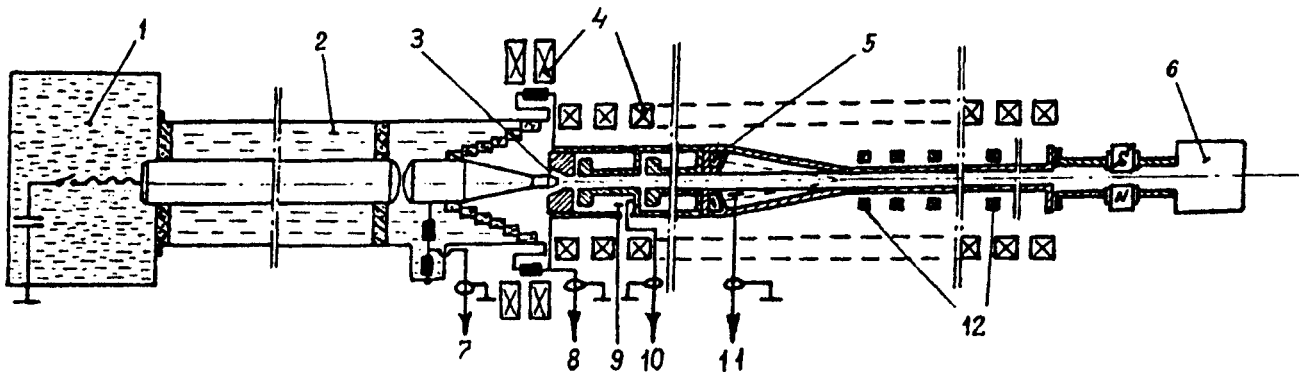


FIG. 2. Schematic diagram of accelerator: 1 — pulse voltage generator, 2 — coaxial line, 3 — electron gun, 4 — guiding magnetic field coils, 5 — ion injector, 6 — ion analyzer, 7 — measurement of diode voltage, 8 — measurement of diode current, 9 — resonator, 10 — measurement of current inside resonator, 11 — electrostatic detector, and 12 — magnetic ripple coils.

The temporal modulation of the relativistic electron beam at a given frequency is based on interaction between the electrons and a narrow slit in the resonator at currents close to the limiting value:^{4,5}

$$I_0 \rightarrow I_{0 \text{ ult}} = \frac{m_0 c^3 (\gamma^{2/3} - 1)^{3/2}}{e \frac{b}{2 \ln \frac{b}{R_0}}}, \quad (4)$$

where m_0 and c are the electron mass and charge.

Three quarter-wave shortened resonators with positive electron feedback are used to obtain reliable 100% modulation of the beams.⁵

The temporally modulated beam is fed into a magnetic ripple cavity with a variable pitch, into which ions are preliminarily injected at a velocity equal to the initial phase velocity of the accelerating wave. These ions, propagating synchronously with the wave field, are accelerated and recorded by an analyzer.

The design of the accelerator model shown in Fig. 2 consists of an Arkad'ev-Marx pulse voltage generator which charges a low-resistance water coaxial line with a pulse-sharpening device,⁶ whose load is a magnetron-type gun. A modulator formed by a set of cavities is mounted coaxially with the magnetron gun and an ion injector¹⁾ is mounted behind the modulator. A drift tube with magnetic ripple is located behind the injector and to this is attached a Thomson analyzer for double time-of-flight analysis.

Principal calculated parameters of accelerator

Beam current	20 kA
Electron energy	360 keV ($\gamma \approx 1.7$)
Pulse length of beam current	60 ns
Beam modulation frequency	166 MHz
Initial proton energy	41 keV
Final proton energy	3 MeV
Amplitude of accelerated proton current	≥ 100 A
Total acceleration length	0.8–1.0 m

¹⁾Figure 2 shows the case where ions are injected from the edge. The case when ions are injected from the end of the relativistic electron beam is not shown.

¹Ya. B. Faĭnberg, *Fiz. Plazmy* 3, 442 (1977) [*Sov. J. Plasma Phys.* 3, 246 (1977)].

²A. A. Plyutto, P. E. Belensov, E. D. Korop, G. P. Mkhedze, V. N. Ryzhkov, K. V. Suladze, and S. M. Temchin, *JETP Lett.* 6, 61 (1967); I. Rander, B. Ecker, and G. Yonas, *Phys. Rev. Lett.* 24, 283 (1970); S. Luce, L. Sahlin, and K. Grites, *IEEE Trans. Nucl. Sci.* NS-10, 336 (1973).

³A. G. Lymar', N. A. Khikhnyak, and V. V. Belikov, *Vopr. At. Nauk. Tekh. Ser. Fiz. Vys. Énerg. Atom. Yad.* Vol. 3 [in Russian], Khar'kov (1973), pp. 78–80; A. N. Lebedev and K. N. Pazin, *At. Énerg.* 41 244 (1976); A. K. Gevorkov, and T. R. Soldatenkov, Preprint SFTI-7 [in Russian], Sukhumi Physicotechnical Institute, Sukhumi (1980), p. 20.

⁴V. V. Krasnopol'skiĭ and V. I. Kalinin, *Zh. Tekh. Fiz.* 56, 1160 (1986) [*Sov. Phys. Tech. Phys.* 31, 679 (1986)].

⁵A. Friedman, V. Serlin, A. Drobot, and L. Seftor, *Phys. Rev. Lett.* 50, 1922 (1983).

⁶G. I. Zverev, V. G. Surovtsev, and L. S. Volkov, in *Proceedings of the All-Union Conference on Controlled Thermonuclear Fusion*, Vol. 2, (1975) [in Russian], p. 153.

Spectral multi-demultiplexer based on a three-dimensional holographic wedge-shaped optical element

I. A. Novikov

D. I. Mendeleev All-Russian Research Institute of Metrology, State Science Center, St. Petersburg

(Submitted November 20, 1997)

Pis'ma Zh. Tekh. Fiz. **24**, 79–86 (September 26, 1998)

An analysis is made of the possibility of developing a new holographic multi-demultiplexer using the principle of a series device constructed as a single three-dimensional optical wedge-shaped element. © 1998 American Institute of Physics. [S1063-7850(98)02809-2]

The development of compact, optical spectral multiplexing devices with high resolution, low optical losses, and a large number of spectral channels in a bounded wavelength range is currently of great interest. These devices can enhance the throughput of fiber-optic information transmission and processing systems and can also improve the structure of these systems.¹ The use of hologram optical elements based on highly selective three-dimensional diffraction gratings^{2,3} is of considerable interest in spectral multiplexing devices.

Several types of optical spectral multi-demultiplexers based on holographic and integrated-optics elements are known.^{2–5} The requirements specified above can be satisfied by using three-dimensional holograms operating in the single-order Bragg diffraction regime. Hologram multi-demultiplexers can be constructed using a series of hologram spectral filters.⁴ In this case, the effective Bragg condition⁶

$$\lambda_m = 2d_m n \sin \theta_m \quad (1)$$

is satisfied for the m th hologram when radiation at wavelength λ_m is incident on it. In Eq. (1), d_m is the period of the three-dimensional phase diffraction grating, n is the average refractive index of the hologram medium, and θ_m is the Bragg angle measured in the medium.⁶

Another possible variant of a hologram multi-demultiplexer consists of a single hologram element made up of a set of several superimposed Bragg three-dimensional diffraction gratings.^{3,5} The advantages of both types of hologram multi-demultiplexers are their high spectral resolution, which can reach fractions of angstroms, and the low optical losses attainable in the working channel (up to 1–2 dB). The main disadvantage of the series multi-demultiplexer⁴ is that it uses several hologram elements which incurs additional optical losses. A disadvantage of the multi-demultiplexer with superimposed gratings is the large dynamic range of variation of the refractive index of the recording medium (up to 10^{-2}) needed to record a large number of holograms. In addition, the relative orientation of the superimposed holograms must be highly precise when fabricating this type of multi-demultiplexer. This disadvantage is particularly apparent when superimposed gratings are fabricated by integrated technology where the problem of effectively matching the hologram optical element with the input and output optical fibers also arises.

Developing the idea put forward in Ref. 7, we shall make a detailed analysis of the properties of a multi-demultiplexer using a holographic optical wedge-shaped element with a Bragg transmission hologram.

OPERATING PRINCIPLE OF MULTI-DEMULTIPLEXER

A new hologram multi-demultiplexer is proposed which uses the principle of a series multi-demultiplexer⁴ constructed in the form of a single three-dimensional holographic optical wedge-shaped element.⁷ A transmission-type phase Bragg holographic grating with constant period d and plane isorefractive surfaces positioned at the angle φ_1 to the surface of the element is recorded in the interior of this element (see Fig. 1).

Figure 1 shows an optical diagram of a demultiplexer using this type of three-dimensional holographic optical wedge-shaped element. A collimated light beam is coupled into the three-dimensional hologram element via a contact prism. The radiation is diffracted by the hologram in accordance with the Bragg condition (1) by being successively reflected from the boundaries of the element and the diffracted beams are coupled out of the element. The angle of inclination of the isorefractive surfaces of the wedge-shaped element is selected so that the diffracted beams are coupled out of the element at the minimum angles to the normal to its surface. The undiffracted beams are completely reflected at the boundaries of the element and propagate as shown in Fig. 1. The condition for total internal reflection of these beams at the boundaries of the element is satisfied by suitably selecting the refractive index of the medium, the wedge angle γ , and the angle of incidence of the input beam. Thus, the undiffracted light (zeroth diffraction order) propagates inside the element with almost zero reflection losses at the boundary.

The wedge-shaped profile of the element has the result that the angle θ_m between the direction of propagation of the light beam and the isophase surfaces of the grating changes after each reflection from the upper boundary of the element. This change in angle is proportional to the number of reflections m and the wedge angle of the element (see Fig. 1):

$$\theta_m = \beta_m - \varphi_1; \quad \beta_m = \beta_1 + (m-1) \gamma. \quad (2)$$

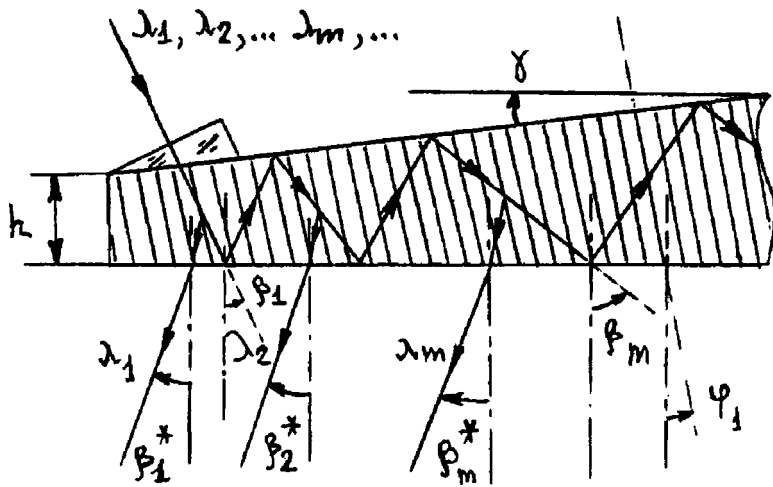


FIG. 1. Operating principle of a spectral multi-demultiplexer using a hologram optical wedge-shaped element.

As a result, after each reflection from the lower boundary of the element, the light is effectively diffracted for different wavelengths λ_m in accordance with the Bragg condition (1). It is easy to show that the wavelength difference for neighboring diffracted beams $\Delta_m = \lambda_m - \lambda_{m-1}$ is given by

$$\Delta_m = \gamma \lambda_{m-1} \cot(\beta_1 - \varphi_1 + (m-2)\gamma). \quad (3)$$

The angles of refraction β_m^* of the rays emerging from the element in air are given by

$$\beta_m^* = \arcsin[n \sin(\beta_1 - 2\varphi_1 + (m-1)\gamma)]. \quad (4)$$

The condition for total internal reflection of the m th ray inside the element yields

$$n \sin(\beta_1 + (m-1)\gamma) \geq 1. \quad (5)$$

This allows us to determine the parameters β_1 and γ for given n and maximum (given) number m .

The real values of these parameters of the wedge-shaped element for $\lambda = 1.55 \mu\text{m}$, $n = 1.5$, $m = 10$, $\Delta_m = 5 \text{ nm}$, and $\varphi_1 = 20^\circ$ are $\gamma = 0.105^\circ$, $\beta_1^* = 13.55^\circ$, and $\beta_1 = 45^\circ$.

OPTICAL LOSSES IN MULTI-DEMULTIPLEXER

The optical losses P_m in the m th working channel of the multi-demultiplexer are attributable to the losses A_m as a result of reflection of light at the surface of the element, the losses B_m as a result of absorption and scattering of radiation in the interior of the element, and the hologram diffraction efficiency η_m . Allowance should also be made for the optical losses C_0 and C_m when radiation is coupled in and out of the element, and the losses D_0 and D_m when radiation is coupled in and out via the optical fiber.

The total optical losses P_m in this multi-demultiplexer in decibels are

$$P_m = A_m + B_m + C_0 + C_m + D_0 + D_m + |\log \eta_m|. \quad (6)$$

If the total-internal-reflection condition (5) is satisfied, the value of A_m is almost zero. The following estimates hold for the other terms in Eq. (6):

$$B_m = |\log \tau_m| = K_\lambda l_m, \quad \tau_m = 10^{-K_\lambda l_m}, \quad (7)$$

where K_λ is the standard absorption coefficient of the recording medium, l_m is the distance covered by the light beam inside the wedge-shaped element for the m th channel

$$l_m = l_{m-1} + 2h/\cos \beta_m, \quad (8)$$

where h is the thickness of the wedge-shaped element and $l_1 = h/\cos \beta_1$. In particular, for $\beta_1 \approx \beta_m = \pi/4$ we have

$$l_m = 2\sqrt{2}h(2m-1). \quad (9)$$

The real values of the absorption coefficient are

$$K_\lambda = (3.0-5.0) \times 10^{-3} \text{ mm}^{-1}$$

for photopolymers and

$$K_\lambda = (1.5-4.5) \times 10^{-3} \text{ mm}^{-1}$$

for porous glasses. For the case described above we have $h = 1 \text{ mm}$ and for photopolymers $B_m \approx 10^{-2}(2m-1)$, and for porous glasses $B_m \approx (5-10) \times 10^{-3}(2m-1)$.

The average values of C_0 and C_m are 0.5–0.8 dB. The optical losses caused by coupling the radiation in and out of the multi-demultiplexer depend on the type of optical fiber supplied (single-mode or multimode) and the quality of the focusing optics, and in practice are 1.0–2.5 dB.

The theoretical diffraction efficiency of the wedge-shaped element is 100% but its practical values for phase three-dimensional transmission holograms are 70–80% (Refs. 4–6). Thus, Eqs. (6)–(9) can be used to estimate the total optical losses in the spectral channels of the multi-demultiplexer.

DIFFRACTION EFFICIENCY, SPECTRAL AND ANGULAR RESOLUTION OF MULTI-DEMULTIPLEXER

The basic properties of phase three-dimensional hologram optical elements are satisfactorily described using the Kogelnik coupled wave theory^{6,8} which gives the well-known expression for the diffraction efficiency of a transmission phase hologram:

$$\eta = [1 + \xi^2/\nu^2]^{-1} \sin^2 \sqrt{(\nu^2 + \xi^2)}. \quad (10)$$

In the formula (10) the expressions for ν and ξ allowing for the wavelength mismatch $\delta\lambda$ and the angle-of-incidence mismatch $\delta\theta$ have the form

$$\xi = [\delta\theta \cos(\beta_m - \varphi_1) - \delta\lambda/2dn] \pi h/dc_2, \quad (11)$$

$$\nu = \pi n_1 h / (\lambda_m + \delta\lambda) (c_1 c_2)^{1/2}, \quad c_1 = \cos(\beta_m + \delta\theta),$$

$$c_2 = \frac{(\lambda + \delta\lambda)}{nh} \sin \varphi_1 + \cos(\beta_m + \delta\theta),$$

where n_1 is the amplitude of the spatial modulation of the refractive index of the medium.

For transmission holograms, the angular selectivity for the m th channel of the wedge-shaped element at the 0.5 level (which corresponds to $\xi \cong 3$) is given by

$$\delta\theta_m = d \left(\cos \beta_m + \frac{d}{h} \sin \beta_m \sin \varphi_1 \right) / h \cos(\beta_m - \varphi_1). \quad (12)$$

Thus, the spectral selectivity $\delta\lambda_m$ of the m th channel of the multi-demultiplexer is given by

$$\delta\lambda_m = d\lambda_m \left(\cos \beta_m + \lambda_m \frac{1}{nh} \sin \varphi_1 \right) / h \sin(\beta_m - \varphi_1). \quad (13)$$

An analysis of expressions (12) and (13) shows that the angular and spectral selectivity of a three-dimensional hologram with inclined isophase surfaces may be either lower (for positive angles φ_1) or higher (for negative φ_1) than that of a symmetric hologram. A numerical simulation of the influence of this factor on the angular and spectral selectivity was made in Ref. 9 for $\varphi_1 < 0$. For $m \leq 10$ the values of $\delta\theta_m$ and $\delta\lambda_m$ for the real parameters of a multi-demultiplexer differ negligibly (by no more than 3–5%).

The spectral resolution $\delta\lambda_1$ of a multi-demultiplexer with a wedge-shaped element of thickness $h = 1$ mm is up to 2.3 nm in the wavelength range $\lambda = 1.3$ – 1.5 μm and around 1 nm for a hologram thickness $h = 2$ mm.

CROSSTALK IN A MULTI-DEMULTIPLEXER

The optical crosstalk P_m in a multi-demultiplexer characterizes the fraction of the optical energy transferred from the i th light source to the working m th spectral channel. To describe the spectral transfer functions of the multi-demultiplexer channels and power-normalized light sources in the Gaussian approximation, the crosstalk can be estimated using the formula⁹

$$P_{im} = 5 \log[1 + (\delta_i / \delta\lambda_m)^2] + 40 \log e(\lambda_i - \lambda_m)^2 / [\delta_i^2 + (\delta\lambda_m)^2]. \quad (14)$$

Here λ_i and λ_m are the average wavelengths of the source and the receiving channel of the multi-demultiplexer, δ_i is the spectral half-width of the i th source, and $\delta\lambda_m$ is the half-width of the pass band (13) of the m th spectral channel of the multi-demultiplexer which corresponds (to within 17–20%) to the half-width of the spectral line in the Gaussian approximation.⁹ The crosstalk in a multi-demultiplexer depends on the spectral characteristics of the wedge-shaped element and the light sources used.

By analogy with the spectral factor (14), in order to achieve a high degree of decoupling between the channels and minimize the losses in the working channels of the multi-demultiplexer (which corresponds to $\lambda_i = \lambda_m$), the angular selectivity $\delta\theta_m$ of the wedge-shaped element must exceed the angular divergence $\delta\theta_0$ of the radiation incident on the element. It was shown in Ref. 9 that the optical crosstalk in a multi-demultiplexer can be estimated satisfactorily using formula (14) subject to the condition $\delta\theta_0 \leq \delta\theta_m/3$. Thus, this multi-demultiplexer requires a high-quality optical collimator. This problem may be solved satisfactorily by using high-quality microscope objectives, self-focusing lenses, or in some cases spherical lenses.

CONCLUSIONS

The main advantage of the proposed multi-demultiplexer is that it uses a single simple three-dimensional hologram sample for numerous (up to ten or more) working spectral channels. This is consistent with current trends toward economical miniaturized optical information processing devices.

The author thanks A. L. Dmitriev for fruitful discussions of problems treated in this work.

¹L. Solymar and D. J. Cook, *Volume Holography and Volume Gratings* (Academic Press, New York, 1981), 466 pp.

²T. Stone and N. George, *Appl. Opt.* **24**, 3797 (1985).

³A. L. Dmitriev, I. A. Novikov, and T. N. Tarasova, *Zh. Prikl. Spektrosk.* **52**, 409 (1990).

⁴A. L. Dmitriev, *Kvantovaya Élektron. (Moscow)* **11**, 1352 (1984) [*Sov. J. Quantum Electron.* **14**, 914 (1984)].

⁵J. M. Senior and S. D. Cusworth, *IEE Proc.-J: Optoelectron.* **136**, 183 (1989).

⁶R. J. Collier, C. B. Burckhardt, and L. H. Lin, *Optical Holography* (Academic Press, New York, 1971; Mir Moscow, 1973, 685 pp.).

⁷I. A. Novikov, in *Advance Program and Abstracts of CLEO/QELS'95*, Baltimore, 1995, p. 86.

⁸H. Kogelnik, *Bell Syst. Tech. J.* **48**, 2909 (1969).

⁹T. V. Basistova, *Tekh. Sredstv Svyazi Ser. TPS No. 2*, 61 (1988).

¹⁰O. I. Gorbunov, A. L. Dmitriev, and V. I. Makkaveev, *Tekh. Sredstv Svyazi Ser. TPS No. 3*, 3 (1985).

Indication of the presence or absence of convective motion in water by nuclear magnetic resonance

B. G. Emets

Kharkov State University

(Submitted March 24, 1998)

Pis'ma Zh. Tekh. Fiz. **24**, 87–90 (September 26, 1998)

Nuclear magnetic resonance was used to determine the characteristic parameters for the evolution of an ensemble of gas bubbles in a liquid exposed to microwave irradiation. These parameters can be used to determine whether convective motion takes place in the liquid. It is observed that a liquid may be “strengthened” by low-intensity radio waves. © 1998 American Institute of Physics. [S1063-7850(98)02909-7]

When a liquid is exposed to electromagnetic waves, radiant energy is dissipated, causing it to undergo nonuniform heating. Under certain conditions, mechanical equilibrium may be established in a nonuniformly heated liquid. If the temperature nonuniformity is sufficiently large, the equilibrium becomes unstable and is replaced by convective motion. In order to analyze the physical processes taking place in a liquid exposed to low-intensity electromagnetic waves, we need to know precisely whether the liquid object is in mechanical equilibrium or whether convection is present. It will be shown subsequently that this question can be answered by using nuclear magnetic resonance (NMR).¹

The absence or presence of hydrodynamic instability can be determined from the nature of the evolution of the gas microbubbles which are always present in a real liquid. If the irradiated liquid is not removed from mechanical equilibrium, heat transfer is purely by conduction and as a result of the thermocapillary effect, bubbles drift slowly from a relatively cold region to a hotter region of the liquid.^{2,3} “Creeping” of air bubbles into a “thermal lens” created by a low-power helium–neon laser beam was observed in Ref. 4, where the authors also observed an increase in the size of the moving bubbles. Obviously, the total number of air bubbles may also increase since the laser beam heats the liquid in the vicinity of the illuminated track, thereby lowering the solubility of the gas in this section.

The main effect observed in the presence of convective motion is that layers of liquid undergo large-scale displacements and are transferred to the free surface together with the bubbles, as a result of which the bubbles can leave the liquid.

The present study was carried out assuming that on exposure to electromagnetic waves, the size and number of air bubbles in a liquid in mechanical equilibrium increase and the number of bubbles decreases as a result of convection. It was shown in Ref. 5 that the difference between the rates of transverse (T_2^{-1}) and longitudinal (T_1^{-1}) nuclear magnetic relaxation depends on the product $\bar{R}\nu$, where \bar{R} is the average radius of the air bubbles contained in the water and ν is the number of bubbles per unit volume. We particularly note that everywhere in this study the symbol T_2^{-1} denotes the rate of transverse nuclear magnetic relaxation measured by

the Carr–Purcell method.¹ We used the working formula tested in Ref. 5 for proton measurements in water, whereby this product is

$$\bar{R}\nu = (T_2^{-1} - T_1^{-1} - 0.05) \left/ \frac{4}{3} \pi^3 D \tau^2 \gamma^2 H_0^2 (\chi_{v,a} - \chi_{v,w})^2 \right.$$

Here D is the coefficient of self-diffusion of the water molecules, which is $2.5 \times 10^{-9} \text{ m}^2/\text{s}$ at the test temperature (22°C), τ is the time interval between the 90° and 180° pulses in the Carr–Purcell method, which is $2 \times 10^{-3} \text{ s}$ in our experiment, $\gamma = 2.68 \times 10^8 \text{ rad} \cdot \text{s}^{-1} \cdot \text{T}^{-1}$ is the proton gyromagnetic ratio, $H_0 = 0.371 \text{ T}$ is the field strength of the relaxometer magnet, $\chi_{v,a} = 3 \times 10^{-8}$ is the volume magnetic susceptibility of air, and $\chi_{v,w} = -7.2 \times 10^{-7}$ is the bulk magnetic susceptibility of water.

For the tests, 0.6 cm^3 of doubly distilled water was placed in a glass ampoule. Measurements of the unirradiated sample at room temperature yielded the product $\bar{R}\nu = (4.8 \pm 1.2) \times 10^7 \text{ m}^{-2}$. The sample was then exposed to microwave irradiation for 30 min from the open end of the waveguide of a 51-I generator (3.2 cm wavelength). As a result of irradiation with a power flux density of $(1.0 \pm 0.1) \text{ mW}/\text{cm}^2$, the product $\bar{R}\nu$ increased to $(7.2 \pm 1.4) \times 10^7 \text{ m}^{-2}$. After exposure to a higher power flux density of $(2.6 \pm 0.1) \text{ mW}/\text{cm}^2$, the product $\bar{R}\nu$ decreased to $(2.3 \pm 1.2) \times 10^7 \text{ m}^{-2}$, which was less than the parameter for the unirradiated sample. It should be considered that in the first case, the liquid was in mechanical equilibrium — the bubbles moved slowly in the field of the temperature gradient and their size and number increased. In the second case, the higher power flux density induced convective motion, which helps to remove air bubbles from the liquid.

It has been shown in hydrodynamics that the appearance of a convective heat flux component, which impairs the mechanism of heat transfer purely by conduction, is observed when the critical Rayleigh number reaches $Rl = g\beta\Delta\Theta L^3\rho/(\eta k)$ (Ref. 6). Here g is the free-fall acceleration, β is the coefficient of thermal expansion, L is the characteristic cavity length, $\Delta\Theta$ is the characteristic temperature difference, ρ is the density of the liquid, η is the dynamic viscosity, and k is the thermal diffusivity. The Rayleigh

number for water was determined experimentally in Ref. 7: $Rl = 1700 \pm 51$. Estimates show that for the geometric dimensions of our sample the convective regime is established when the temperature difference at the boundaries is around 0.4°C . In fact, a temperature rise of 0.3°C was detected by means of a thermocouple during microwave irradiation.

To sum up, nuclear magnetic resonance can be used to identify the time when convective motion is established in a liquid as a result of external influences. The identification of this time can be used to solve many problems in hydromechanics. It is also possible to identify the power flux density of the electromagnetic waves at which efficient removal of air bubbles from the liquid begins. Since the real tensile strength (cavitation strength) of a liquid depends on the concentration of free air contained in it,⁸ it is possible to ‘strengthen’ a liquid by removing the bubbles using

electromagnetic waves with the temperature kept almost constant.

¹A. Abragam, *The Principles of Nuclear Magnetism* (Clarendon Press, Oxford, 1961, 560 pp.; IL, Moscow, 1963, 551 pp.).

²V. G. Levich, *Physicochemical Hydrodynamics* [in Russian], Fizmatgiz, Moscow (1959), 699 pp.

³V. G. Levich and V. S. Krylov, *Annu. Rev. Fluid Mech.* **1**, 293 (1969).

⁴R. G. Yarovaya, N. A. Makarovskii, and N. A. Lupashko, *Zh. Tekh. Fiz.* **58**, 1375 (1988) [*Sov. Phys. Tech. Phys.* **33**, 817 (1988)].

⁵B. G. Emets, *Pis'ma Zh. Tekh. Fiz.* **23**(13), 42 (1997) [*Tech. Phys. Lett.* **23**, 513 (1997)].

⁶G. Z. Gershuni and E. M. Zhukhovitskii, *Convective Stability of Incompressible Fluids*, Israel Program for Scientific Translations, Jerusalem; National Technical Information Service (1976); [Russian orig., Nauka, Moscow (1972), 392 pp.].

⁷P. L. Silveston, *Forsch. Ing. Wes.* **24**(29), 59 (1958).

⁸D. Messino, D. Sette, and F. Wanderlingh, *J. Acoust. Soc. Am.* **35**, 1575 (1963).

Translated by R. M. Durham

Modeling of the fracture of elasticoplastic materials capable of undergoing a phase transition

E. A. Notkina, A. V. Chizhov, and A. A. Shmidt

A. F. Ioffe Physicotechnical Institute, Russian Academy of Sciences, St. Petersburg

(Submitted February 10, 1998)

Pis'ma Zh. Tekh. Fiz. **24**, 91–95 (September 26, 1998)

An investigation was made of the fracture of a layer of iron undergoing a polymorphic α - ϵ phase transition caused by a detonation wave, using an elasticoplastic model of the deformation of a continuous medium with spallation. The influence of the elastic precursor on the spallation was identified. © 1998 American Institute of Physics. [S1063-7850(98)03009-2]

1. The problem of fracture of materials undergoing a polymorphic phase transition under the action of shock and explosive loads arises in a range of applications. From the point of view of the theory of continuum mechanics, it is interesting to develop a mathematical description of wave propagation in condensed media with phase transitions. Numerous results of experimental investigations have now been accumulated on this topic, but this is not sufficient to construct a general model of the phenomenon needed to predict the fracture pattern and optimize the explosive loads. A numerical simulation can be used to analyze the propagation characteristics of compression and rarefaction waves, especially the possible localization of high tensile stresses in particular areas. In a previous study¹ we described a model to calculate the flow of iron undergoing an α - ϵ phase transition, which only allows for the plastic deformation phase, and we reported results of calculations using a one-dimensional formulation which revealed three qualitatively different explosion regimes. Here we use a model which allows for the elastic deformation phase and includes a spallation model. This allowed us to analyze the role of the elastic precursor in the fracture process.

2. An explosion at the surface of a material causes the propagation of a detonation wave which, in the presence of a phase transition, may have a complex structure and consist of several compression and rarefaction waves, as is confirmed by experimental data. Specific rarefaction shock waves may also be produced.

When the compression waves interact with the free boundary, they form secondary rarefaction waves propagating inside the sample. Depending on the parameters of the explosion, either the secondary rarefaction waves near the free surface or interaction between primary and secondary rarefaction waves inside the material produce tensile stresses in excess of the strength threshold and spallation fracture occurs.

A model of a barotropic elasticoplastic medium is used for a mathematical description of the process. It is assumed that the medium is homogeneous and isotropic and the phase transition time is short. The system of equations includes the equations of continuity and motion, and determining relations for the deviator of the stress tensor. The equations are written in Lagrangian coordinates. Hooke's law for elastic

deformations and the Mises plasticity condition are taken as the determining relations. The system is closed by an isothermal equation of state characterized by kinks on the curve $p = p(\rho)$, which correspond to a phase transition and are responsible for splitting the compression and rarefaction waves. Effects such as smooth and multiple spallation accompanying the evolution of fracture in these materials are also associated with the presence of a phase transition. Smooth spallation is observed when two counterpropagating rarefaction shock waves interact, while multiple spallation is attributed to the multiwave structure of the rarefaction waves.

The significant nonlinearity of the equation of state and the presence of phase transitions impose more stringent constraints on the monotonicity of a finite-difference scheme. Thus, the system is discretized by using a TVD shock-capturing scheme constructed for equations written in terms of Riemann invariants. The spatial derivatives are constructed using a method of finite Galerkin elements. Two fracture models were used: instantaneous spallation and a model with a global spallation criterion based on the kinetic strength concept.²

3. The calculations were made for a one-dimensional iron sample. An α - ϵ phase transition at 13 GPa was analyzed and the equations of state for the α and ϵ phases were taken from Refs. 3 and 4, respectively. The simulation showed that, depending on the initial parameters there are

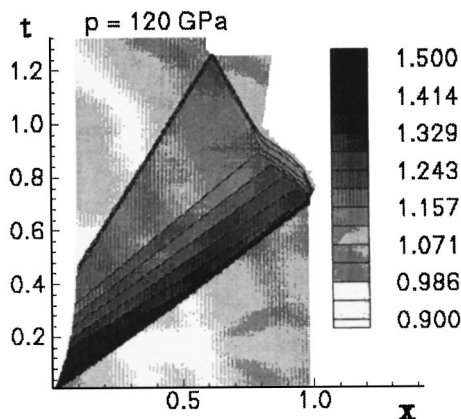


FIG. 1.

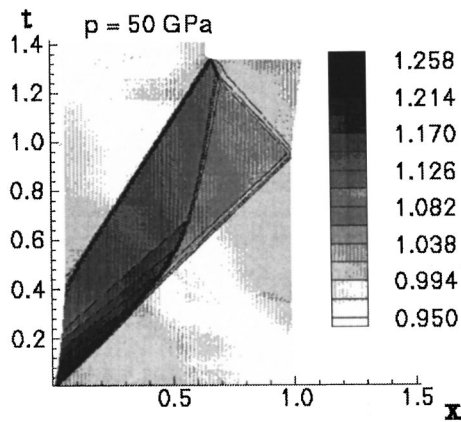


FIG. 2.

three qualitatively different regimes of interaction between the detonation wave and the sample.

The results of the calculations are plotted as $x-t$ density diagrams (all the quantities are normalized to their typical values).

The first regime (Fig. 1) is achieved for a large-amplitude detonation wave ($p > 50$ GPa). In this case, multiple rough spallation is observed near the right-hand boundary in a strong smooth rarefaction wave and smooth spallation occurs inside the sample as a result of the interaction of rarefaction shocks.

In the second case (Fig. 2), the amplitude of the detonation wave is such that a phase transition takes place at the fronts of the compression shock wave and the rarefaction wave. Smooth spallation occurs as a result of interaction between the incident and reflected rarefaction shocks inside the material.

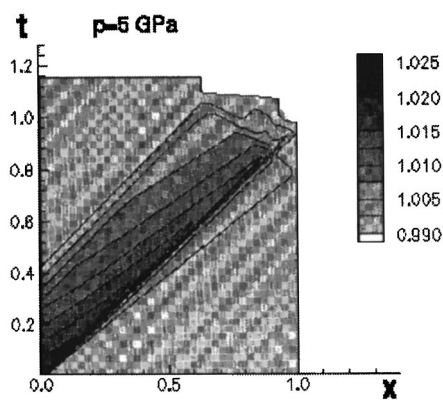


FIG. 3.

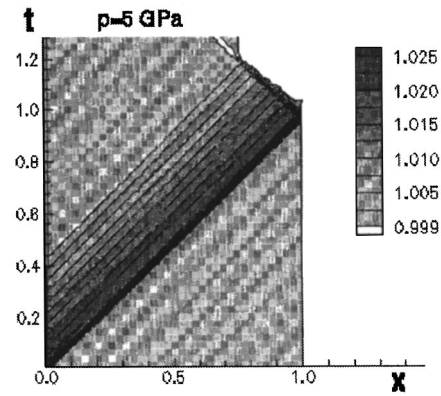


FIG. 4.

The third regime is established when the initial pressure at the surface is lower than the phase transition pressure (Fig. 3). In this case, we observe wave propagation characteristics and spallation patterns associated with the elastic properties of the medium, since the elastic limit σ_H is comparable with the amplitude of the detonation wave. The incident shock wave and the rarefaction waves have a two-wave structure. The elastic precursor propagates at a higher velocity and this is followed by the plastic wave. The incident shock wave is attenuated by the elastic precursor of the rarefaction wave. A comparison between the results of these calculations and the results of a simulation neglecting the elastic properties of the medium (Fig. 4) can reveal the role of the elastic precursor in the evolution of spallation at low tensile strength σ_0 (results are presented for $\sigma_H = 0.53$ GPa and $\sigma_0 = -0.3$ GPa). In the first case, spallation occurs not only in the reflected rarefaction wave but also as a result of interaction between the incident rarefaction wave and the wave formed by interaction between the elastic precursor of the compression shock and the free surface. This explains the substantial difference between the thicknesses of the spallation layers in the calculations using the plastic and elastico-plastic models.

¹A. V. Chizhov, V. O. Chistyakov, and A. A. Shmidt, *Pis'ma Zh. Tekh. Fiz.* **23**(9), 33 (1997) [*Tech. Phys. Lett.* **23**, 347 (1997)].

²B. P. Glushak, V. F. Kuropatenko, and S. A. Novikov, *Investigation of the Strength of Materials Under Dynamic Loading* [in Russian], Nauka, Novosibirsk (1992), 295 pp.

³L. V. Al'tshuler, *Usp. Fiz. Nauk* **85**, 197 (1965) [*Sov. Phys. Usp.* **8**, 52 (1965)].

⁴L. V. Al'tshuler and S. E. Brusnikin, *Teplofiz. Vys. Temp.* **27**, 40 (1989).

Translated by R. M. Durham